



**Release and Remineralization of Ancient Carbon from  
Svalbard Glaciers**

**Master's Thesis**

Master's programme Marine Geoscience at the University Bremen

in cooperation with:

Alfred-Wegener-Institute, Bremerhaven

MARUM, Bremen

Of

**Manuel J. Ruben**

Supervisors

**Professor Dr. Gesine Mollenhauer**

**Dr. Florence Schubotz**

Bremen, January 2020

## Abstract

Within the last two decades several studies have focused on the conundrum of the bioavailability of ancient carbon. In high latitudes this is particularly important, as 40 to 50 % of organic matter (OM) in arctic sediments is estimated to be of petrogenic origin. Arctic Amplification will impact these regions severely in the coming decades. Arctic fjords act as hotspots of carbon burial on a global scale, especially for petrogenic carbon, which makes them an ideal location to study climatically induced changes in OM input to sediments and the related biodegradability of ancient petrogenic carbon. To assess these issues, sediment core HH14-897-MF-GC from Hornsund Fjord on Svalbard was analyzed for changes in OM input using biomarker abundances from 1961 to 2014. Further, the incorporation of ancient carbon by sedimentary bacterial communities was investigated using compound specific radiocarbon dating (CSRD) on intact polar lipid (IPL) derived fatty acids (FA), as indicators for viable microbiota in the sediments. Biomarker abundances indicate only minor changes in sedimentary OM, mainly related to tidewater glacier retreat and subsequent changes in the diagenetic setting caused by lower sedimentation rates. Further, petrogenic and marine OM appear to be the two primary OM sources, with predominantly ancient petrogenic material (>90 %) resulting in bulk sediment ages ranging from  $17,327 \pm 48$  years B.P. at the core top to ages consistently over 24,000 years B.P. below 50 cm sediment depth. Using a two-endmember model, radiocarbon signatures of analyzed IPL-FA suggest incorporation of substantial amounts of ancient petrogenic OM into viable sedimentary bacteria, ranging from 4 to 52 %. Increasing sediment depth and time of sedimentary storage seem to have the most impact on ancient carbon utilization, potentially due to priming.

## Table of Contents

Abstract .....	1
Table of Contents .....	2
Abbreviations .....	4
1. Introduction.....	5
1.1 Goals and Hypotheses .....	10
2. Methodology .....	12
2.1 Study Area and sampling.....	12
2.2 Age model.....	14
2.3 Sampling and sample preparation .....	14
2.4 Sample processing.....	15
2.5 Bulk OM radiocarbon dating .....	15
2.6 Biomarker Analyses .....	16
2.6.1 Lipid extraction.....	16
2.6.2 Saponification and separation of fatty acids.....	16
2.6.3 Silica gel column chromatography .....	17
2.6.4 Methylation and purification of fatty acids.....	17
2.6.5 Neutral lipid separation.....	18
2.6.6 Gas Chromatography – Flame ionization detector .....	18
2.6.7 Gas Chromatography – Mass spectrometry .....	19
2.6.8 High-performance liquid chromatography – Mass spectrometry of GDGTs .....	20
2.7 Compound specific radiocarbon dating of fatty acids.....	20
2.7.1 Pre-extraction sample preparation .....	20
2.7.2 Lipid extraction .....	20
2.7.3 IPL separation through liquid chromatography .....	21
2.7.4 Derivatization of fatty acids.....	21
2.7.5 Gas Chromatography – Preparative fraction collector.....	22
2.7.6 Radiocarbon measurements .....	22
2.7.7 Accelerator mass spectrometry .....	23
2.7.8 Blank correction .....	23
2.7.9 Correction for known contaminations .....	25
2.8 Intact polar lipid analysis.....	26
2.8.1 IPL – Analysis with Q-TOF .....	26
2.9 Biomarker Indices.....	27
2.9.1 Homohopanes .....	27
2.9.2 <i>n</i> -Alkanes .....	28
2.9.3 Fatty Acids .....	28
2.9.4 GDGTs.....	28
2.9.5 Isotope mass balance calculation.....	28
2.9.6 Sediment and mass accumulation rates.....	29
2.10 Supplementary data sets.....	29
3. Results .....	30
3.1 Sediment and mass accumulation rates .....	30
3.2 Bulk organic matter .....	30
3.2.1 <i>n</i> -Alkanes .....	31
3.2.2 Fatty acids.....	33
3.2.3 Fatty acids in relation to <i>n</i> -alkanes.....	34
3.2.4 Glycerol dialkyl glycerol tetraethers.....	34

## Release and Remineralization of Ancient Carbon from Svalbard Glaciers

3.2.5 C <sub>31</sub> Homohopanes.....	34
3.1 Intact polar lipids.....	34
3.2 Compound specific radiocarbon dating .....	36
3.3.1 Glycolipid Fatty Acids .....	37
3.3.2 Polar-Lipid Fatty Acids .....	37
4. Discussion.....	38
4.1 Sources of Organic Matter .....	38
4.1.1 Terrestrial Organic Matter.....	39
4.1.2 Relative Contributions of Marine and Petrogenic Organic Matter .....	40
4.1.3 Petrogenic Organic Matter .....	42
4.1.4 Marine Organic Mater.....	43
4.1.5 Controls on relative abundances of petrogenic and marine OM.....	44
4.1.6 Diagenetic impact on OM composition.....	48
4.1.7 In-situ microbial community .....	49
4.2 Organic matter as microbial substrate.....	51
4.2.1 Origin of dated fatty acids .....	52
4.2.2 Carbon fixation .....	53
4.2.3 Radiocarbon signature of fatty acids.....	54
4.2.4 Isotope mass balance calculation.....	56
4.2.5 Environmental controls .....	57
4.2.6 Priming Effect .....	58
5. Conclusion .....	59
5.1 Outlook.....	60
6. Acknowledgements .....	61
7. References.....	62
Appendix.....	72

## Abbreviations

AGE	Automated graphitization equipment
AMS	Accelerator mass spectrometry
APCI	Atmospheric pressure chemical ionization
BL	Betaine lipids
CIC	Constant input concentration
DCM	Dichlormethane
(lyso-) DPG	(lyso-) Diphosphatidylglycerol
CIS	Cold injection system
CSRD	Compound specific radiocarbon dating
EA	Element analyser
FA	Fatty acid
FAME	Fatty acid methyl ester
F <sup>14</sup> C	Fraction of modern carbon
GC	Gas chromatography
GDGT	Glycerol dialkyl glycerol tetraether
GL	Glycolipid
GLFA	Phospholipid fatty acid
HEX	Hexane
HPLC	High performance liquid chromatography
IPL	Intact polar lipids
MAR	Mass accumulation rate
MeOH	Methanol
MS	Mass spectrometry
NL	Neutral lipids
OM	Organic matter
PC	Phosphatidylcholine
PE	Phosphatidylethanolamine
PFC	Preparative fraction collector
PG	Phosphatidylglycerol
PME	Phosphatidyl-(N)-methylethanolamine
PL	Polarlipid
PO <sub>4</sub> B	Phosphate buffer
PLFA	Phospholipid fatty acid
SAR	Sediment accumulation rate
TAG	Triacylglycerol
TA <sub>FA</sub>	Terrestrial aquatic ratio (fatty acids)
(N-) TLE	(neutral-) Total lipid extract

## 1. Introduction

The effects of climate change are predicted to have a tremendous impact on human societies, some estimates reach economic damages of up to 20 % of GDP (Stern, 2006), with associated changes in water security (Haddeland et al., 2014), agriculture (Adams et al., 1998), and fisheries (Brander, 2010) leading to food and water shortages on local and regional scales (Haddeland et al., 2014; Wheeler and von Braun, 2013). These changes are likely to cause sociopolitical alterations (da Silva, 2004) and consequently severe adaptations of societies on local (Hunt and Watkiss, 2011) and global scales (Burrows and Kinney, 2016; Reuveny, 2007). These climatic changes are strongly influenced by atmospheric greenhouse gas concentrations and thus are coupled to the release and storage of carbon (Change, 2007; Figure 1, Mollenhauer et al., 2019). Sedimentation and burial of organic matter (OM) in marine sediments present an efficient natural way of removing carbon from the atmosphere (Bauer et al., 2013). The degradation of OM in benthic marine environments also plays an essential role as it determines the quantity of carbon ultimately sequestered in deep sediments (Arndt et al., 2013). The input of OM from different sources and its respective molecular composition is of particular interest, as the chemical characteristics of the OM constituents, the so-called “quality of OM”, govern the degree of biochemical processing in benthic microbial communities (Schmidt et al., 2014). However,

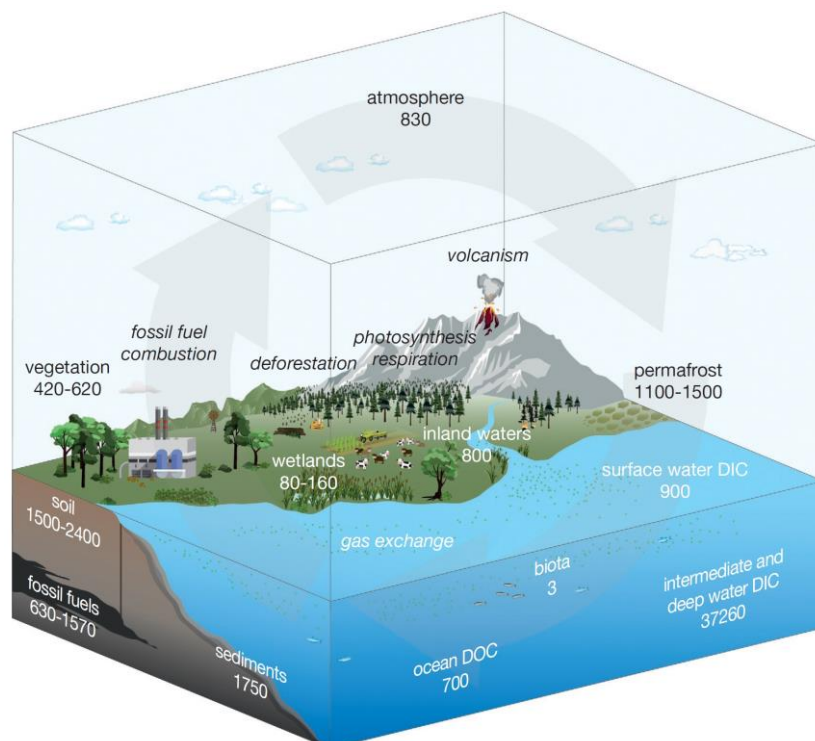


Figure 1: Major global reservoir sizes (**bold**) in Pg carbon and associated exchange flux mechanisms (*italics*). From Mollenhauer et al. (2019).

the composition and quantity of OM buried in sediments changes substantially over space and time (Arndt et al., 2013).

The immense size of the marine realm limits investigation into interactions of different sedimentary processes. Fjords, however, can be regarded as miniature oceans, offering a unique possibility to study processes in a defined space with accelerated rates (Skei, 1983). Despite the early recognition of the potential of fjord based studies, their role in marine carbon burial has only recently been highlighted by Smith et al. (2015) based on an extensive database study. These authors estimated that as much as 18 Mt of carbon are buried in fjords annually, which is equivalent to 11% of total annual carbon buried in marine sediments (Figure 2; Smith et al., 2015). Thus, normalized to their area fjords have by far the highest OM burial rates of any marine environment and can, therefore, be considered as “hot-spots” for OM burial (Smith et al., 2015). A major reason for this is that in comparison to low-land coastal systems, OM mobilized from terrestrial and petrogenic sources in fjords, has very low residence times in the mobilized state, leading to quick deposition and low mineralization during transport. OM residence time in fjords is generally highly influenced by climatic parameters like precipitation and temperature as well as local topography (Cui et al., 2017).

Even though Smith et al. (2015) entailed a wide variety of studies on OM burial in fjords (Cui et al., 2016c, 2017), only a few focused on arctic fjords (Cui et al., 2016a; Kozirowska et al., 2016). Nevertheless, Arctic fjords are of particular interest due to their high sedimentation rates, the associated poor sorting, and thus high rates of conservation and burial of OM (Bianchi et al., 2018). Furthermore,

arctic ecosystems are estimated to be most affected by climate change, a phenomenon known as “Arctic Amplification” (Change, 2007), which results in increased heat uptake in the polar regions, due to shrinking snow and ice surface areas and a subsequent increase in polar albedo. This positive feedback will, cause strong alterations in the near future at high northern latitudes (Change, 2007).

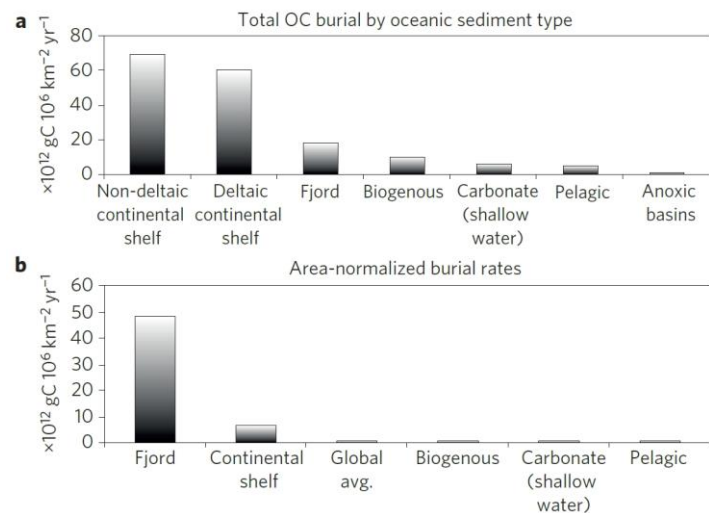


Figure 2: Carbon burial of different oceanic sediment types in total (a) and area-normalized (b). From Smith et al. (2015)

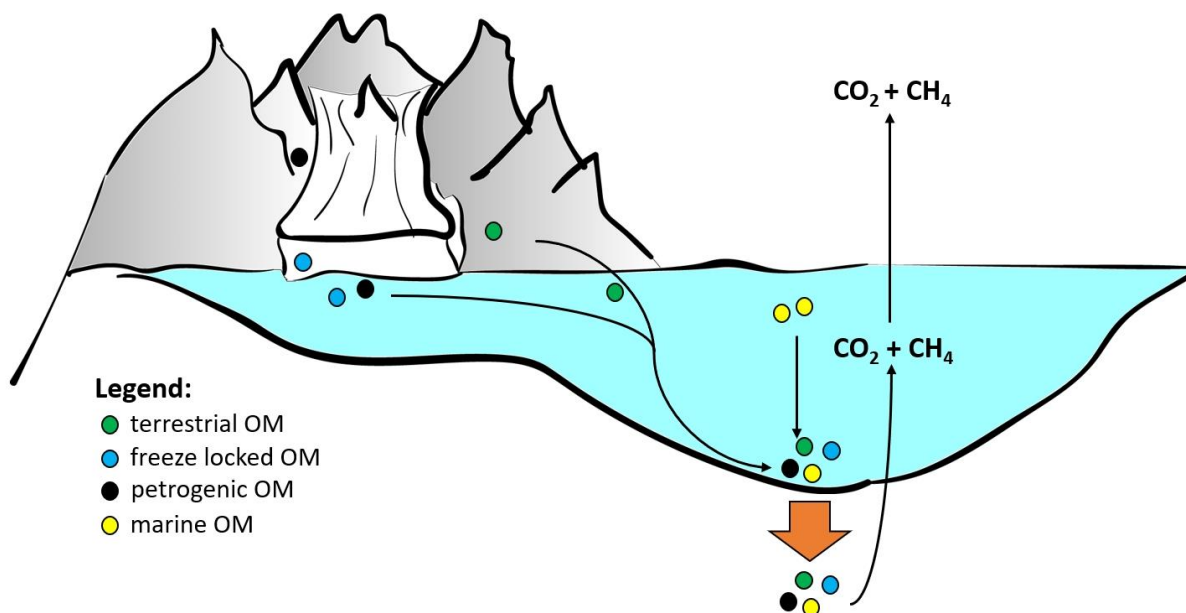


Figure 3: Scheme of possible organic matter sources, their transport and sedimentation to the ocean/fjord floor and subsequently into the sediment (brown arrow). Release of the greenhouse gases CO<sub>2</sub> and CH<sub>4</sub> into the water column and atmosphere, due to remineralization of organic matter in the marine sediments.

Due to their sensitivity to climate changes, arctic fjords are an important focus for OM studies and have been underrepresented in past research (Bianchi et al., 2018). Arctic fjords can show high values of both biogenic and petrogenic OM leading to a complex mixture (Figure 3) of the total organic carbon (TOC) in the accumulated sediments (Walinsky et al., 2009). For the majority of arctic fjords, soils underlain by permafrost (Tarnocai et al., 2009) and/or glaciers are the primary sources of terrigenous organic matter accumulating in fjord sediments (Cottier et al., 2010). In today's state of transitioning climate, both permafrost soils and glaciers have been found to be sources of pre-aged but labile OM being released from previously (freeze-) locked states into downstream aquatic systems, ultimately leading to an additional flux of carbon to the atmosphere, causing a positive feedback of climate warming (Hood et al., 2015, 2009; Winterfeld et al., 2018). Petrogenic organic matter represents ~90 % of organic carbon on earth, is the largest reservoir, and is primarily stored in shales and sedimentary rocks (Galy et al., 2008). Erosion related input due to transition from cold- to warm-based glaciers and runoff increase was estimated to release about 78 Tg of ancient particulate organic carbon and ancient dissolved organic carbon from glaciers into their adjacent aquatic systems by 2050 (Hood et al., 2015). However, Hood et al. (2015) also stated that the reactivity of this ancient material has not been quantified and it is unclear to what extent the ancient OM can be re-mineralized in the downstream environments. Nevertheless, their incubation experiments suggested potentially high bioavailability of the investigated ancient material.

Bio-availability and hence the potential for remineralization of this ancient OM is still highly debated. The current understanding of OM utilization and thus remineralization expects “young”, “fresh”, and therefore “labile” OM to be preferentially utilized by organisms (higher energy yields) rather than “old”, “ancient”, and therefore “recalcitrant” OM. This leads to the widely accepted concept of preservation and sequestration of ancient OM as opposed to reworking and remineralization processes (Guillemette et al., 2017). In contrast to this concept, recent research shows increasing evidence of utilization of ancient OM in settings where fluxes of ancient carbon are increased by both anthropogenic and natural sources (Cui et al., 2016a; Guillemette et al., 2017; Hood et al., 2015; Petsch et al., 2001; Wakeham et al., 2006). In arctic fjord systems, ancient POM often originates from the release of petrogenic sources excavated by glaciers (Cui et al., 2016a) and is subsequently being categorized as remnant and non-bioavailable. Anthropogenic aerosol particles derived from fossil fuel burning have been reported as another source of ancient carbon in glaciers, supplying the majority of fossil DOM to glacial environments (Stubbins et al., 2012). In turn, “young” and labile OM is also produced within the fjord’s water column, local soils (Cui et al., 2017) and glaciers (Hood et al., 2015). Hence, a complex assemblage of OM from diverse sources and ages comes into play (Figure 2), which may change the overall dynamics of the refractory fraction (Guillemette et al., 2017). The input of fresh and labile material has been noticed to enhance the bio-availability and lability of OM over all in soils. This complex and not yet fully understood process of “priming” (Bianchi, 2011; Fontaine et al., 2003; Guillemette et al., 2017) has also been described to enhance refractory OM degradation in marine sediments, especially at high OM concentrations in sediments (Gontikaki et al., 2013). Hence, it may be essential for remineralization of ancient OM in arctic fjord sediments studied in this thesis (Guillemette et al., 2017), but also in a wider picture as 40 % to 50% of the organic carbon buried in arctic sediments derive from supposedly recalcitrant petrogenic OM (Drenzek et al., 2007). With remineralization and preservation of OM playing a key role in regulating atmospheric greenhouse gas levels in the long run (Bauer et al., 2013), the estimation of the changing OM composition and resulting remineralization of the distributed OM is essential for future predictions and models (Arndt et al., 2013; Guillemette et al., 2017).

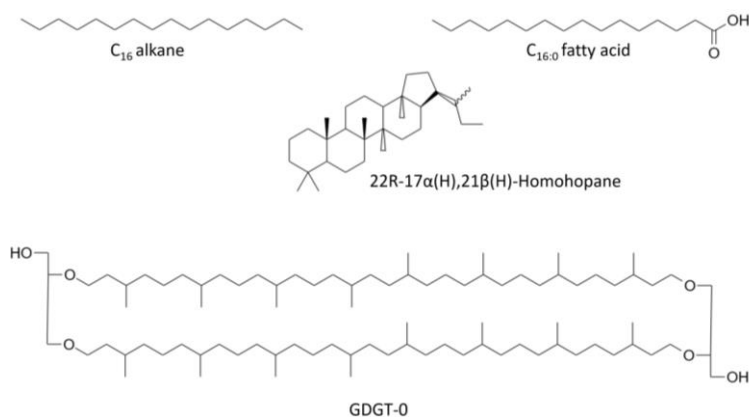


Figure 5: Examples for (remnant) biomarker classes used in this study

Organism specific biomolecules, so-called biomarkers can be used to assess different sources of organic matter in an ecosystem. For this purpose, solvent extractable lipid biomarkers offer great potential in sedimentary studies. Different compound classes like *n*-alkanes, *n*-alkanoic acids (fatty acids; FA), glycerol

dialkyl glycerol tetraethers (GDGTs), and homohopanooids (Figure 5) in combination with their respective number of carbon atoms, isomeric structure, and isotopic signature are indicative for different precursor organisms, environmental, or depositional conditions. These biomarkers are classically used due to their high resilience to degradation (Bianchi and Canuel, 2011). In contrast, IPLs (Figure 4) are widely seen as indicators of living biomass, as these lipids are prone to a quick loss of their head groups within days to weeks after cell death through natural breakdown mechanisms. This class includes glycol-, phospho-, and amino-lipids, which in turn are diagnostic for precursor organisms in combination with their respective side chains (Sturt et al., 2004). These compound classes can be separated by wet chemical preparation to obtain fractions of compounds indicative of viable and non-viable microbiota (Akondi et al., 2017; Ringelberg et al., 1997; Wakeham et al., 2006).

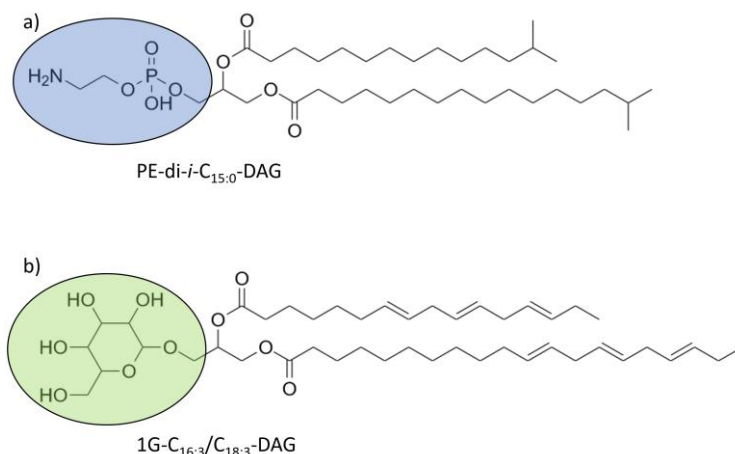


Figure 4: Phospho-(a) and glycolipid (b) examples for labile intact polar lipids and associated fatty acid side chains. Ovals indicate head groups lost quickly after cell lysis from core lipids.

In order to trace different OM-pool inputs to marine sediments on a decadal to millennial time scale, a combined approach of biomarker analysis with bulk and compound CSRD has been proven to be an effective tool to identify (residence) ages of OM accumulated in sediments (Feng et al., 2013; Mollenhauer and Rethemeyer, 2009; Vonk et al., 2017, 2012; Winterfeld et al., 2018). Additionally,

CSRD of IPLs can be used to identify metabolic pathways of modern versus ancient organic compounds in sediments, using  $^{14}\text{C}$  as an inverse-tracer.  $^{14}\text{C}$  is an ideal tracer signal as it can be carried over from the substrate to the utilizing microorganisms, allowing for the biological assimilation of degrading microbiota to be identified through their respective radiocarbon age (Petsch et al., 2001; Slater et al., 2006a; White et al., 2005). In turn, this approach determines if and to what extent, local benthic microbial communities are able to utilize ancient OM. If the ancient OM would entirely consist of non-bioavailable and therefore remnant biomass, extracted FA of IPLs would show modern  $^{14}\text{C}$  activity levels as they would exclusively metabolize recently assimilated biomass, in accordance to the principle “you are what you eat”. On the contrary,  $^{14}\text{C}$  signatures below the modern endmember indicate the possibility of the microbial community to utilize ancient OM as a carbon or energy source for their metabolism. The latter case would suggest ancient carbon utilization by microbes, which would have to be accounted for in future climate models and predictions.

### 1.1 Goals and Hypotheses

This study investigates changes in sedimentary OM composition, their rates of deposition, and remineralization in Hornsund Fjord, Svalbard, over the course of the last 60 years using lipid biomarkers, bulk OM parameters and CSRD. It addresses the hypothesis that changing environmental conditions influence OM production and mobilization. The strong warming of recent decades is expected to result in an overall increase in carbon exported from glaciers and adjacent soils to local fjord sediments.

More specifically, the working hypothesis (1) suggests that increasing atmospheric temperatures lead to higher glacial runoff and higher amounts of petrogenic carbon being exported to downstream aquatic environments. However, with shifting glacial fronts petrogenic OM input may decrease at a given core location over time. Simultaneously, increased runoff leads to higher turbidity in downstream aquatic systems, causing a decrease in marine primary production, due to less sunlight penetration into the photic zone. However, with retreating glaciers this effect may lose its significance as the inflow of turbid waters will follow the glacial front while the ice-free sea surface area will simultaneously increase, in turn leading to a larger area of sunlight penetrating into the sea surface layer. Furthermore, increasing temperatures and decreasing salinity may exert a strong influence on local aquatic primary productivity. Both parameters have to be considered as they are directly or indirectly influenced by atmospheric temperatures and glacial runoff.

Secondly, the uptake of ancient carbon by benthic microbial communities is investigated. It is hypothesized that the mobilization of ancient terrigenous organic matter to arctic fjords will contribute to greenhouse gas emissions due to the microbial degradation of ancient carbon in the marine realm. Specific working hypothesis (2) is that due to the long ongoing, continuous input of ancient OM, local microbial communities have adapted to utilize ancient OM for anabolic and catabolic purposes. Taking into account the principle of “you are what you eat” of the isotopic signature, ancient OM utilizing microbiota are expected to show  $^{14}\text{C}$ -depleted radiocarbon signatures. Nevertheless, if – despite short residence times – remineralization of ancient OM is occurring in the water column already, these microbiota may be exported to the sediment where they could further utilize ancient OM when buried. Downcore profiles will show different stages of OM utilization from freshly deposited sediment (core top) to more mature stages (down core). Allowing a temporal view of the remineralization dynamics. Information about sedimentary OM input (derived from working hypothesis 1) will allow in-depth analysis of the utilized substrate by heterotrophic microbiota using a  $^{14}\text{C}$  endmember model.

Additionally, it is hypothesized (3) that OM degradation by benthic microbial communities is initiated/primed by supply of highly bioavailable organic matter, i.e., from phytoplankton, and will extend to less bioavailable petrogenic organic matter, due to the continuing presence of previously released exoenzymes or other metabolites. This is expected to result in a temporal shift in the radiocarbon signature of the biomarkers (fatty acids) originating from degrading microorganisms. In early stages of degradation (core top), the indicative biomarkers are expected to have a relatively *young* signature. With increasing time/depth these radiocarbon signatures are expected to shift to *older* values. However, the possibility of changes in the primary input of modern and ancient OM has to be taken into consideration while assessing this hypothesis, as this is expected to have a strong impact on the radiocarbon signature of the indicative biomarkers. Ideally, two (or more) samples taken from the same sediment depth, at the same location, but retrieved considerable time apart from one another, would be needed to assess this hypothesis. Nevertheless, by assessing both the OM input to the sediment and the compound specific radiocarbon signatures, a reliable estimation of the importance of priming for the utilization of ancient carbon in arctic fjord sediments will be determined.

## 2. Methodology

### 2.1 Study Area and sampling

The Svalbard archipelago is located between the Arctic Ocean in the north, the North Atlantic in the south and the Barents Sea to the east. On Svalbard's western flank, the Fram Strait is strongly influenced by the West Spitsbergen Current bringing warm and saline Atlantic water to the north, being the primary salt and heat source to the Arctic ocean (Mangerud et al., 2006; Muckenhuber et al., 2016). This results in the relatively mild climate on Svalbard and an overall low ice cover of the eastern Fram Strait (Onarheim et al., 2014). Hornsund Fjord is located at the far south-west of Svalbard (Figure 6). Its location causes a strong influence by cold and low saline Arctic-type waters of the Sørkapp (Costal) Current originating in the Barents Sea, which separates the local microclimate from the other fjords on Svalbard's western coast (Koziorowska et al., 2018). This is of particular importance as local conditions are dominant factors for seasonal sea ice formation rather than large-scale atmospheric and oceanic conditions (Muckenhuber et al., 2016), and therefore are highly susceptible to climatological and hydrological fluctuations (Majewski et al., 2009). Seasonal ice cover is important factor for glacial runoff (Kohler et al., 2007), water column stratification and overturning (Cottier et al., 2010), primary production (Smola et al., 2017), benthic meiofaunal assemblage (Grzelak and Kotwicki, 2012), and burial and sequestration of carbon (Koziorowska et al., 2018). South-West Svalbard's location right on the outer edge of the arctic front makes it highly influenced by global climate change, especially due to Arctic Amplification (Change, 2007), which will in turn also influence local climatic conditions. Thus, current regional processes may be indicative for future regional changes.

Hornsund Fjord comprises of a main basin, connecting multiple smaller side bays to a system of about ~ 32 km length and ~ 10 km width. The glaciers' proximal basins are separated by sills in depths of ~ 100 m from the main fjord basin which is > 250 m deep (Pawłowska et al., 2017). Its complex catchment spans over about 1200 km<sup>2</sup> with 73 % glaciated area (Szczuciński et al., 2006) of which 97 % constitutes thirteen tidewater glaciers. Five of the most active glaciers are located in the innermost basin, Brepollen. With changing climatic conditions these local tidewater glaciers retreated with rates of several tens to 120 m yr<sup>-1</sup> (Błaszczuk et al., 2013), creating expanding bays (Ziaja, 2001) while simultaneously forming "sediment traps" in the inner bays like Brepollen. In these bays, fast ice formation during winter is common, whereas in the central basin sea ice formation varies from one year to the next (Błaszczuk et al., 2013). Local tidewater glaciers supply vast amounts of sediment, reaching sediment accumulation rates of up to 0.7 cm yr<sup>-1</sup> (Szczuciński et al., 2006). During summer,

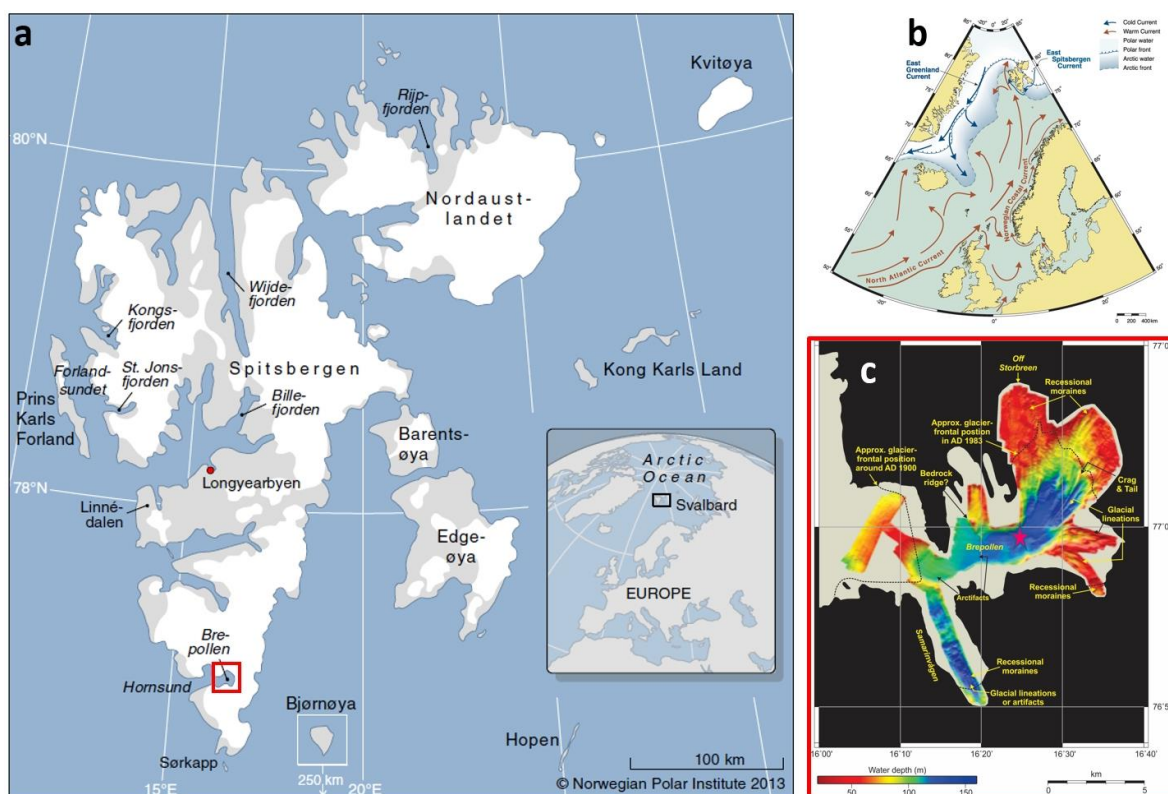


Figure 6: a) Map of Svalbard's fjords, glaciers (indicated in white), and non-glaciated areas. b) North Atlantic currents indicating Svalbard's location on the Arctic front (Mangerud et al., 2006). c) Bathymetric map of the Brepollen bay, location in a) indicated by red rectangle (personal correspondence Forwick, 2019) and marking coring location of HH14-897-MF-GC (magenta star).

meltwater runoff increases drastically leading to strong stratification at Brepollen bay. Associated high loads of suspended inorganic material limits the euphotic zone and consequently primary production (Grzelak and Kotwicki, 2012). However, local primary production rates are still relatively high with rates up to 120 to 220 g C m<sup>-2</sup> yr<sup>-1</sup> (Piwosz et al., 2009; Smoła et al., 2017). Leading to high sedimentary organic carbon concentrations ranging from 1.38 % to 1.98 % (Koziorowska et al., 2016). Most contributing primary producers are diatoms, with increasing dominance towards the fjord mouth, and nanoflagellates (Piwosz et al., 2009). Due to extensive glaciation, the exposed terrestrial terrain in the catchment area of Brepollen is extremely small and its time of exposure is limited to the recent decades of fast glacial retreat (Błaszczuk et al., 2013). Hence, biomarker concentrations of recently produced terrestrial OM and soils are expected to be negligible for the investigated sediment core and sedimentary OM input can be assessed by using two-endmember models of marine and petrogenic biomarkers.

The location of Hornsund Fjord at the arctic frontal region and the associated strong climatic changes (Saloranta and Svendsen, 2001) make it a key study area to investigate changes in OM cycling as part of the global carbon cycle. For this study, sediment samples were taken from gravity core HH14-897-

Manuel J. Ruben

GC-MF. It was obtained on board of the RV Helmer Hanssen in October 2014 in the most proximal bay of Hornsund Fjord, Brepollen, in a water depth of 140 m (Figure 1).

## 2.2 Age model

The age model was created by Szczuciński (2019, personal communication, AMU) on the basis of a  $^{210}\text{Pb}_{\text{xs}}$  constant initial concentration (CIC) model after Robbins and Edgington (1975), verified with  $^{137}\text{Cs}$  peaks for 1963 and 1986. Measurements were performed every 2 cm downcore, allowing the construction of a high-resolution age model. The  $^{210}\text{Pb}_{\text{xs}}$  and  $^{137}\text{Cs}$  data were obtained at the Department of Mineralogy and Petrology at Adam Mickiewicz University, Poland using gamma spectrometry. The age model was cross-checked by comparison to reconstructed glacial forefronts (Błaszczuk et al., 2013), coring date, laminations visible in X-ray scans, and sediment thickness.

## 2.3 Sampling and sample preparation

Organic compounds for biomarker analysis were extracted from 22 sediment samples throughout the core. Sampling depths were chosen on the basis of the age model provided by Szczuciński (2019, personal communication, AMU). The age model indicates the earliest sample age for the biomarker analysis at 1961 AD and the youngest at the core top at 2014 AD, leading to a biogeochemical archive of 53 years (Table 1).

Further, five large volume samples were taken for CSRD (Table 2). In order to obtain lipids in sufficient quantities to allow compound specific radiocarbon dating (CSRD) the sample size chosen was larger than for the classic biomarker abundances samples. In total 5 samples were taken of the archive half of gravity core HH14-897-GC-MF. Each sample was taken over a depth interval of 3 cm. To obtain as much sample volume as possible the whole core section was used. However, the outer edges of the sediment-cake were removed to prevent contamination from the liner and from carry-over. All samples were stored in pre-combusted glass containers at  $-20^{\circ}\text{C}$ , freeze-dried, and then homogenized in an agate mortar.

Depth [cm]	Year of Deposition, A.D.	Dry weight [g]
1.5	2011	3.01
4.5	2005	3.01
8	2000	3.05
13	1993	3.00
16.5	1990	2.99
19	1989	3.01
22	1987	3.03
25	1986	3.10
28	1986	3.01
31	1985	3.04
34	1983	3.02
43.5	1982	3.03
53.5	1980	3.07
60	1978	3.09
73.5	1975	3.00
83.5	1973	3.07
96	1971	2.99
103	1969	3.01
113	1967	3.01
123	1965	3.07
133	1962	3.09
137.5	1961	3.03

Table 1: Depth, age, and weight of the samples used for biomarker abundances. Ages: dated by Szczuciński (green) and interpolated (blue)

Depth interval [cm]	Year(s) of Deposition, A.D.	Dry weight [g]
0-3	2014-2008	60.67
5-8	2004-2000	77.20
10-13	1997-1993	76.56
86-89	1972	81.83
133-136	1962	82.29

Table 2: CSRD samples, time of sedimentation and dry weight of sediment extracted off.

## 2.4 Sample processing

The general workflow of laboratory procedures used for this thesis is shown in Figure 7. Different procedural steps are displayed and linked to their respective analytical methods (green boxes). As displayed, the working methods were split into four procedures. In the following chapter, the individual methods are described. All used glass-ware were pre-combusted overnight at 450°C.

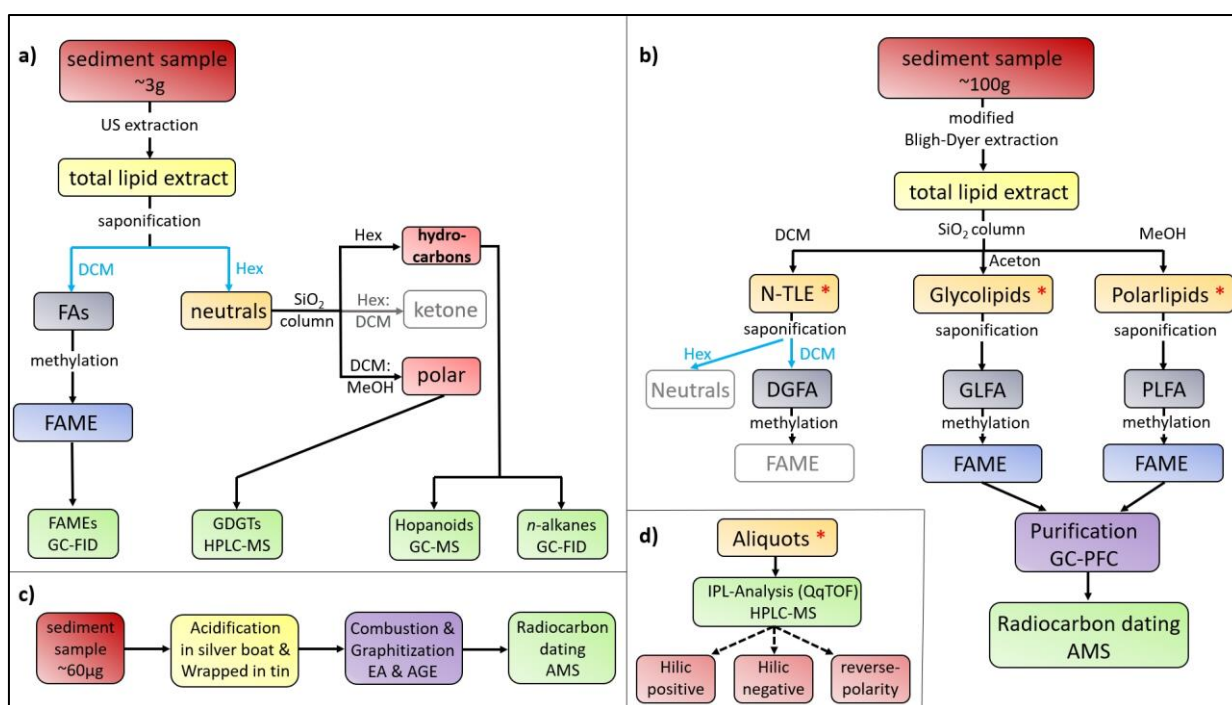


**Figure 7: General lab work workflow for a) biomarker abundances, b) CSRD, c) bulk radiocarbon, and d) IPL analysis (performed for all three fractions) – Box color codes are as followed, dark red: sediments; yellow: total lipid extracts; orange: unsaponified lipids; red \*: link between workflow b) and d); dark blue: fatty acid fractions; bright blue: fatty acid methyl ester; bright red: fractions of neutral lipids; purple: technical preparative procedures; green: analytical methods used; pink: QqTOP modes used for samples; grey: extracted and stored fractions, but not used in this study. Black lines, arrows and text modulators: used and described methods including solvents; Blue arrows: indicate liquid-liquid extraction including solvents; Dashed black arrows: no procedural advancement, but different analytical mode.**

## 2.5 Bulk OM radiocarbon dating

Sample sizes were determined by the sample's respective TOC content. Sediment samples for this thesis were consistently ~2 wt% TOC. In order to get target carbon concentrations of 1 mg C for accelerator mass spectroscopy (AMS), 50 - 60 mg of sediment were separated in small silver boats (Figure 7c). For each sample, two aliquots were weighed successively into silver boats, the second one being considerably smaller (~10 %) as it would later function as a pre-sample to clean the system. The sediment in the silver boats was acidified with super-pure 6 M HCl to remove inorganic carbon and subsequently dried on a hotplate at 60°C, three consecutive times. After the third acidification samples were dried overnight at 60°C. Subsequently, silver boats were folded tightly and wrapped into tin foil.

At first, one pre-sample was run to clean the system from any contaminants, the actual sample was run thereafter. Prepared samples were combusted in an Element Analyzer (EA) at 950°C in a constant flow of helium with the addition of oxygen. Emitted combustion gases were completely oxidized by excess oxygen and copper oxide in the combustion tube. The sample packages were made of tin foil which functioned as a catalyst. The resulting gas-mixture was composed of CO<sub>2</sub>, N<sub>2</sub>, and H<sub>2</sub>O. Subsequently, the three gases were separated by chromatography. The purified CO<sub>2</sub> gas was transferred to an Automated Graphitization Equipment (AGE), where the transferred CO<sub>2</sub> gas from EA combustion was absorbed and concentrated on a zeolite trap and the other gases were vented. After the complete transfer, the zeolite trap was heated to a temperature of 450 °C. Due to thermal desorption and associated thermal expansion of the trapped CO<sub>2</sub> gas, it was released and transferred into a pre-evacuated quartz glass vial attached to the reactor chamber, and heated up to 580°C after gas injection. A local hydrogen atmosphere in the presence of an iron catalyst completely reduced the inflowing CO<sub>2</sub> gas from the zeolite trap within the vial, and caused graphite to precipitate on the surface of the iron powder the vial. The resulting graphite was pressed into targets and later measured using AMS. Recovered graphite pellets were further pressed into targets before determining their respective F<sup>14</sup>C using AMS at the MICADAS lab in Bremerhaven (AWI, compare section 2.7.7).

## 2.6 Biomarker Analyses

### 2.6.1 Lipid extraction

Lipid biomarkers were extracted in a multi-step (Figure 7a) procedure from ~ 3 g of the dry, ground and homogenous sediment by

ultrasonic extraction (3 x 15 min, at room temperature) with three times 25 mL of a mixture of dichloromethane (DCM) and methanol (MeOH) in a volumetric ratio of 9:1. For quantification of the different lipid classes, 10 µL of an internal standard mixture (Table 3) was added to the weighed sediment (Table 1) prior to extraction.

Compound class	Internal standard	Concentration
n-alkanes	Squalane (Sq)	82.00 ng/µL
n-alkanoic acids	19-methylarachidic acid (19-MA)	161.04 ng/µL
GDGTs	C46-GDGT	80.96 ng/µL

Table 3: Internal standards used for biomarker quantification

### 2.6.2 Saponification and separation of fatty acids

After extraction, the total lipid extracts (TLE) were saponified in 1.5 mL (CSRD: 15 mL) of a solution of 0.5 M KOH in MeOH:H<sub>2</sub>O 9:1 (v:v) for 2 hours at 80°C, cleaving off FAs from their respective precursor molecules forming more polar, dissolved FA potassium salts. From this mixture, the remaining neutral lipids were separated three times using 1.0 mL (CSRD: 10 mL) *n*-hexane (HEX) in liquid-liquid phase separation. Subsequently, the residual solution of the TLE containing the organic salts was re-acidified

to FAs using hydrochloric acid until reaching a pH-value of 1. FAs were further purified by three times liquid-liquid phase separation using 1.0 mL (CSRD: 10 mL) DCM. This procedure resulted in one fraction each for neutral lipids and FAs.

### 2.6.3 Silica gel column chromatography

In the following sections, different wet chemical procedures are described. Within these protocols liquid chromatography is used for compound separation and purification. Different compound classes were eluted from the stationary phase (column) by selected mobile phases (solvents), due to their individual polarities and the compounds' respective interactions between stationary and mobile phase(s). Although the mobile phase changed due to different procedural requirements, the stationary phase was consistent.

As stationary phase, a silica column was set up for each individual separation (Figure 8: Silica column setupFigure 8). For this purpose, 1 g of pre-combusted

silica gel ( $\text{SiO}_2$ , deactivated with 1 %  $\text{H}_2\text{O}$ ) suspended in HEX was loaded into a 4 mL pre-combusted glass pipette, resulting in a silica column length of 4 cm. In order to prevent silica gel from discharging off the pipette and entering the purified fractions, the bottom of the pipette was filled with pre-combusted glass wool prior to loading. Additionally, an ~5 mm thick layer of  $\text{Na}_2\text{SO}_4$  was added on top of the silica gel to prevent any  $\text{H}_2\text{O}$  from entering the column and interfering with its polarity properties. Subsequently, compounds were loaded onto the column by three times 100  $\mu\text{L}$  of the eluting solvents described in 2.6.4, 2.6.5, and 2.7.3 before the mobile phase was added.

### 2.6.4 Methylation and purification of fatty acids

FA fractions were methylated overnight in a  $\text{MeOH}:\text{HCl}_{37\%}$  95:5 (v:v) solution at  $50^\circ\text{C}$ , forming less polar fatty acid methyl ester (FAME). The isotopic signature of the used MeOH was determined prior to methylation. Obtained FAMEs were further purified by column chromatography to remove remaining polar components. Silica gel was used as a stationary phase (compare section 2.6.3) with two different mobile phases. First FAMEs were eluted using 4 mL  $\text{DCM}:\text{HEX}$  2:1 (v:v) followed by the second phase, eluting polar compounds with 4 mL  $\text{DCM}:\text{MeOH}$  1:1 (v:v). The purified FAMEs were quantified by gas chromatography (GC) – flame ionization detector (FID).

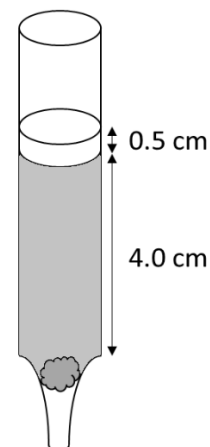


Figure 8: Silica column setup. Glass pipette, filled with glass-wool (dark gray), silica gel (light gray), and  $\text{Na}_2\text{SO}_4$  (white).

### 2.6.5 Neutral lipid separation

Neutral lipids were separated into three fractions over a pre-combusted silica column (compare section 2.6.3). Fraction one was eluted first with 4 mL HEX, containing non-polar components, primarily *n*-alkanes. Secondly, ketones were eluted with 4 ml of DCM:HEX 2:1 (v:v) into fraction two. At last, fraction three was eluted with 4 ml of DCM:MeOH 1:1 (v:v), containing the most polar compounds of the neutral lipids like alcohols and GDGTs. After separation *n*-alkanes and ketones were quantified by GC-FID. Whereas, polar components of alcohols and GDGTs were dissolved in HEX:2-propanol 99:1 (v:v) and filtered through a 0.45 µm syringe filter to remove any particles before quantification by high performance liquid chromatography (HPLC) – mass spectroscopy (MS), homohopanes were quantified in the *n*-alkane fraction using GC-MS and an external hopane standard.

### 2.6.6 Gas Chromatography – Flame ionization detector

Extracted *n*-alkanoic acids (measured as FAME) and *n*-alkanes were identified and quantified on a GC-FID, using internal, external, and reference standards and their respective retention times. A 7890A gas chromatograph (Agilent Technologies) equipped with a DB-5MS fused silica capillary column (60 m, ID 250 µm, 0.25 µm film coupled to a 5 m, ID 530 µm deactivated fused silica precolumn) and a FID was used (Figure 9).

Extracted samples were dissolved in 100 µL HEX for injection with the cold on-column injection system. Injection volume was 1 µL of the sample solution. The GC was heated using the following temperature program: 60 °C for 1 min., 20 °C/min. to 150 °C, 6 °C/min. to 320 °C and a final hold time of 35min. Compounds were carried by a constant flow of helium of 1.5 µL min<sup>-1</sup>. In the FID the compounds were combusted with a fuel gas mixture of hydrogen and synthetic air.

In order to minimize contamination, the system was cleaned with two runs of HEX before each sample batch. Additionally, the syringe of the injection system was automatically cleaned with DCM and HEX before and after each injection.

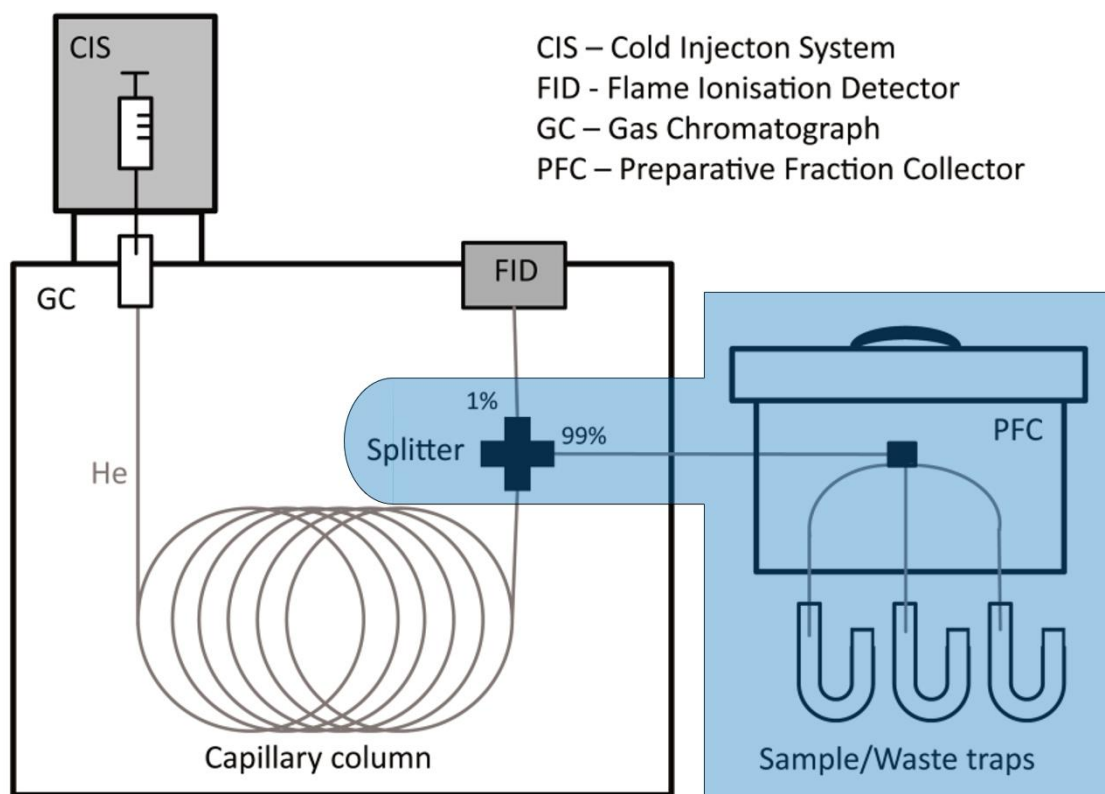


Figure 9: Building blocks of GC-FID (without blue box) and GC-PFC (with blue box) modified after Höfle (2015)

### 2.6.7 Gas Chromatography – Mass spectrometry

For identifying compounds in very low concentrations, i.e. hopanes, or without a specific reference standard, a GC-MS system was used. The setup consisted of an Agilent 6850 GC coupled to an Agilent 5975C MSD operating in electron impact mode with an ionization energy of 70 eV. The GC was equipped with a fused silica capillary column (Restek Rxi-1ms, length 30 m; 250  $\mu\text{m}$  ID, film thickness 0.25  $\mu\text{m}$ ). Compounds dissolved in HEX were injected in split-less mode in the injector held at 280  $^{\circ}\text{C}$ , with an injection volume of 1  $\mu\text{L}$ . Helium was used as the carrier gas at a constant flow rate of 1.2 mL/min. The GC temperature program was as follows: 60  $^{\circ}\text{C}$  start temperature, held for 3 min, increased to 150  $^{\circ}\text{C}$  with a rate of 20  $^{\circ}\text{C min}^{-1}$ , increased further to 320  $^{\circ}\text{C}$  with a rate of 4  $^{\circ}\text{C min}^{-1}$  and finally held at 320  $^{\circ}\text{C}$  for 15 min. The source temperature of the MS was set to 230  $^{\circ}\text{C}$  and the quadrupole to 150  $^{\circ}\text{C}$ . After GC separation, compounds were fragmented into ions, accelerated, deflected and finally their mass to charge ratio ( $m/z$ ) was determined in full-scan mode.

In order to minimize contamination, before every batch, a cleansing run with pure HEX was performed. In addition, the syringe for sample injection was automatically cleaned with DCM and hexane before and after each injection.

### 2.6.8 High-performance liquid chromatography – Mass spectrometry of GDGTs

GDGT were analyzed after a slightly modified protocol from Hopmans et al. (2016), using an Agilent 1200 series HPLC system with two consecutively linked UPLC silica columns in series (Waters Acquity BEH HILIC, 2.1 x 150 mm, 1.7  $\mu$ m) and a 2.1 x 5 mm pre-column of the same material, maintained at 30 °C. The HPLC setup was connected to an Agilent 6120 MSD, allowing an atmospheric pressure chemical ionization (APCI) interface linkage to a single quadrupole MS. Two mobile phases were used, mobile phase A (HEX/2-propanol; 99:1, v/v) was used 5 minutes into each sample run and for 15 min prior to the next sample to re-equilibrate with 18 % of mobile phase B (HEX/2-propanol/chloroform; 89:10:1, v/v/v). After sample injection (20  $\mu$ L) and 25 min isocratic elution with 18 % mobile phase B the proportion of B was linearly increased to 50 % within 25 min, and thereafter to 100 % for the next 30 min. Flow rate was 0.22 ml/min and a maximum back pressure of 220 bar was obtained. Total run time was 100 min.

At the APCI-MS a positive-ion mode was used with a selective ion monitoring for their (M+H)<sup>+</sup> ions or ion-source fragmentation products to identify GDGTs (Schouten et al., 2007) and OH-GDGTs (Liu et al., 2012). APCI spray-chamber conditions were as follows: nebulizer pressure 50 psi, vaporizer temperature 350 °C, N<sub>2</sub> drying gas flow 5 l/min and 350 °C, capillary voltage (ion transfer tube) -4 kV and corona current +5  $\mu$ A.

GDGT concentrations were determined using the response factor from a C<sub>46</sub> GDGT standard, by integrating respective peak areas. Due to a lack of appropriate standards, individual relative response factors between the different GDGTs and the C<sub>46</sub> were not determined. The obtained concentrations should therefore be regarded as being only semi-quantitative.

## 2.7 Compound specific radiocarbon dating of fatty acids

### 2.7.1 Pre-extraction sample preparation

FAs were extracted, separated, and purified using a sequence of wet chemical techniques and chromatographic methods (Figure 7b).

### 2.7.2 Lipid extraction

Organic compounds were extracted and separated using a modified Bligh and Dyer approach in combination with liquid chromatography over a silica column (Akondi et al., 2017; Bligh and Dyer, 1959; Slater et al., 2006b; Wakeham et al., 2006).

To maximize lipid yields, the entire sediment samples (Table 2) were used for extraction. Extraction was carried out overnight (~18 hours), at room temperature with a single-phase solution of DCM:MeOH:PO<sub>4</sub>B in a volumetric ratio of 1:2:0.8. The phosphate buffer (PO<sub>4</sub>B) was prepared by dissolving 4.35 g of dibasic potassium phosphate in 500 mL of nano-pure water. The buffer was then set to a pH-value of ~7.4 using HCl. After the initial extraction, the remaining sediment was rinsed twice with 100 mL of the extraction solution and ultrasonicated. The resulting solvent lipid extract was filtered and collected in a separatory funnel. DCM and purified H<sub>2</sub>O were added to the separatory funnel until a ratio of DCM:MeOH:[PO<sub>4</sub>B+H<sub>2</sub>O] in 1:1:0.9 (v:v:v) was reached. Additionally, KCl was added to enhance the separation process of the resulting two-phase system. Subsequently, the solvent lipid extract contained in the DCM phase was drained, and the aqueous phase was re-extracted twice with DCM, before the combined DCM extracts were evaporated by a rotary evaporator.

### 2.7.3 IPL separation through liquid chromatography

Depending on their visual appearance the TLEs were separated into 2 to 5 aliquots, to minimize the risk of column overloading in the following separation procedure. The separation of the lipids into three different fractions was achieved according to their polarity reflected in their interaction with the silica column during column chromatography (Table 4). For the column, the setup is described in the section 2.6.3. Compounds were eluted with three different solvents starting from low to high polarity. First, non-polar compounds and triacylglycerols (TAG) were eluted with 4 ml DCM, followed by free FA and glycolipids (GL) with 4 ml Acetone and by polar lipids (PL) such as phospho- and amino lipids with 4 ml MeOH. To simplify the following working process the aliquots of the different polarity fractions were re-combined.

<u>Solvent</u>	<u>Fraction</u>
DCM	neutral lipids (NL)
Acetone	glycolipids (GL)
MeOH	polar lipids (PL)

Table 4: During IPL separation used solvents and related fractions.

### 2.7.4 Derivatization of fatty acids

Ester bonds between core-lipids and the FA side-chains were broken by mild alkaline saponification with 0.5 M KOH in MeOH:H<sub>2</sub>O 9:1 (v:v) for 2 hours at 80°C (compare: section 2.6.2), in all three fractions. Neutral lipids of the non-polar fraction were extracted after saponification with HEX, this fraction was dried and stored. The residual of the non-polar-, GL-, and PL-fraction were re-acidified and FA were extracted with DCM. Subsequently, the FAs were methylated into FAMES and cleaned via silica column. The procedures used were equivalent to the ones used for determination of biomarker abundances.

### 2.7.5 Gas Chromatography – Preparative fraction collector

Purified FAME fractions extracted from large samples for CSRD contained a multitude of different compounds varying in chain lengths, degrees of unsaturation, and isomers. In order to obtain pure single compound FA fractions, samples were purified using a gas chromatograph coupled to a preparative fraction collector (GC-PFC; Eglinton et al., 1996).

The schematic setup is shown in Figure 9. A traditional GC-FID unit is coupled with an additional PFC. GC, and FID working principles and temperature program were as described in section 2.6.6. In the GC-PFC setup, a Gerstel Cooled Injection System (CIS) connected to an Agilent HP6890N GC equipped with a Restek Rtx-XLB fused silica capillary column (30 m, 0.53 mm diameter, 1.5  $\mu$ m film thickness) was used. In this setup, a splitter separates the gas flow from the capillary column, causing a distribution of the flow to 1 % to the FID and 99 % to a Gerstel PFC. The FID unit determines retention times of target compounds. The PFC was equipped with six pre-combusted glass sample traps and one waste trap. Every outlet of a trap is connected to an individual magnetic valve, of which only one can be opened at a given time. All traps were kept at room temperature, allowing the compounds to condense in the traps while entering. The PFC top unit was constantly kept at 340 °C (maximum temperature reached at the GC) to prevent any compound precipitation before the eluent entered the glass traps. Purified compounds were later transferred with DCM from the glass traps to pre-combusted glass vials.

For purification, the fatty acid fractions were dissolved in HEX. Depending on the concentration in the solution, it was injected up to 100 times (100 GC runs) with 5 $\mu$ L each time. The degree of dilution was chosen according to target compound concentrations, aiming for maximum compound concentrations while staying below 5  $\mu$ g for a single compound to prevent column overloading and coelution. The purity of the isolated single compounds was evaluated by GC-FID and GC-MS.

In order to minimize contamination, the syringe of the CIS was automatically cleaned with DCM and hexane before and after each injection. In addition, before every new sample the deactivated glass liner in the CIS was exchanged and a cleansing run with pure hexane was performed.

### 2.7.6 Radiocarbon measurements

Purified compounds were measured as CO<sub>2</sub> gas at the MICADAS-facility of the Alfred-Wegener-Institute in Bremerhaven, Germany. The purified compounds were washed into tin capsules for liquids (25  $\mu$ l volume, 2.88x6x0.1 mm, Elementar) three times using DCM. Volumes were chosen appropriately to generate sample sizes between 10 and 100  $\mu$ g C. After the solvent was completely evaporated, tin

capsules were folded and combusted using a vario isotope select elemental analyzer. Resulting CO<sub>2</sub> gas was directly injected into the MICADAS ion source under constant flow and pressure. Samples were corrected for both machine blank against <sup>14</sup>C free CO<sub>2</sub> gas using BATS software (Wacker et al., 2010) and procedural blanks (compare: below).

### 2.7.7 Accelerator mass spectrometry

Radiocarbon dating was performed on an accelerator mass spectrometer using the Mini Carbon Dating System (MICADAS 15; Wacker et al., 2010), produced by Longplus AG. Both graphitized sediment (compare: section 2.5) samples as well as the purified FAME were measured on this system. The system uses an optimized cesium ion source, allowing sample sizes as small as 10 µg C. Graphitized bulk OM samples were loaded as pressed targets directly into the AMS. Whereas, prepared samples for CSRD were combusted in an EA (compare: section 2.5). Generated CO<sub>2</sub> gas was trapped on a zeolite trap in the Gas Ion Source Interface. After completed combustion, the CO<sub>2</sub> gas was released from the trap by heating the trap to 450°C. Emitting CO<sub>2</sub> gas was quantified manometrically after desorption from the trap and subsequently diluted to 5 % in He. The resulting gas mixture was directly injected into the AMS ion source under constant flow and pressure.

In the AMS, both sample types were ionized by an accelerated ion beam (Cs<sup>+</sup>) causing negatively charged carbon ions to shutter of the samples, allowing a discrimination of <sup>14</sup>C against <sup>14</sup>N. Subsequently, all ions are accelerated into the focusing device and deflected by an injector magnet to split off non-carbon-ions. Remaining carbon ions are accelerated in a tandem accelerator unit and bypass an electron stripper, scattering remaining molecules. Subsequent carbon atoms are further accelerated and deflected by their mass due to a second magnet to remove remaining molecule fragments. Emerging carbon ion beams are quantified by their amperage using a Faraday cup.

All radiocarbon data were normalized relative to the reference standard oxalic acid II (NIST 4990c) and expressed in fraction of modern carbon (F<sup>14</sup>C) for post-bomb samples to avoid confusion with different terms (Reimer et al., 2004):

$$F^{14}C = \frac{(^{14}C/^{12}C_{sample})}{(^{14}C/^{12}C_{standard})} \quad (1)$$

### 2.7.8 Blank correction

Due to the extremely small sample size and extensive wet chemical processing, the obtained <sup>14</sup>C data is potentially influenced by carbon contamination and procedural blanks. In order to obtain correct

radiocarbon data for the investigated samples, a blank correction was performed. The carbon contamination from sample processing is too low to be determined directly ( $< 10 \mu\text{g C}$ ). Influence of the blank carbon on the mass and  $F^{14}\text{C}$  of samples increases with decreasing sample size. Therefore, it is necessary to perform a secondary blank correction. Sample processing blanks ( $b$ ), including wet chemical processing, sample combustion and measurement, were determined by processing standards ( $std$ ) of known  $^{14}\text{C}$  composition. FAMEs extracted from Messel Shale ( $F^{14}\text{C} = 0$ ; immature Eocene oil Shale from western Germany) and Apple Peel ( $F^{14}\text{C} = 1.031 \pm 0.004$ ) were processed similarly to the investigated samples. Assuming constant contamination it is possible to indirectly determine the processing blank by analyzing FAMEs of different masses ( $m$ ) and known  $^{14}\text{C}$  composition, using a standard mass balance (Hwang and Druffel, 2005):

$$\begin{aligned} F^{14}C_{std+b} * m_{std+b} &= F^{14}C_{std} * m_{std} + F^{14}C_b * m_b \\ &= F^{14}C_b * m_b + F^{14}C_b * (m_{std+b} - m_b) \end{aligned} \quad (2)$$

Assuming a constant procedural blank equation (2) can be expressed as a linear equation, with  $1/m_{std+b}$  representing the x-variable and  $F^{14}C_{std+b}$  the y-variable. The resulting y-intercept of the linear equation being the true  $F^{14}C_{std}$  value of the used standard and relating in  $(F^{14}C_b - F^{14}C_{std})$  as the slope of the linear regression (Hwang and Druffel, 2005):

$$F^{14}C_{std+b} = (F^{14}C_b - F^{14}C_{std}) * m_b * \frac{1}{m_{std+b}} + F^{14}C_{std} \quad (3)$$

Therefore, linear regression lines for multiple fossil and modern standards were fitted to determine the blank (Hwang and Druffel, 2005). A Bayesian regression model was employed to account for measurement uncertainties and to calculate the intercepts ( $x_0; y_0$ ) of the two regression lines, to determine  $1/m_b$  and  $F^{14}C_b$ . The calculated carbon contamination accounted for a mass of  $1.3 \pm 0.1 \mu\text{g C}$  with a  $F^{14}\text{C}$  of  $0.54 \pm 0.05$  (Figure 10). The obtained blank signature ( $F^{14}C_{blank}; m_{blank}$ ) was later used to correct for the measured data ( $F^{14}C_{sample}; m_{sample}$ ) of the samples to obtain true  $F^{14}\text{C}$ -values ( $F^{14}C_{true}; m_{true}$ ) of the compounds (Hwang and Druffel, 2005; Sun et al., 2019; Wacker and Christl, 2011) using the equations provided by Sun et al. (2019):

$$F^{14}C_{sample} = F^{14}C_{true} * \frac{m_{true}}{m_{sample}} + F^{14}C_{blank} * \frac{m_{blank}}{m_{sample}} \quad (4)$$

Furthermore,  $F^{14}\text{C}$ -values of the FAMEs ( $F^{14}C_{true}$ ) were corrected for the methyl group added during methylation to the FAs ( $F^{14}C_{FA}$ ). The used MeOH had a  $F^{14}\text{C}$ -value of  $0.0028 \pm 0.0001$  ( $F^{14}C_{MeOH}$ ). The

added methyl group was accounted for by the ratio of the total number of carbon atoms after methylation ( $n$ ) in relation to the individual carbon atoms of the FAs ( $n-1$ ), leading to the methyl corrected  $F^{14}C_{FA}$  of the FAs:

$$F^{14}C_{FA} = F^{14}C_{MeOH} * \frac{1}{n} + F^{14}C_{true} * \frac{n-1}{n} \quad (5)$$

In order to estimate combined uncertainties for these multistep correction procedures, an error propagation was conducted after Wacker and Christl (2011).

### 2.7.9 Correction for known contaminations

Compound purification with GC-PFC was very successful. However, at 86-89 cm for the FAME  $C_{16:0}$  some contamination from 86-89 cm FAME  $C_{16:1}$  occurred due to a broadening of the 86-89 cm  $C_{16:1}$  peak retention time, leading to co-elution with 86-89 cm FAME  $C_{16:0}$ . As  $F^{14}C$  of 86-89 cm  $C_{16:1}$  was determined independently and the degree of contamination (respective masses:  $m$ ) was known,  $F^{14}C$  values for 86-89 cm  $C_{16:0}$  were corrected using the following formula:

$$m_{measured} * F^{14}C_{measured} = m_{C_{16:0}} * F^{14}C_{C_{16:0}} + m_{C_{16:1}} * F^{14}C_{C_{16:1}} \quad (6)$$

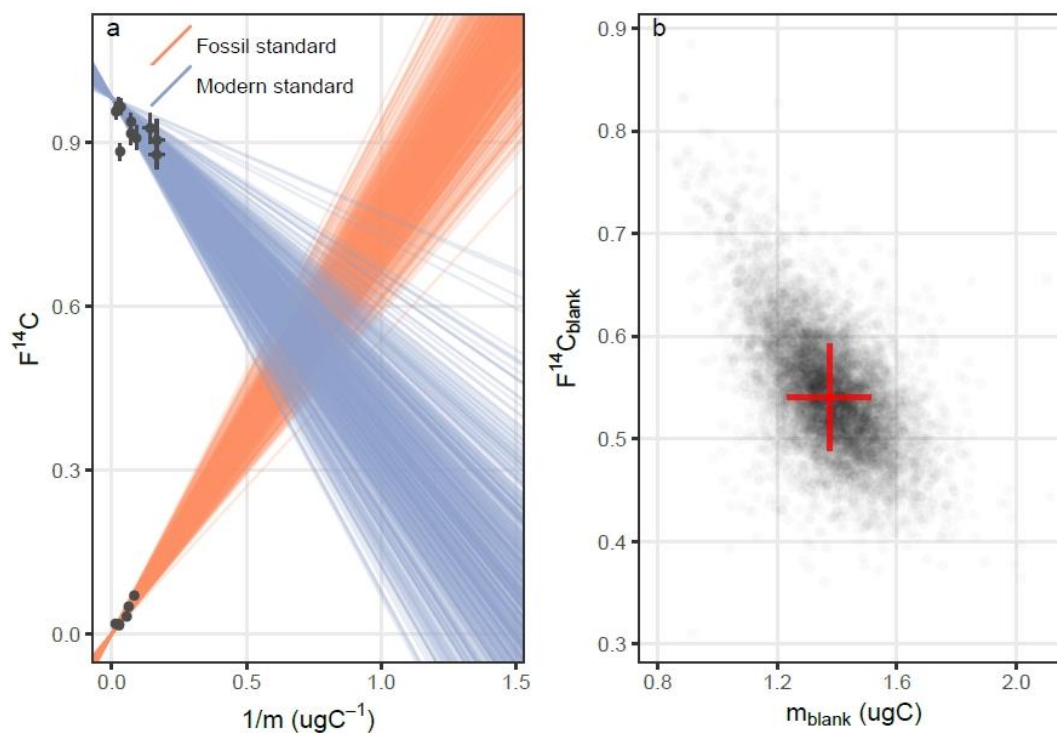


Figure 10: Blank determination for this study of  $1.3 \pm 0.1 \mu\text{g C}$  with a  $F^{14}C$  of  $0.54 \pm 0.05$ . a) Plot of all intersections of the two possible regression lines for modern (blue) and carbon free (orange) standards. The intersections are the paired estimates of  $F^{14}C$  and  $m$ . b) Highest probability of blank  $F^{14}C_{\text{blank}}$  and  $m_{\text{blank}}$ , indicated by red cross.

## 2.8 Intact polar lipid analysis

Intact polar lipid (IPL) analysis was performed to confirm the separation of the different compound classes and to determine precursor lipids of the  $^{14}\text{C}$  dated FAs. Aliquots were taken from each fraction after silica-column separation subsequently to the performed modified Bligh and Dyer extraction for CSRD (Figure 7d). For sample depths 0-3 cm and 133-136 cm 1 % splits of the TLE were taken and for sample depths 8 cm, 13 cm and 83.5 cm separate extractions were performed following the protocol described above and 100 % of the TLE was taken for IPL analysis. This way, injection volumes could be normalized to similar sample sizes (respective 0.12 to 0.18 g sediment per injection), to allow comparable results.

### 2.8.1 IPL – Analysis with Q-TOF

IPL analysis was carried out using the previously described protocol of Sturt et al. (2004) with improved detection and chromatographic separation techniques after Wörmer et al., 2013 on a Bruker maXis Plus ultra- high-resolution quadrupole time-of-flight mass spectrometer (Q-TOF) with an electrospray ionization source coupled to Dionex Ultimate 3000RS ultra-high-pressure liquid chromatography. Aliquots of the individual fractions were dissolved in DCM:MeOH in a ratio of 9:1 (v:v) and measured by hydrophilic interaction chromatography (Hilic) mode to check the separation of phospholipids, glycolipids, and aminolipids. Hilic separation was achieved with an Waters Acquity UPLC BEH amide column (1.7  $\mu\text{m}$ , 2.1 x 150 mm) at 40°C with the following solvent gradient: 99 % A and 1 % B for 2.5 min at a flow of 0.4 mL min<sup>-1</sup> (A: acetonitrile:DCM, 75:25, 0.01 % formic acid, 0.01 % ammonium hydroxide; B: MeOH:H<sub>2</sub>O, 50:50, 0.4% formic acid, 0.4 % ammonium hydroxide), ramping to 5 % B at 4 min, 25 % B at 22.5 min and 40 % B at 26.5, held for 1 min and equilibrated to initial conditions for 8 min. Additionally, samples were analyzed by reverse phase chromatography to also check the separation of more apolar compounds such as diacyl and triacyl glycerol lipids after. Reverse phase separation was achieved on a Waters Acquity UPLC BEH C18 column (1.7  $\mu\text{m}$ , 2.1 x 150 mm) at 65 °C with the following solvent gradient: 2 % B for 2 min at a flow of 0.4 mL min<sup>-1</sup> (A: MeOH:H<sub>2</sub>O, 85:15, 0.04 % formic acid, 0.1 % ammonium hydroxide; B: 2-propanol:MeOH, 50:50, 0.04 % formic acid, 0.1 % ammonium hydroxide), ramping to 15 % B at 2.1 min, 85 % B at 20 min and 100 % B at 20.5, held for 7.5 min and equilibrated to initial conditions for 8 min.

Compounds were identified based on their retention-time and mass spectral information including specific fragmentation patterns in positive and negative ion mode using Bruker Compass DataAnalysis. Absolute concentrations of phospholipids, amino-lipids, and GL were determined in

positive ionization mode. Notably, the individual compounds were not response factor corrected, hence, obtained values are only semi-quantitative. Identification of side chain FA variations for GL and amnio-lipids was achieved in positive ionization mode whereas for PL side chains were identified in negative ionization mode. Relative TAG abundances were assessed using reversed phase chromatography. Corresponding FA of the five most abundant IPLs were identified by characteristic mass fragments and retention-times of precursor IPLs (Schubotz et al., 2009; Sturt et al., 2004).

## 2.9 Biomarker Indices

Measured biomarker abundances were displayed as ratios of different compounds within one sample rather than absolute values in order to minimize uncertainties. All measured compound quantities can be found in the appendix.

### 2.9.1 Homohopanes

Homophones were analyzed in order to estimate fractions of freshly produced biomass versus OM from a petrogenic origin in the local sediment. Thus, the abundance of hopanes from biological sources, typically exhibiting the stereochemical configuration 17 $\beta$ ,21 $\beta$  (H), 22R (Rohmer et al., 1992) was compared to that of the “geological” isomers 17 $\beta$ ,21 $\alpha$ S, 17 $\beta$ ,21 $\alpha$ R, 17 $\alpha$ ,21 $\beta$ S, and 17 $\alpha$ ,21 $\beta$ R (Wenger and Isaksen, 2002), which form during diagenesis and catagenesis due to the transformation of the unfavorable stereochemical configuration of the biological configuration of 17 $\beta$ ,21 $\beta$  (H), 22R. Hence,  $f_{\beta\beta}$  for C<sub>31</sub> homohopanes was calculated using the following formula (Meyer et al., 2019):

$$f_{\beta\beta} = \frac{C_{31}\beta\beta R}{C_{31}\beta\beta R + C_{31}\alpha\beta S + C_{31}\alpha\beta R + C_{31}\beta\alpha S + C_{31}\beta\alpha R} \quad (7)$$

to qualitatively determine relative contributions of biological versus petrogenic input.

Additionally, the maturity of the petrogenic fraction was determined using the ratio of the biological C<sub>31</sub> $\alpha\beta$ R configuration, which is found in bacteriohopanetetrols, versus its converted equilibrium mixture of biological (C<sub>31</sub> $\alpha\beta$ S) and its mature, converted (C<sub>31</sub> $\alpha\beta$ R) configuration. In most crude oils the C<sub>31S/R</sub> is stable at ~0.58-0.62 (Peters et al., 2005):

$$C_{31S/R} = \frac{C_{31}\alpha\beta S}{C_{31}\alpha\beta S + C_{31}\alpha\beta R} \quad (8)$$

### 2.9.2 *n*-Alkanes

Biologically produced *n*-alkanes have an odd over even dominance in their chain-lengths. However, through maturation and/or biodegradation this predominance is lost. Thus, the carbon preference index for the aliphatic *n*-alkanes  $C_{24}$  to  $C_{34}$  ( $CPI_{alk}$ ) can be used for the evaluation of the OM maturity (Bianchi and Canuel, 2011):

$$CPI_{alk} = 0.5 * \left( \frac{C_{25} + C_{27} + C_{29} + C_{31} + C_{33}}{C_{24} + C_{26} + C_{28} + C_{30} + C_{32}} + \frac{C_{25} + C_{27} + C_{29} + C_{31} + C_{33}}{C_{26} + C_{28} + C_{30} + C_{32} + C_{34}} \right) \quad (9)$$

### 2.9.3 Fatty Acids

Similar to the  $CPI_{alk}$  the  $CPI_{FA}$  was determined for alkanolic acids. However, for biosynthetic reasons “fresh” FAs display a strong even over odd predominance (Bianchi and Canuel, 2011):

$$CPI_{FA} = 0.5 * \left( \frac{C_{16:0} + C_{18:0} + C_{20:0} + C_{22:0} + C_{24:0}}{C_{15:0} + C_{17:0} + C_{19:0} + C_{21:0} + C_{23:0}} + \frac{C_{16:0} + C_{18:0} + C_{20:0} + C_{22:0} + C_{24:0}}{C_{17:0} + C_{19:0} + C_{21:0} + C_{23:0} + C_{25:0}} \right) \quad (10)$$

Additionally, the terrestrial aquatic ratio ( $TAR_{FA}$ ) was determined by quantifying the relative abundance of long-chained fatty acids versus short-chained fatty acids. This ration is used to estimate the relative contributions from terrestrial and aquatic plants (Meyers, 1997):

$$TAR_{FA} = \frac{C_{24:0} + C_{26:0} + C_{28:0}}{C_{12:0} + C_{14:0} + C_{16:0}} \quad (11)$$

### 2.9.4 GDGTs

In order to estimate fluviually transported terrestrial soil OM input to the sediment, the BIT-index was determined (Hopmans et al., 2004):

$$BIT \text{ index} = \frac{GDGT \text{ I} + GDGT \text{ II} + GDGT \text{ III}}{Crenarchaeol + GDGT \text{ I} + GDGT \text{ II} + GDGT \text{ III}} \quad (12)$$

### 2.9.5 Isotope mass balance calculation

Modern ( $f_{marine}$ ) and fossil ( $f_{fossil}$ ) contribution of the bulk organic matter (Equation 13) and extracted FAs (Equation 14) used for CSRD, were calculated using an isotope mass balance calculation of a

modern ( $F^{14}C_{\text{modern}}$ ) and a fossil endmember. Sample radiocarbon signatures ( $F^{14}C_{\text{Bulk}}$ ;  $F^{14}C_{\text{FA}}$ ) were determined AMS (White et al., 2008):

$$F^{14}C_{\text{Bulk}} = f_{\text{marine}} * F^{14}C_{\text{GLFA 14:0}} + (1 - f_{\text{marine}}) * F^{14}C_{\text{fossil}} \quad (13)$$

$$F^{14}C_{\text{FA}} = f_{\text{marine}} * F^{14}C_{\text{GLFA 14:0}} + (1 - f_{\text{marine}}) * F^{14}C_{\text{fossil}} \quad (14)$$

$$f_{\text{fossil}} = 1 - f_{\text{marine}} \quad (15)$$

### 2.9.6 Sediment and mass accumulation rates

Sediment accumulation rates (SAR) and TOC mass accumulation rates of total OM ( $MAR_{\text{TOC}}$ ) were calculated on the basis of the age model of Szczuciński, sediment density ( $\rho_{\text{Sed}}$ ), and TOC content ( $TOC_{\text{wt}\%}$ ), determined by the isotope mass balance:

$$SAR = \frac{\Delta \text{depth}}{\Delta \text{age}} \quad (16)$$

$$MAR_{\text{TOC}} = SAR * \rho_{\text{Sed}} * TOC_{\text{wt}\%} \quad (17)$$

## 2.10 Supplementary data sets

Mean seasonal temperature was calculated using temperature measurements obtained at Svalbard Airport, provided by the eKlima database of the Norwegian Meteorological Institute ([www.met.no](http://www.met.no)).

Total organic carbon, total nitrogen, and bulk  $\delta^{13}C$  were provided by Szczuciński (2019, unpublished data, personal communication, AMU). TOC/N data were obtained by Szczuciński, Dominiczak, Woszczyk, and Forwick, using a Vario Max CNS analyzer. Each sample was analyzed in duplicate. Samples were homogenized, then analyzed for TC, TS and TN. The accuracy of all the measurements was >96 %. Subsequently, the samples were treated with HCl to remove carbonates and analyzed again to obtain TOC. Bulk  $\delta^{13}C$  data were obtained by Szczuciński, Apolinarska, Dominiczak, and Forwick using an Elemental Analyser Flash EA 1112HT Series with mass spectrometer Thermo Delta V Advantage in flow mode. Samples were homogenized and the carbonates were removed with HCl.

Additionally, a bathymetry map of Hornsund Fjord was provided by Forwick (2019, unpublished data, personal communication, UiT).

### 3. Results

#### 3.1 Sediment and mass accumulation rates

Linear sediment accumulation rates derived from the age model varied significantly and showed three distinctive zones (Figure 11). For the complete core, SAR was on average  $>2.4 \text{ cm yr}^{-1}$ . In the topmost 19 cm SARs were between  $0.5$  to  $1.2 \text{ cm yr}^{-1}$ . In a transitional zone down to 43.5 cm SAR was constant at  $3.0 \text{ cm yr}^{-1}$ . Below 43.5 cm SAR reached values as high as  $6.3 \text{ cm yr}^{-1}$ , with a mean of  $4.8 \text{ cm yr}^{-1}$  and some irregularities as low as  $3.3 \text{ cm yr}^{-1}$ .

OM mass accumulation rates were expressed in  $\text{MAR}_{\text{TOC}}$  closely following the SAR patterns, likewise resulting in a zonation into three sections. Above 19 cm  $\text{MAR}_{\text{TOC}}$  were between  $100$  and  $220 \text{ g C m}^{-2} \text{ yr}^{-1}$ . In the transitional zone until 43.5 cm,  $\text{MAR}_{\text{TOC}}$  ranged from about  $480$  to  $670 \text{ g C m}^{-2} \text{ yr}^{-1}$  and below values rose to a rates of  $700 \text{ g C m}^{-2} \text{ yr}^{-1}$  to over  $1400 \text{ g C m}^{-2} \text{ yr}^{-1}$ .

#### 3.2 Bulk organic matter

TOC/N and  $\delta^{13}\text{C}$  data were provided by Szczuciński (2019, personal communication, UAM; Figure 11). Within the top most 21 cm of the core, TOC/N ratio showed a distinctive decrease ranging from 18.26 at 21 cm to 13.36 at 3 cm. From 21 cm downcore TOC/N values had an increasing variability toward higher values, especially between 60 cm and 80 cm core depth, where a pronounced increase is visible. Within this range, values did not drop below 16.73 (at 87 cm) but increased up to 21.51 (at 141 cm) within the mid-range of the variability of the entire data set. A maximum occurred between 60 and 80 cm, where C/N values were as high as 23.42 at 63 cm.

Bulk OM showed a distinctive increase in conventional age within the topmost 40 cm, where radiocarbon ages range from as young as  $18,730 \pm 59$  conventional  $^{14}\text{C}$  years B.P. at 4.5 cm to  $27,790 \pm 270$  conventional  $^{14}\text{C}$  years B.P. at 38-40 cm depth (Figure 11). Below 40 cm the OM  $^{14}\text{C}$  ages remained rather constant, but with some variations ranging from  $22,820 \pm 160$  conventional  $^{14}\text{C}$  years B.P. at 50-52 cm up to  $27,377 \pm 104$  conventional  $^{14}\text{C}$  years BP at 60 cm.

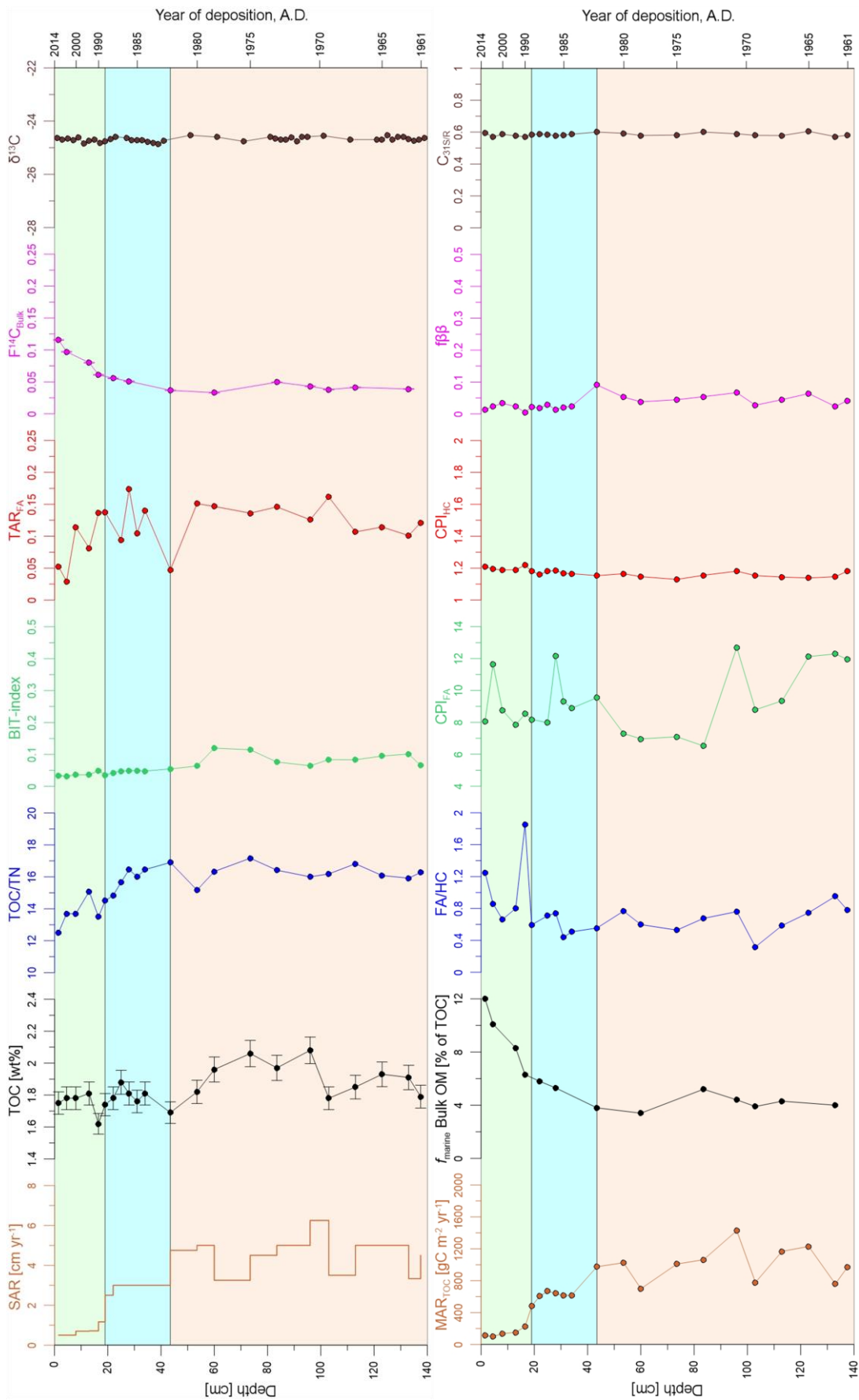


Figure 11: Biomarker indices of HH14-897-MF-GC. Separation different sediment depths according to their SAR and the expected diagenetic conditions. Green box: low SAR with high remineralization rates; Blue box: medium SAR with medium remineralization rates, Orange box: High SAR with low rates of remineralization.

### 3.2.1 *n*-Alkanes

Throughout the entire core, *n*-alkanes showed rather constant distribution patterns (Figure 12). The most striking feature of the *n*-alkane distribution is a low odd over even predominance of the aliphatic *n*-alkanes which is reflected in the low and rather constant  $CPI_{alk}$ -values, ranging from 1.13 to 1.23 (Figure 11). In all samples but the one from 16 cm, *n*-C<sub>19</sub> was the most abundant homologue ranging from  $0.458 \pm 0.022 \mu\text{g}$  to  $1.004 \pm 0.048 \mu\text{g}$ , whereas *n*-C<sub>21</sub> was most abundant at 16 cm with  $0.378 \pm 0.048 \mu\text{g}$ . Generally, abundances of *n*-alkanes decreased from these highest contents, gradually with decreasing and increasing chain length towards concentrations below the detection-limit at C<sub>13</sub> to C<sub>14</sub> for short-chain *n*-alkanes and C<sub>36</sub> to C<sub>38</sub> for long-chain *n*-alkanes respectively.

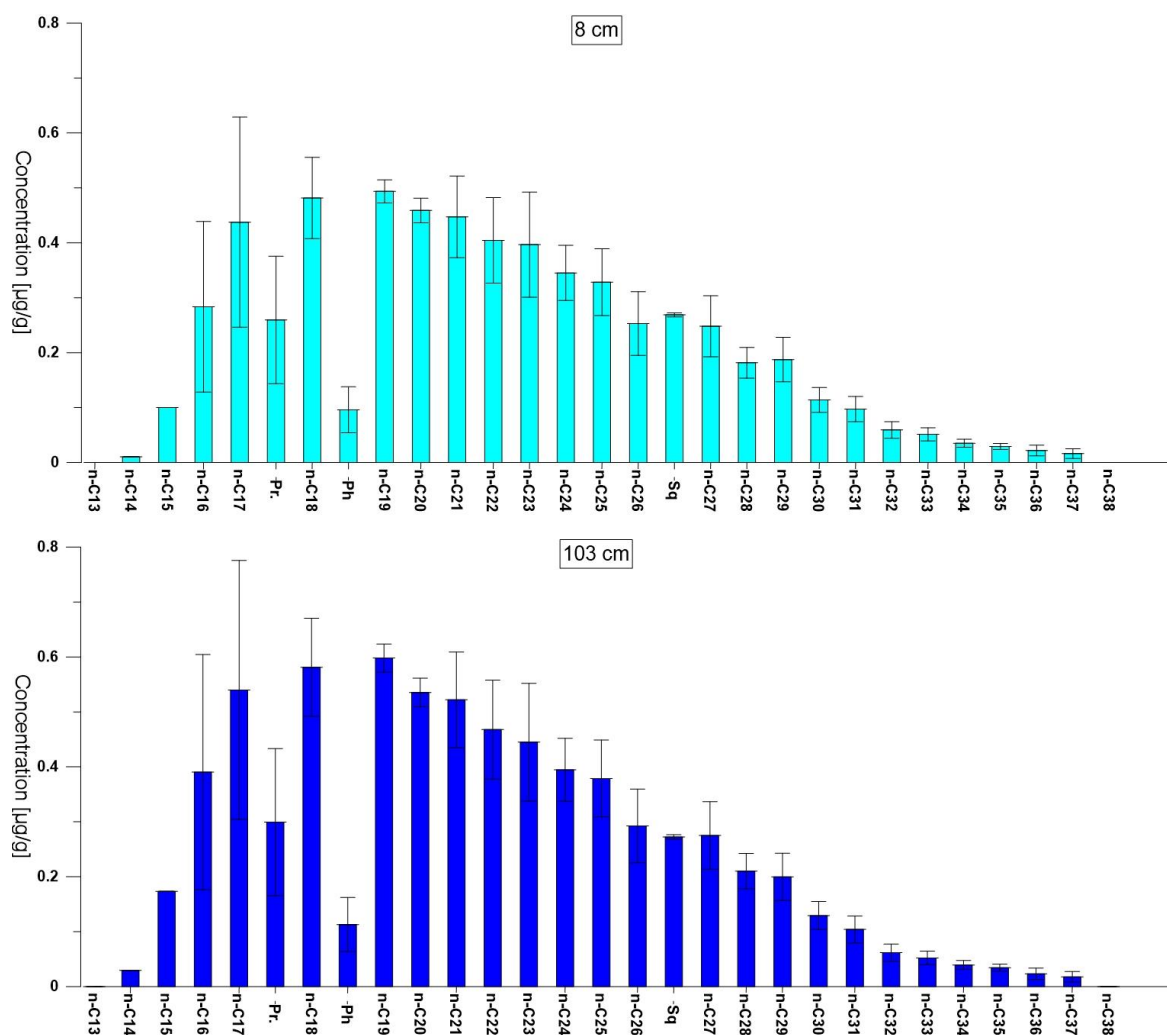


Figure 12: Typical *n*-alkane distributions of upper (8 cm) and lower (103 cm) core section, displaying uniformity within the core.

### 3.2.2 Fatty acids

FAs were analyzed and displayed as FAME. Their distribution was fairly constant throughout the core, although with some minor decreases in abundance downcore (Figure 13). A typical even over odd dominance was observed, resulting in  $CPI_{FA}$  values ranging from 6.52 to 12.70 (Figure 11). In all measured depths,  $C_{16:0}$  was the dominant homologue. FAs with  $>C_{30}$  were constantly below the detection limit. Short-chained FAs were substantially more abundant than long-chained FAs with a slight increase towards the core top. Terrestrial-aquatic ratios of FAs ( $TAR_{FA}$ ) ranged from 0.03 to 0.17 (Figure 11). The highest  $TAR_{FA}$  value of 0.17 was found at 28 cm and an overall shift to even lower  $TAR_{FA}$  values towards the core top was present.

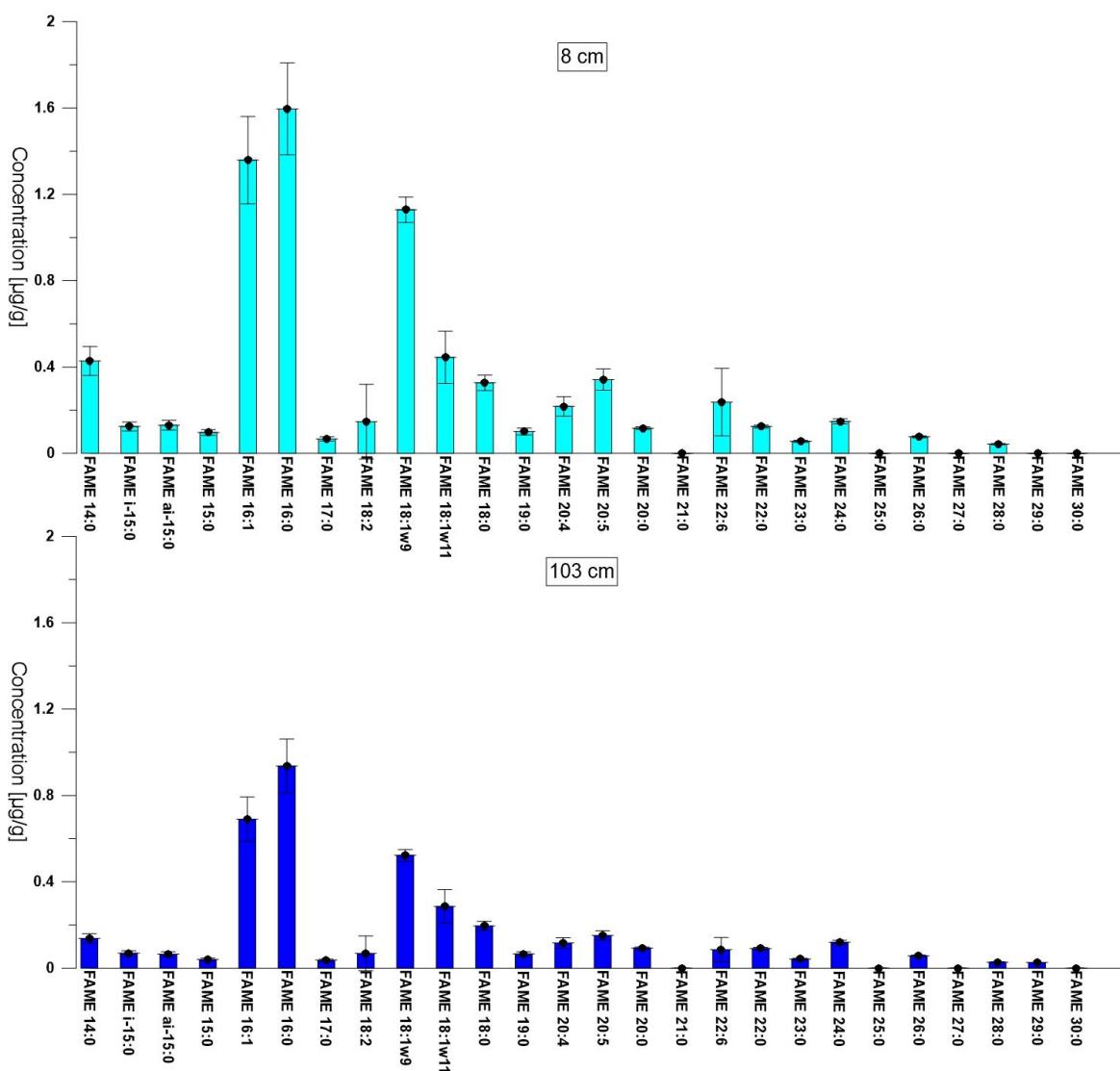


Figure 13: Typical FAME distributions of upper (8 cm) and lower (103 cm) core section, displaying uniformity within the core

### 3.2.3 Fatty acids in relation to *n*-alkanes

The summed abundance of saturated FAs versus aliphatic *n*-alkanes showed an increasing trend towards the core top, especially above 40 cm (Figure 11). Within this range, the ratio varied from as low as 0.44 at 31 cm up to 1.85 at 16.5 cm. Below 40cm these ratios ranged from 0.32 at 103 cm to 0.95 at 133 cm with increasing variability downcore and a local maximum at 16.5 cm.

### 3.2.4 Glycerol dialkyl glycerol tetraethers

GDGT assemblages were dominated by GDGT-0 ranging in content from 3.24 ng/g to 9.55 ng/g and crenarchaeol ranging from 2.62 ng/g to 7.42 ng/g. Both were consistently one to two orders of magnitude more abundant than the rest of the isoprenoid GDGTs as well as the branched GDGTs. The BIT index ranged from 0.06 to 0.12 below 53.5 cm core depth, peaking at 60 and 53.5 cm. Above this core depth, values were fairly stable and ranged between 0.05 and 0.03 with an overall slight decrease towards the core top (Figure 11).

### 3.2.5 C<sub>31</sub> Homohopanes

Overall, homohopane data showed very little variability (Figure 11).  $f\beta\beta$ -ratios were low with the highest value being 0.1 at 43.5 cm. Samples above 43.5 cm were even less variable than those down core and lower values constantly below 0.03. Below 43.5 cm,  $f\beta\beta$ -ratios decreased gradually with oscillating values ranging from 0.09 to 0.02. C<sub>31S/R</sub> values were very consistent between 0.57 and 0.60 throughout the core.

## 3.1 Intact polar lipids

IPL analysis was primarily performed to verify the separation of neutral total lipid extract (N-TLE; incl. TAGs), GL, and PLs. Contamination of TAGs into GL and PL fraction was determined qualitatively. The majority of TAGs eluted in the N-TLE fraction. However, a number of the TAGs were also found in the GL fraction. Detected TAGs in the GL fraction were primarily composed of C<sub>14:0</sub>, C<sub>16:0</sub>, C<sub>16:1</sub>, C<sub>18:0</sub>, C<sub>18:1</sub>, and C<sub>18:2</sub> FAs. Within the PL fraction TAGs were barely detected, of these associated FAs were C<sub>16:0</sub>, C<sub>18:0</sub>, C<sub>18:1</sub>, and C<sub>18:2</sub>.

Secondly, precursor IPLs of the PLFAs were quantified to allow a better understanding of the active bacterial communities in the sediment. Identified IPLs in the phospholipid fraction consisted of five

## Release and Remineralization of Ancient Carbon from Svalbard Glaciers

major and two minor groups, divided by their respective head groups (Figure 14). These were the phospholipids phosphatidylcholine (PC), phosphatidylethanolamine (PE), phosphatidyl-(N)-methylethanolamine (PME), phosphatidylglycerol (PG), diphosphatidylglycerol (DPG) and lyso- diphosphatidylglycerol (lyso-DPG) and a group belonging to the aminolipids, betaine lipids (BL). Presented values show the shares of these IPLs, normalized to the total of all quantified IPLs of the PL fraction. Relative abundances of the PL-IPLs were highly uniform throughout in all five analyzed sample depths. PC had highest relative abundances, ranging from 27 % to 33 %, followed by PME and PE with fairly similar abundances ranging from 19 % to 29% and 21 % to 25 %, respectively. PG and BL also showed similar quantities ranging from 7 % to 11 % and 6% to 11 %, repetitively. The two minor compounds were DPG and lyso-DPG, with relative abundances between 1 % to 4 % and 1 % to 2 %, respectively.

Due to the high conformity of the relative IPL abundances, additionally the average chain-lengths and number of double bonds were determined (Figure 15), to further investigate potential alterations in the bacterial communities with depth. Note that the following values both for average chain-length and number of double bonds, refer to MS fragments of two fatty acids as the analyzed fragments are still attached to the glycerol backbone.

The conformity downcore of the headgroups increased similarly with the average number of double bonds in their respective groups, showing only minor differences with increasing depth (Figure 15). Strongest shifts are observed within the upper most three samples, with exaptation of PG and DPG. PG, PC, and DPG increased their average number of double bonds slightly, from 1.5 to 1.8, 1.6 to 2.1,

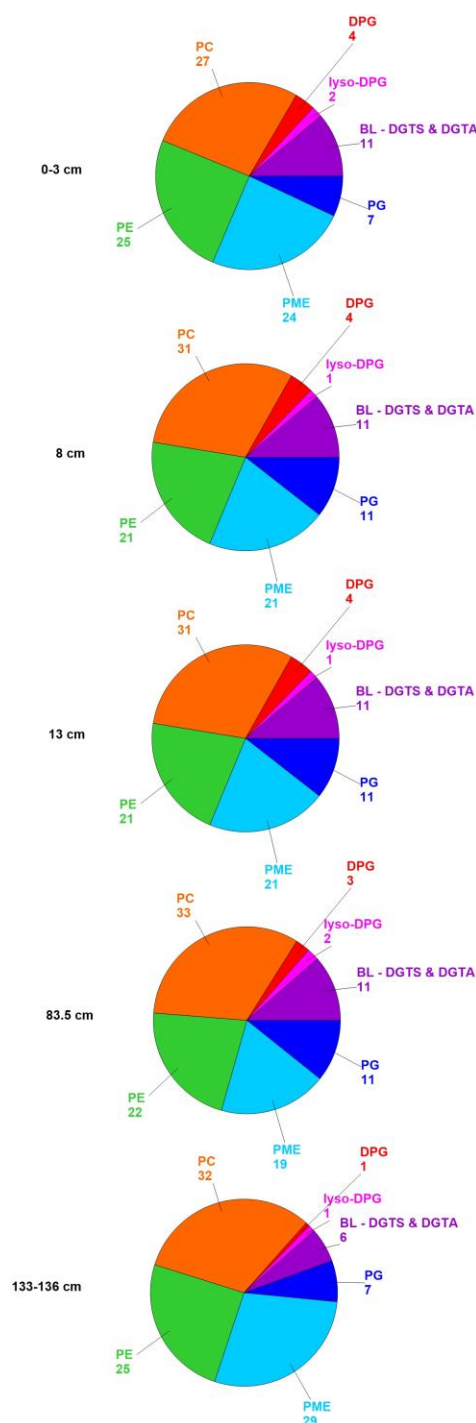


**Figure 14: Relative contributions of IPLs of the PL fraction separated for CSRD. Values in percent.**

and 1.0 to 2.0 respectively. PE was the only group which show a decrease in double bonds from an average of 2.2 at 0-3 cm to 1.4 at 133-136 cm. BL have shown stable average double bond values, ranging from 1.2 to 1.3. PME varied most widely from 1.3 to 2.3 respectively, with a mean of 1.9.

Overall, the average-chain lengths showed a more diverse picture compared to the number of double bonds. PG was most stable with only minor variations from C32.3 to C32.9, while DPG displayed an increase downcore from C31.3 to C33.4. PME, PE, and BL were even more diverse. BL and PME had minor variations with an overall downcore decrease, ranging from C32.1 to C33.6 and C34.8 to C32.1. The most pronounced changes occurred within PE with a distinctive decrease from C36.7 at 0-3 cm to C32.5 at 133-136cm, with a local increase at 83.5 cm. A distinctive decrease was also observed for PC, from 32.2 to 29.6.

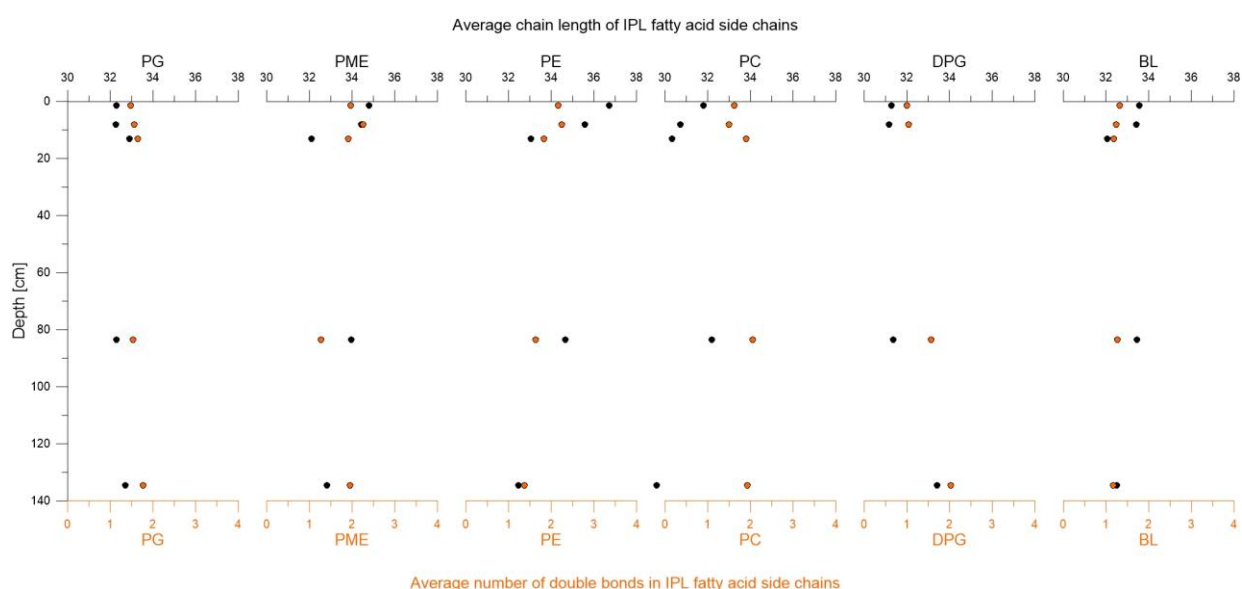


Figure 15: IPL headgroup related average number of double bonds (orange) and average chain-lengths (black) of one FA side chain. Values are related to fragments of two FA attached to one glycerol backbone.

### 3.2 Compound specific radiocarbon dating

All data were corrected for the isotopic signature of the methanol used for methylation as well as for contributions of blank carbon using the approaches described by e.g. Meyer et al. (2019). The mass and  $F^{14}C$  of the blank carbon were determined according to Sun et al. (2019). Error propagation was performed to fully account for uncertainties.

### 3.3.1 Glycolipid Fatty Acids

Individual glycolipid fatty acids (GLFA; Table 5) showed an overall decrease in age downcore, however, the decrease is not constant. Of the dated GLFA only the  $C_{14:0}$  at 0-3cm showed a modern-day  $F^{14}C$  signature of  $0.959 \pm 0.0098$  which equated to an age of  $334 \pm 67$  years, likely reflecting the Svalbard marine surface reservoir age of  $380 \pm 30$  years suggested by (Mangerud et al., 2006). All other dated GLFAs had  $F^{14}C$ -values way below their respective sedimentation age and exhibit significant variability, ranging from  $0.923 \pm 0.0079$  of  $C_{18:2+18:1}$  at 5-8 cm down to  $0.468 \pm 0.0048$  of  $C_{16:1}$  at 86-89 cm. In the individual sample depths, the GLFAs showed a distinct age pattern. The  $C_{18:2+18:1}$  were always the youngest fraction, with  $F^{14}C$  values ranging from  $0.698 \pm 0.0065$  to  $0.923 \pm 0.0079$ . By contrast,  $C_{16:1}$  was the oldest fraction in every sample with  $F^{14}C$ -values of  $0.469 \pm 0.0048$  to  $0.770 \pm 0.0061$ .  $C_{16:0}$  and  $C_{i+ai15:0}$  displayed intermediate  $F^{14}C$  values ranging between those of  $C_{18:2+18:1}$  and  $C_{16:1}$ . At 0-3 cm, 10-13 cm, and 133-136 cm  $C_{i+ai15:0}$  had significantly younger  $F^{14}C$ -values than  $C_{16:0}$ . At 5-8 cm and 86-89 cm  $C_{16:0}$  and  $C_{i+ai15:0}$  showed similar ages however, their  $2\sigma$  ranges overlap. Additionally,  $F^{14}C$  of 86-89 cm  $C_{16:0}$  was corrected (compare: Correction for known contaminations) for contamination from 86-89cm  $C_{16:1}$ , which occurred during the GC-PFC separation procedure.

### 3.3.2 Polar-Lipid Fatty Acids

Radiocarbon values of polar-lipid fatty acids (PLFA) are displayed in Table 5. FA yields after extraction, separation, and purification were, in many cases, close to or below the operational limits of  $10 \mu\text{g C}$  needed for radiocarbon dating with state of the art AMS. Hence, data for all PLFA  $C_{i+ai15:0}$  values have to be interpreted with caution. Additionally, due to only very small recoveries of  $C_{i+ai15:0}$  and  $C_{18:2+18:1}$  at 86-89 cm after purification, radiocarbon analysis was not possible for these purified compounds.

In all sample depths,  $C_{16:1}$  FAME had a lower  $F^{14}C$  than the co-occurring  $C_{16:0}$  at the same depth.  $C_{16:1}$  FAME range from  $F^{14}C$  of  $0.459 \pm 0.0115$  at 86-89 cm to  $0.760 \pm 0.0067$  at 0-3 cm. Similarly,  $F^{14}C$  of  $C_{16:0}$  FAME increase from  $0.606 \pm 0.0146$  at 86-89 cm to  $0.893 \pm 0.0085$  at 0-3 cm. In the topmost 15 cm  $C_{18:2+18:1}$   $F^{14}C$ -values remained the most constant of any dated FAME ranging between  $0.854 \pm 0.0102$  and  $0.878 \pm 0.0134$ , however, they decreased to  $0.699 \pm 0.0096$  at 133-136 cm.  $C_{i+ai15:0}$  FAME in the PLFA fraction showed the most diverse tendency in relation to the other FAMES at the respective depths. At 0-3 cm  $C_{i+ai15:0}$  had the youngest  $F^{14}C$ , coming close to the second youngest of  $C_{18:2+18:1}$  at 5-8 cm, being the oldest FAME fraction at 10-13 cm, and retuning back to being the second youngest to  $C_{18:2+18:1}$  at 133-136 cm. However, it has to be emphasized once more that the margin of error for

PLFA  $C_{i+ai15:0}$  is very high. Nevertheless, all  $F^{14}C$  values of the dated FAMES remained at values significantly below local marine reservoir ages of displayed by GLFA  $C_{14:0}$ .

FAME	depth [cm]	F14C	$\sigma F^{14}C$	fossil
<b>GLFA C14:0-FAME</b>	0-3	0.959	0.0098	0%
<b>GLFA C15:0 (i+ai)-FAME</b>	0-3	0.833	0.0093	13%
	5-8	0.781	0.0085	19%
	10-13	0.771	0.0097	20%
	86-89	0.556	0.0255	42%
	133-136	0.611	0.0065	36%
<b>GLFA C16:1-FAME</b>	0-3	0.770	0.0061	20%
	5-8	0.676	0.0071	30%
	10-13	0.701	0.0069	27%
	86-89	0.468	0.0048	51%
	133-136	0.540	0.0048	44%
<b>GLFA C16:0-FAME</b>	0-3	0.861	0.0068	10%
	5-8	0.780	0.0070	19%
	10-13	0.790	0.0066	18%
	86-89	0.565	0.0054	41%
	133-136	0.632	0.0057	35%
<b>GLFA C18:2+C18:1-FAME</b>	0-3	0.903	0.0067	6%
	5-8	0.923	0.0079	4%
	10-13	0.877	0.0074	9%
	86-89	0.698	0.0065	27%
	133-136	0.748	0.0061	22%
<b>GLFA C26:0 + 28:0 + 30:0-FAME</b>	5-8	0.625	0.0126	35%
	133-136	0.368	0.0083	62%
FAME	depth [cm]	F14C	$\sigma F^{14}C$	fossil
<b>PLFA C15:0 (i+ai)-FAME</b>	0-3	0.926	0.0142	4%
	5-8	0.869	0.0243	9%
	10-13	0.638	0.0199	34%
	133-136	0.645	0.0253	33%
<b>PLFA C16:1-FAME</b>	0-3	0.760	0.0067	21%
	5-8	0.693	0.0065	28%
	10-13	0.650	0.0066	32%
	86-89	0.459	0.0115	52%
	133-136	0.521	0.0066	46%
<b>PLFA C16:0-FAME</b>	0-3	0.893	0.0085	7%
	5-8	0.805	0.0081	16%
	10-13	0.803	0.0104	16%
	86-89	0.606	0.0146	37%
	133-136	0.611	0.0065	36%
<b>PLFA C18:2+18:1-FAME</b>	0-3	0.869	0.0079	9%
	5-8	0.878	0.0134	8%
	10-13	0.854	0.0102	11%
	133-136	0.669	0.0096	30%

Table 5: Radiocarbon signatures ( $F^{14}C$ ) of purified FAME of glyco- (GLFA) and polar-lipid (PLFA) fractions, uncertainties ( $\sigma F^{14}C$ ), and calculated amounts of ancient carbon used for biosynthesis of the FAME (fossil).

## 4. Discussion

### 4.1 Sources of Organic Matter

The deposition of OM in marine sediments is a key natural mechanism of carbon sequestration, within the global carbon cycle. Rates of deposition and sequestration, are highly dependent on the overall OM flux and the type of OM put into the sediment. This rate however, is strongly influenced by external factors. Especially in arctic regions, climatic changes are expected to dramatically alter sedimentary OM input. Hence, understanding these mechanisms will be crucial to predict future changes, due to global warming.

Within this section working hypothesis (1) is discussed, debating organic matter input from different sources and their relation to climatic changes during the time from 1961 to 2014 in Brepollen, Hornsund Fjord, Svalbard. Despite its recent deposition, the bulk OM showed extremely high

radiocarbon ages ranging from  $17,327 \pm 48$  years B.P. at the core top, to ages of constantly over 25,000 years B.P. in the lower parts of the core, indicating the deposition of primarily old OM.

SAR are of major importance for the input and preservation of OM to the sediment (Koziorowska et al., 2018). Based on the observed differences in SARs, in the following sections the sediment core is divided into three parts (Figure 11). The distance to the glacial front (Błaszczuk et al., 2013) during these phases can be reconstructed according to the depositional age of the OM determined by Szczuciński's age model. The section below 53.5 cm was deposited before 1980, with glacial fronts being within 1 to 4 km of the core location. Consequently, SAR were fairly high ranging from 3.0 to over  $6.0 \text{ cm yr}^{-1}$ , with an increasing trend downcore towards the most proximal position of the glacial fronts. Above 19 cm the sediment was deposited after 1990, with a reduced SAR of  $1.2 \text{ cm yr}^{-1}$  and below, with a decreasing trend towards the core top. Distances to the tidewater glaciers increased over time, from about 4 to 6 km in 1990 up to 10 km for the most distal position of the glacial front in 2010 (latest data). In the transitional section from 19 to 53.5 cm, ranging from 1990 to 1980 respectively, SAR were stable at  $3.0 \text{ cm yr}^{-1}$  and glacial fronts were located about 4 to 6 km from the core location.

### 4.1.1 Terrestrial Organic Matter

Vascular plants are the primary precursor of terrestrial OM (Burdige, 2005). Within the framework of this thesis, organic carbon from petrogenic sources is distinguished from the terrestrial fraction and is defined as an individual fraction, as the OM of both pools differs substantially. In this section, the sedimentary input of recently synthesized terrestrial OM is discussed based on GDGTs and FAs distributions using BIT index and  $\text{TAR}_{\text{FA}}$ , respectively. Both FAs and GDGTs have been reported to be relatively sensitive to degradation (Mollenhauer and Eglinton, 2007; Shah et al., 2008). Hence, the influence of petrogenic OM onto both indices is expected to be minimal.

The BIT index showed values significantly below 0.12. In the original study from Hopmans et al. (2004) open ocean sediments were found to have BIT index values as high as 0.22 but generally below 0.10 (Figure 11). Despite the proximity of the core location to the shoreline, BIT values in this study are similar to open ocean sediments, described by Hopmans et al. (2004), indicating the very low or negligible contribution of fresh terrestrial OM. Furthermore,  $\text{TAR}_{\text{FA}}$  values consistently below 0.17, indicate very low terrestrial contributions throughout the core. However, due to degradational effects of the short-chained FAs and anthropogenic input of long-chained FAs,  $\text{TAR}_{\text{FA}}$  values may even be overestimated. Mollenhauer and Eglinton (2007) have shown that degradation occurs at an elevated speed in short-chained FAs compared to long-chained FAs. Additionally, Stubbins et al. (2012) found

long-chained FA were derived from anthropogenic aerosols in glacial surface snow. In combination, these factors may lead to an overestimation of the  $TAR_{FA}$  values, and therefore, an overestimation of the significance of the terrestrial fraction. Furthermore, the satellite images and the reconstructed positions of the glacial fronts by Błaszczuk et al. (2013) reveal no land exposure suitable for soil or terrestrial plant development.

On the contrary, some authors (Bardgett et al., 2007; Bhatia et al., 2010; Hood et al., 2009) reported peat or forest areas, which developed in former Holocene warm periods, to be overrun by current glaciers, providing some potential for terrestrial input. Additionally, terrigenous OM material transported by currents from the outer parts of the fjord into the Brepollen has to be considered. Hornsund Ford is, due to its substantial size and geographical location, prone to inward flowing currents on its southern shore, caused by the Coriolis force (Pawłowska et al., 2017). Hence, terrigenous OM, derived from lesser glaciated regions in the outer Hornsund Fjord, may deposit in the Brepollen Bay. However, the shallow sill dividing the Brepollen bay from the central basin (Forwick, 2019, unpublished data, personal communication, UiT) and the significant meltwater discharge (Wezslawski et al., 1991) flowing out of the Brepollen bay, in combination with prevailing katabatic winds (Cottier et al., 2010) are expected to minimize the input from Coriolis currents by surface waters. On the contrary, meltwater plumes at the glacial front are expected to cause a suction effect, transporting intermediate- and/or bottom-water towards the glacier (Lydersen et al., 2014), potentially allowing terrigenous OM to be transported towards Brepollen bay. Yet again, the very shallow sill separating the bay from the main basin, is expected to limit the inflow of those water masses severely (Forwick, 2019, unpublished data, personal communication, UiT).

Nevertheless, the detected terrestrial biomarker contents are very low, especially in comparison with the very high TOC values, derived mainly from petrogenic OM (compare below) being delivered by glaciers from subglacial rocks. Therefore, as hypothesized terrestrial OM can be regarded as a negligible part of the sedimentary OM pool.

### **4.1.2 Relative Contributions of Marine and Petrogenic Organic Matter**

Organic matter input to the sediment at the core site was fairly high and stable over time, based on the TOC content of roughly 1.8 % throughout the entire depth of the sediment core. However, considering the dramatic slow-down in SAR towards the core top (above 19 cm, after 1990), an overall decrease in  $MAR_{TOC}$  was observed. Simultaneous to the decrease in SAR and the increasing distance to the glacial fronts in the top 19 cm, a distinctive decrease in TOC/TN and  $TAR_{FA}$  was observed, associated

with a synchronous increase of  $CPI_{HC}$  and  $F^{14}C$  (Figure 11). However,  $\delta^{13}C$  showed extremely stable values between -24.9 and -24.5, with no associated zonation. Indicating either (1) a relative increase in marine OM input to the sediment, (2) degradational processes, or (3) both.

Considering these three possibilities, the sum of FA/HC indicates an increase of FAs versus n-alkanes over time and, therefore, supports (1) an increased input of marine OM into the sediment. Short-chained FAs dominated both the decreasing  $TAR_{FA}$  and the increasing FA/HC towards the core top. However, both indices are likely to be influenced by degradational processes of the short-chained FAs (Mollenhauer and Eglinton, 2007). A combination of both higher marine OM input to the sediment and degradation is displayed by the biomarker distribution.

If it is assumed that terrestrial OM can be excluded from the OM pool (as argued above), the remaining fractions of marine and petrogenic OM consequently make up a two-endmember model. As the petrogenic OM is expected to be derived from Tertiary coal (compare below), it can be considered as radiocarbon free, leading to a  $F^{14}C$  endmember-value of 0.00. On the contrary, the marine  $F^{14}C$  endmember-value is defined by the youngest FA of the polar fraction GLFA  $C_{14:0}$  purified from the core top (0-3 cm), as an indicator for recent primary production ( $F^{14}C = 0.833 \pm 0.0093$ ; Table 5). The lower part of the core (sedimented before 1980, below 53.5 cm), with SAR of above  $3.0 \text{ cm yr}^{-1}$  has a relative marine contribution of the OM of 3 % to 5 % (Figure 11). Whereas, the top part (sedimented after 1990, above 19cm) with low SAR ( $< 3.0 \text{ cm yr}^{-1}$ ), relative marine contributions increase from 6 % to 12 % Consequently, the marine fraction of the TOC rose from 4 % to 14 %, indicating a strong shift towards more marine conditions at the core site with an ongoing retreat of the tidewater glaciers.

The  $C_{31S/R}$  homohopane configurations can be taken as an indicator for recently synthesized versus petrogenic organic matter (Meyer et al., 2019). The  $f\beta\beta$  index values in sediment core HE14-897-MF-GC showed constant values below 0.09, meaning that petrogenic organic matter input expressed by  $f\beta\beta$  is generally very high, being at least 90% throughout the core. This indicates a similar ratio of marine to petrogenic OM as TOC  $F^{14}C$  data in the lower parts of the core at 53.5 cm and below, ranging from 2.5 % to 10 % and 97.5 % to 90 % respectively (Figure 11). Petrogenic carbon input is clearly dominating the sedimentary system. The above described end-member model even suggests higher values than the previous study of Kozirowska et al. (2016). They estimated the marine fraction to be between 18 % to 20 % in surface sediments in Brepollen on the basis of a carbon-nitrogen two-endmember model.

The distinctive shift from high to medium and low sedimentation rates is also evident in the  $f\beta\beta$ -values. Within the deeper region of high SAR,  $f\beta\beta$ -values ranged from 0.024 to 0.1, whereas slower SARs above 53.5 cm were associated with distinctively lower  $f\beta\beta$ -values, ranging from only 0.005 to 0.034. Even though concentrations of the compound  $C_{31}\beta\beta R$  were close to the detection limit, the uniform shift of  $f\beta\beta$  with SAR was interpreted as a real signal rather than an analytical error. Nevertheless, the shift of  $f\beta\beta$  to lower values at the core top is counter indicative to the rest of the obtained data, as it would imply an increasing input of petrogenic organic matter. Considering the lower SAR, a longer oxygen exposure of the compounds maybe a possible explanation for the shift. Alternatively, the retreating glaciers may cause a change in sediment origin. Lewińska-Preis et al. (2009) described an evolution of the coal seams within the Firkanten Formation related to their position in the central Tertiary basin. Strong maturity gaps and associated variances in geochemical parameters have been reported within the Firkanten Formation, being stratigraphically only 40 m apart (Marshall et al., 2015). It follows that with fast retreating glaciers (Błaszczuk et al., 2013) some sediment layers may not be contributing to the marine input any longer, resulting in a change of the  $f\beta\beta$ -values. The data obtained in this thesis, however, do not unambiguously exclude one or the other scenario.

### 4.1.3 Petrogenic Organic Matter

The homologous *n*-alkane distributions showed a striking but continuous pattern throughout the entirety of the sediment core. Due to enzymatic decarboxylation of fatty acids during biosynthesis, a general dominance of odd- over even-numbered *n*-alkanes is generally observed in modern sediments (Killops and Killops, 2013). However, this trend was not observed in sediment core HH14-897-MF-GC. CPI values were consistently close to 1 indicating a high maturity of the sediment organic matter (Peters et al., 2005). Furthermore,  $C_{31S/R}$ -values were uniformly close to 0.6 (Figure 11) which indicated a consistent and strong maturity of the organic matter supplied to the fjord sediment (Seifert and Moldowan, 1980). Considering that the sediments retrieved in the core were deposited between 1960 and 2014, this pronounced maturity of the sediment cannot be achieved by diagenesis or catagenesis. The most likely source of mature OM is the sedimentary load of the glacial catchment originating from Tertiary coal seams of the adjacent and underlying Firkanten Formation (Dallmann et al., 2015; Marshall et al., 2015). However, when compared with the study from Ćmiel and Fabiańska (2004), the *n*-alkane chromatograms, CPI values,  $Pr/n-C18$  values, and  $C_{31S/R}$ -values rather resemble analyzed coal from the Hornsundneset Formation located to the south in the Sorkapp Land region. On the contrary, no biogeochemical studies regarding the coal seams of the Firkanten Formation in the area of the Brepollen catchment have been done to the author's knowledge, as the majority of the area is covered

by glaciers (Dallmann et al., 2015). Geochemical parameters could therefore be different to those at various locations throughout Svalbard (Ćmiel and Fabiańska, 2004; Kim et al., 2011; Lewińska-Preis et al., 2009; Marshall et al., 2015), especially as the biogeochemistry of these coal seams has been reported to change on small scales (Marshall et al., 2015).

### 4.1.4 Marine Organic Mater

Due to enhanced FA degradation and transformation during digenesis (Ho and Meyers, 1994) and especially catagenesis (Killops and Killops, 2013), the obtained FAME distributions were interpreted as more recently formed biomarkers in comparison to *n*-alkane distributions. This assumption has been taken into consideration under the implication of the high maturity of the natural hydrocarbon fraction, illustrated by the abundance patterns of *n*-alkanes and homohopanes (compare above). This is also supported by higher  $CPI_{FA}$ -values compared to  $CPI_{HC}$ -values, which ranged from between 6.96 and 12.70 (Figure 11), indicating low maturity and therefore more recent synthesis.

In marine sediments, fatty acids typically show a bimodal distribution pattern with two maxima at  $C_{16:0}$  and  $C_{26:0}$  (Uchida et al., 2001). The saturated, long-chained fatty acids ( $C_{26:0}$ ,  $C_{28:0}$ ,  $C_{30:0}$ ) are indicative of higher vascular plants (Eglinton and Hamilton, 1967). Their abundances throughout core HE14-897-MF-GC were very low and often close to the detection limit. On the contrary, FAME distributions showed a strong dominance of even-numbered, short-chained saturated fatty acids ( $C_{14:0}$ ,  $C_{16:0}$ ,  $C_{18:0}$ ; Figure 13), which are ubiquitous in all plants, but dominant in algae (Cranwell et al., 1987). Consequently,  $TAR_{FA}$ -values were very low, too (compare above). Furthermore, levels of FAME  $C_{20:4}$ ,  $C_{20:5}$ , and  $C_{22:6}$  were uniformly elevated. These polyunsaturated fatty acids are indicative of marine Phyto- and Zooplankton as well (Bianchi and Canuel, 2011).

The very high abundance of FAME  $C_{16:1}$  (second most abundant) was used as a diagnostic marker for bacteria (Elvert et al., 2003; Moss and Lambert-Fair, 1989). Even though FAME  $C_{16:1}$  has also been reported to be produced by diatoms (Dalsgaard et al., 2003; Dunstan et al., 1993), FAME  $C_{16:1}$  is expected to have a primarily bacterial origin as their concentrations in the IPL fraction (viable microbiota) continue to be equally high downcore. If FAME  $C_{16:1}$  would derive from diatoms, their concentrations in the IPL fraction would decrease downcore as diatom based IPLs would have already disintegrated with increasing depth and age. However, this was not the case. On the contrary, Petsch et al. (2001) reported that microbial communities can use ancient carbon as a substrate for their biosynthesis. As the obtained biomarkers suggest that the input of ancient organic carbon is dominating, the organic matter input to the sediment and that the local microbial communities are

similarly able to utilize ancient carbon (see below), I suggest that the high fraction of FAME C<sub>16:1</sub> is primarily caused by OM degrading bacterial communities in the sediment rather than by marine primary production.

### 4.1.5 Controls on relative abundances of petrogenic and marine OM

Controls for the relative increase of petrogenic to marine OM were hypothesized to be primarily caused by temperature increase, due to climate change. The period after 1990 was expected to show a strong increase in meltwater derived material and organic matter (Change, 2007). Over the 53 years covered by the core HH14-897-MF-GC, summer and winter season temperatures were combined using monthly average temperatures from June to September and November to February respectively (eKlima data-base). As the winter seasons use data from two years, the consecutive year was used in the following, e.g. winter season 1959/1960 is displayed as “winter 1960” (Figure 16). However, the obtained biomarker abundances showed a completely opposite trend of marine OM rising relative to petrogenic organic matter, corresponding to both summer and winter temperatures. Furthermore, by comparing sedimentary TOC-values (based on the age model) with seasonal temperature changes between the years of 1960 and 2014 (recorded at Svalbard Airport, Longyearbyen), no direct correlation between seasonal temperature shifts and the OM input was observed. However, within the uncertainty of the age model small scale conformities between winter temperature and TAR<sub>FA</sub> were found. Winter sea surface temperatures are a major control on sea-ice formation (Muckenhuber et al., 2016), which in turn is strongly influencing light penetration into the photic zone and consequently exerts a strong control on primary production of phytoplankton (Mikkelsen et al., 2008). On the contrary, Muckenhuber et al. (2016) further stated that sea-ice coverage is primarily controlled by microclimatic conditions. They further reported significant differences between Kongsfjorden and Honsund Fjord, due to a strong influence of arctic waters from the Sørkapp Current. This demonstrates that comparing Honsund Fjord biomarker data to Longyearbyen Airport temperature archives may be too distant. Unfortunately, no temperature archive with sufficient data coverage from a location nearer to Honsund was accessible. To mitigate this issue, lipid-based paleo sea surface temperature reconstructions were attempted. However, the very low concentrations of the iso-crenarchaeol and its peak area coeluting with the very high quantities of regular crenarchaeol restrained the reconstruction of paleo sea surface temperatures based on GDGTs (Schouten et al., 2013). Paleo sea surface temperatures were calculated using the recently used indices for cold climates, i.e., TEX<sub>86</sub><sup>L</sup>, RI-OH', and indices based on OH-GDGT (Park et al., 2019; Wei et al., 2019), without archiving any plausible results in comparison with measured sea surface temperature reported in the literature.

Nonetheless, a long-term trend was visible since the 1990s (above 19 cm), indicating an increase in the marine OM distribution. Simultaneously, TOC values decreased slightly since the 1980s. The calculated total organic-carbon accumulation rates for this core differed strongly from about  $100 \text{ g C m}^{-2} \text{ yr}^{-1}$  at the core top to more than  $1400 \text{ g C m}^{-2} \text{ yr}^{-1}$  downcore (Figure 11), and was about 2 to 28 times as high as the average organic-carbon accumulation rate in Svalbard fjords, reported by Smith et al. (2015). Furthermore, they displayed very well the overall dynamic changes on OM distribution to the sediment over the course of the 53 years covered by the sediment record.

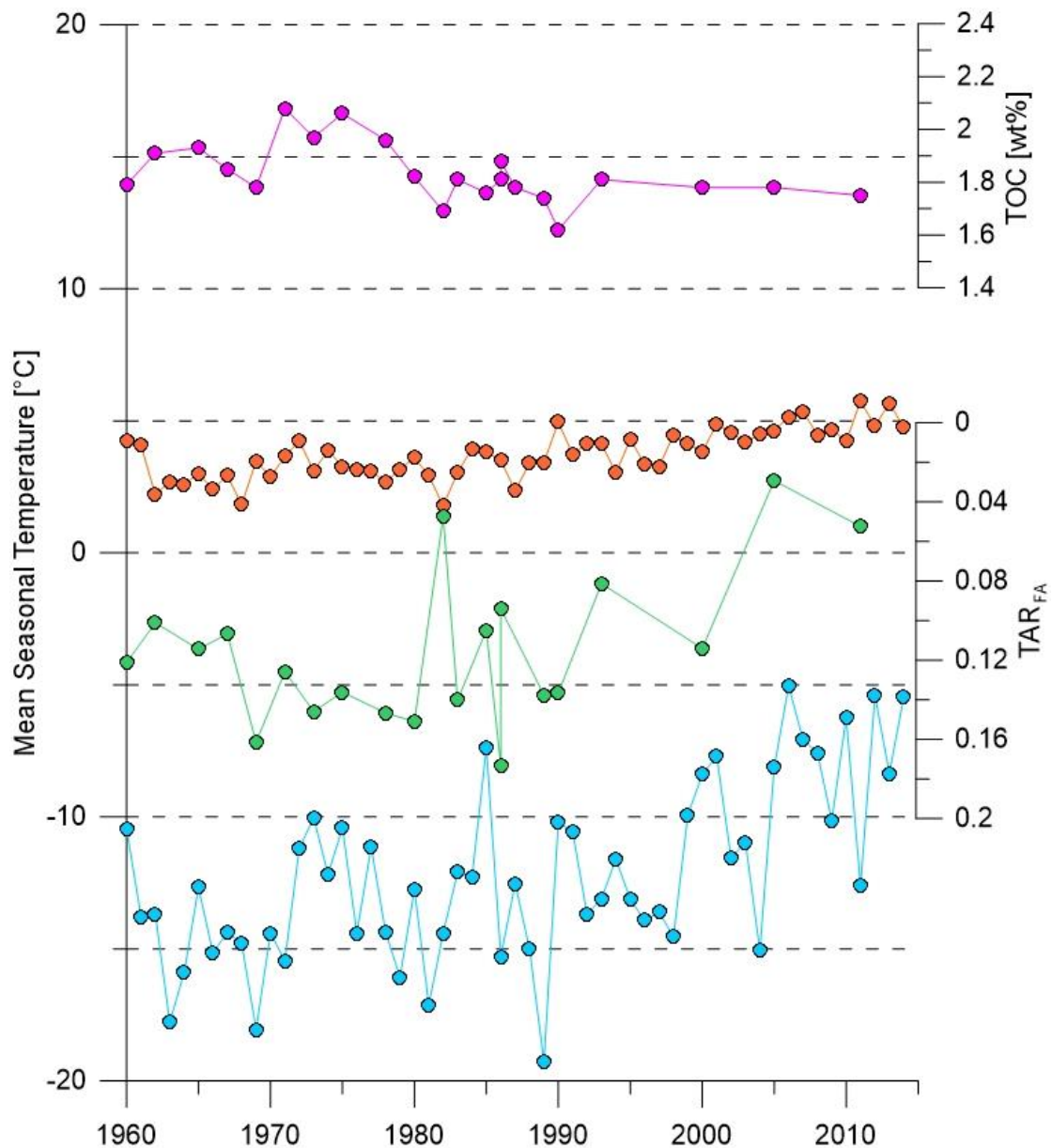


Figure 16: Average seasonal summer (orange) and winter (blue) temperature measured at Svalbard Airport of the years 1960 to 2014, in comparison with TOC (pink) and  $TAR_{FA}$  (green) at the dated time periods according to the age model.

Simultaneous to this decrease of SAR and the TOC content of the deposited sediment, the performed isotope mass balance calculation of the bulk OM (Figure 11) indicated a consistent increase in the marine fraction of the TOC is observed, increasing from about 4 % of the TOC before 1980 up to about 12 % at the core top in 2014. This trend was most likely due to the fast retreat of the glaciers and therefore the increasing distance of the core location to the glacial front (Błaszczuk et al., 2013). The petrogenic OM input decreased, as its majority was deposited close to the glacial fronts (Syvitski, 1989; Szczuciński and Zajązkowski, 2013). Consequently, an even stronger increase of the marine fraction towards a more distal setting of the core would be expected, with sediment supply being more than an order of magnitude lower in the topmost 19 cm in comparison with SAR below. Using the  $F^{14}C$  isotope mass balance model, constant marine primary production rates can be assumed below 53.5 cm of about 4 % of the TOC. Assuming marine OM input rates from the water column remain constant, the drop of SAR in the top most 19 cm by an order of magnitude, would lead to an increase of the marine fraction of the TOC in the sediment to roughly 40 %. However, only a relative increase of about 6 % to 8 % of the marine fraction is observed in the top most 19 cm. A possible explanation is that tidewater glaciers are associated with meltwater plumes, which trap plankton close to the glacial fronts from more distal parts of the fjord. Due to the strong suction of the plume and extremely steep salinity gradients around it, a “planktonic death trap” is created (Lydersen et al., 2014), presumably leading to increased deposition of young marine OM close to the glacial fronts. This correlates with overall lower deposition rates of marine OM towards the core top. Associated with this hypothesis, documented scavenging of OM by mineral particles (Hedges et al., 2001; Hemingway et al., 2019) has to be considered. This causes an increased deposition of OM close to the glacial fronts with increased sediment load (Szczuciński and Zajązkowski, 2013). Biomarker concentrations indicate higher marine OM depositional rates at the glacial front in comparison to more distal settings suggesting that the location of the tidewater glacier (Figure 17) front is the strongest control on carbon burial rates in the local system.

These environmental alterations are associated with climate change induced temperature increases, however, temperature is not the only controlling factor. Other parameters, like sea-ice cover, precipitation, prevailing wind and oceanic currents, or nutrient input are likely to play essential roles in this system (Lydersen et al., 2014). These climate factors have a profound impact on the OM

deposited in Hornsund Fjord, although the changes are expected to have a greater influence on the spatial distribution of OM rather than the quality of OM deposited overall. As in this study, only one non-steady state core location was investigated, a full assessment of the input of the total Brepollen Bay is not possible. However, with increasingly ice-free conditions due to retreating tidewater glaciers and the formation of less sea-ice in the winter, an enhanced area is likely to sequester recently produced marine organic matter. Tidewater glacier fronts are expected to retreat further in the coming decades and will eventually reach adjacent shore lines (Błaszczuk et al., 2013; Change, 2007), diminishing freshwater plumes (Lydersen et al., 2014) and altering meltwater based sediment load input (Szczuciński and Zajączkowski, 2013), while still introducing pre-aged, potentially labile OM to downstream aquatic environments (Hood et al., 2015). These findings suggest that with ongoing climate change, the strong carbon burial capacity of fjord systems (Smith et al., 2015) may substantially decrease in the future.

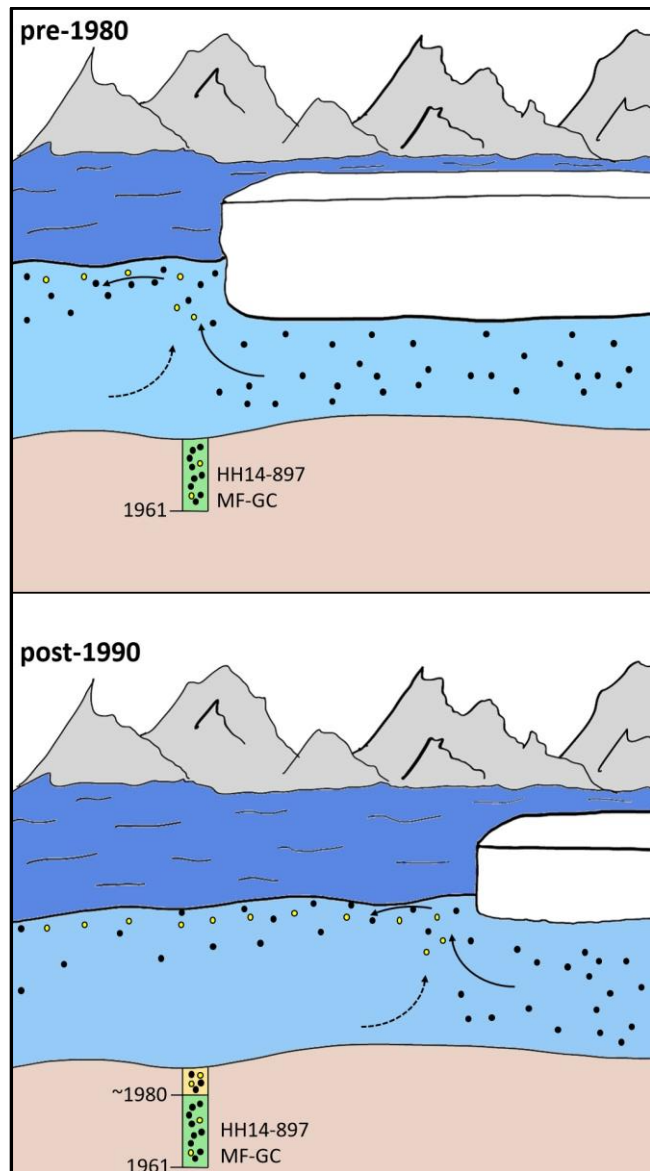


Figure 17: Scheme of sedimentary setting of core HH14-897-MF-GC, due to its proximity to the glacial front (white). Comparing proximal setting of pre-1980 to distal setting post-1990. Sub glacial streams transport low-density meltwaters (solid black arrows) with high suspension load of petrogenic OM (black dots) to the glacial fronts where they rise up through the water column causing suction and drawing bottom waters of the fjord in (scattered black arrows). At the sea-surface the low-density meltwaters flow outwards to the fjord mouth. In the surface waters marine OM (yellow dots) production is dominant as high particle load limits light penetration to deeper water masses. Due to the suction of the meltwater plume and the strong salinity gradient high planktonic mortality is expected to appear close to the glacial front, leading to higher marine OM detritus.

#### 4.1.6 Diagenetic impact on OM composition

Next to the control of the OM due to sedimentary input, degradational processes are important to consider, as remineralization prevents organic carbon from being sequestered. Remineralization processes are primarily governed by microbial communities, and strongly controlled by the availability of terminal electron acceptors for the oxidation of organic matter. Due to different energy yields of the individual electron acceptors and their diffusive replenishment from the sediment surface, a geochemical zonation in the sediments is established (Burdige, 2007), leading to higher rates of OM decomposition at the sediment-water interface in comparison to deeper sediments (Arndt et al., 2013). As diffusive processes are very slow, these high sedimentation rates counter the replenishment of terminal electron acceptors and nutrients, limiting the activity of microbial communities (Musslewhite et al., 2003) and therefore enhancing OM preservation in sediments (Müller and Suess, 1979). Unfortunately, no data are available for the geochemical zonation of the core sediment, however, with SAR being  $> 3.0 \text{ cm yr}^{-1}$  below 40 cm, degradational processes are expected to be minimal in the lower region but have to be considered above 40 cm as oxygen exposure is fairly limited (Hartnett et al., 1998).

Additionally, the age of the OM plays an important role as old OM is widely seen as being more recalcitrant, due to the exposure to previous remineralization cycles (Arndt et al., 2013) and potentially to diagenesis and catagenesis. Comparing  $F^{14}C$  from the pre-1980 section of the core to the post-1980, an increase of modern “young” OM was observed. This also gives an indication of the increasing “quality” of the OM and the associated increasing potential of the microbial communities to utilize the OM present in the sediment.

The biomarker indices of  $TAR_{FA}$ , TOC/TN, FA/HC, and  $F^{14}C$  of the bulk OM (Figure 11) all show distinctive patterns of parallel shifts towards the core top, resembling typical degradational profiles. With a strong decrease of SAR since the early 1990s (above 19 cm), the sediment and the incorporated OM have undergone increased exposure times to terminal electron acceptors, causing increased degradation of OM in the sediment (Arndt et al., 2013; Hartnett et al., 1998). However, the increased degradational effects can be observed as deep as the sample at 43.5 cm, even though SAR in this depth were still at an intermediate to high level ( $>3.0 \text{ cm yr}^{-1}$ ). As the younger sediment layers are thinner, increased diffusion of terminal electron acceptors like oxygen, nitrate, manganese (IV), iron (III), and sulfate into the sediment below is likely. Therefore, enhanced rates of remineralization are expected between

19 and 43.5 cm, however not in the top most 19 cm. Below 50 cm biomarker indices did not display enhanced ongoing or former degradation rates.

As the biomarker indices can be influenced by sedimentary input fluxes, this control was assessed by comparing the same indices of a more distal core in the Hornsund Fjord (Mollenhauer 2019, unpublished data), showing similar shifts in shallow core depth. However, based on the age models of the cores, these shifts happened at very different times, with changes occurring in the distal core after the proximal core. If the change would have occurred due to the sedimentary input controlled by the glacial front position, the changes in the more distal setting would have to occur before the proximal setting. Since this is not the case, diagenetic controls on the OM content in the sediment can be assumed to be of substantial importance, especially as IPL data suggest highly active microbial communities within the sediment.

However, the increasing remineralization towards the core top may not just result from an increase in available terminal electron acceptors but may also be due to a relative increase in labile OM, as low oxygen concentrations limit microbial processes but a lack of labile OM in aquatic systems limits bacterial heterotrophy even with high oxygen levels (Kristensen et al., 2000). A combination of the aforementioned factors is likely controlling the intensity of early diagenesis.

### **4.1.7 In-situ microbial community**

In order to determine microbial community composition in the sediment, the IPL inventories of the PL fractions were assessed at the same depths as CSRD was performed. Additionally, average chain length and number of double bonds of the most abundant IPL-FAs were determined. The IPL inventory indicates viable microbiota within the sediment, as PL imported from external sources into the sediment are expected to decay within days to weeks after cell lysis (Harvey et al., 1986; White et al., 1979). This, in combination with FAME C<sub>16:1</sub> as the second highest detected FA throughout the core, indicates that recently produced OM from bacterial origin is very high. As depth increases and input of fresh marine OM decreases, in-situ produced lipids are expected to constitute a substantial part of the lipid biomarker inventory.

Both PC and BL are prevailing within phototrophic organisms, and have been reported to be present in near shore subsurface environments, due to hydraulic transport through sandy, tidal sediment from the water column (Seidel et al., 2012). However, grain sizes being in clay to silt range and the coring location being at a water depth 140 m below sea-level, this input mechanism of PC and BL into the

subsurface is negligible. Nevertheless, PC are making up between 27 % to 33 % of bacterial IPLs of the PL fraction and hence, are the dominating IPL structure. The previous study of Schubotz et al. (2009) reported only minor quantities of PC in subsurface sediments. However, PC have been reported in some sulfate reducers (Rütters et al., 2001) and are also present in other bacteria (Sohlenkamp et al., 2003). Similarly, BL have been speculated to be derived from sulfate-reducers in marine sediments or related bacteria (Rossel et al., 2011; Schubotz et al., 2011). With TOC values being highly elevated, a quick transition to sulfate as an electron donor can be expected as more energy yielding electron donors are expected to be limited to the surface sediment (Arndt et al., 2013). Correspondingly, PC values are the lowest in the topmost sample. However, PC may also originate from other organisms and not be exclusively produced by sulfate reducing bacteria. Furthermore, the rapid PL degradation after cell death (Harvey et al., 1986; White et al., 1979) suggests a heterotrophic, in-situ origin.

The membrane lipids PME and PE represent interchangeably the second and third most abundant class of IPLs in the PL fraction, with similar concentration levels. Combined they make up between 41 % to 51 % of the PL quantities. Both PME and PE have been found in methanotrophic bacteria (Fang et al., 2000), which is a likely scenario as TOC values were very high and conditions are expected to be anoxic. PE is a canonical IPL in sulfate-reducing bacteria, which are a likely source in these sediments. Furthermore, both PE and PME were suggested to be present in fermenting bacteria and heterotrophic bacteria involved in hydrocarbon degradation (Schubotz et al., 2011). The study of Schubotz et al. (2011) further suggested bacterial precursor organisms of PME and PE to use asphalt derived hydrocarbons as substrate. As the vast majority of the OM in the sediments analyzed for this study, is expected to be of petrogenic origin with very high thermal maturity, similar bacterial communities are potentially active in the local sediment utilizing remnant OM. Similar to PE, PG is one of the major membrane-forming lipids in sulfate reducing bacteria (Rütters et al., 2001; Sturt et al., 2004).

Both DPG and lyso-DPG were only minor lipids in the PL fractions (<5 % of total IPL). DPG have been reported to be dominant in energy limited environments (Seidel et al., 2012) under the expense of PE and PG (Mukamolova et al., 1995). High values of PG and PE accompanied with high TOC values on the contrary, suggest low limitations in this regard and would limit the necessity of bacteria to assimilate DPG lipids. This observation further supports favorable conditions for heterotrophic bacteria in these sediments. It must be stated that similar amounts of DPG and lyso-DPGs were also detected in the GL fraction, so their values are underrepresented in the PL fraction. Nevertheless, even combined they comprise only a minor fraction of the total PL inventory.

Taking into account the different IPL classes, the input of high amounts of petrogenic carbon to the sediment, resulting in high TOC values, the strong homogeneity throughout the core, and most likely strongly anoxic conditions occurring directly below the sediment surface, a dominance of sulfate reducing bacteria is expected. Potentially associated with fermenting communities. A very striking feature is the strong similarity between the core top sample and the deeper samples. IPLs of phototrophic organisms would be expected to have elevated levels at the core-top. However, during sediment collection from the gravity-core, the top most 2 mm of the core-top sample were taken off, in order to prevent  $^{14}\text{C}$  contamination from the synthetic plastic liner and cap. This removal may have caused many of the phototrophic IPLs to be removed from the sample, due to the fact that they would be accumulated only at the core top, as bioturbation can be expected to be marginal based on the X-ray scans. IPLs and consequently the derived FA used for the CSRD are therefore expected to be of OM degrading bacterial origin.

IPL group specific average chain-length and average number of double bonds of the associated FAs (Figure 15) showed generally a similar trend of consistency by the microbial community. All IPL groups but PE, have an average chain-length shift of less than a  $\text{C}_2$  chain and shifts in the number of double bonds of 1 or less. These shifts are mainly due to changes in the contribution of  $\text{C}_{18:1}$  and  $\text{C}_{16:0}$  (data not shown). By comparing the more pronounced shift in PE, this is primarily associated with a loss of polyunsaturated FAs like  $\text{C}_{20:4}$  and  $\text{C}_{20:5}$  and an increase in the relative abundance of  $\text{C}_{15:0}$ ,  $\text{C}_{15:1}$ ,  $\text{C}_{16:0}$ , and  $\text{C}_{16:1}$ . As odd-numbered, monounsaturated, and methyl-branched PLFAs are commonly of purely bacterial origin (Guckert et al., 1985; Ringelberg et al., 1997), average chain lengths and double bonds indicate further the dominance of bacteria in the PL fraction of the separated IPLs and further display the prevailing homogeneity in the sediment core.

### 4.2 Organic matter as microbial substrate

In recent decades, the question of whether or not microbial communities can utilize OM from ancient, remnant sources as a substrate for their metabolic pathways. To investigate this topic further, within this section working hypothesis (2) is discussed, whether local, sedimentary, microbial communities in Hornsund Fjord can utilize ancient OM of petrogenic origin or if they are limited to freshly produced modern marine substrates. Hence, CSRD was performed using  $^{14}\text{C}$  as an inverse tracer for modern and ancient substrates. Fatty acids of intact polar lipids were extracted, purified into single compound fractions, and subsequently dated.

### 4.2.1 Origin of dated fatty acids

Quality control was performed, to ensure fatty acids used for CSRD were derived from viable microbiota in the sediments, rather than being derived from free fatty acids of other precursor lipids. Therefore, IPL analysis was performed using HPLC-MS after (Wörmer et al., 2015). This approach allowed an assessment of the performed column chromatographic separation of IPLs into N-TLE, GL, and PL-fractions.

IPL analyses showed a good separation of the PL-fraction, with only very minor contamination of TAG in this fraction (data not shown) and minor detectable GL. TAG are mainly used as energy deposits within the cells (Kalscheuer et al., 2007) and are less prone to decay than GL and phospholipids (Akondi et al., 2017). Contamination from TAGs in PL-fraction is limited to FAMES  $C_{16:0}$ ,  $C_{18:1}$ , and  $C_{18:2}$ , which are presumably from marine primary production. Therefore, bacterial FA markers of FAME  $C_{15:0}$  i&ai and  $C_{16:1}$  show no contamination due to TAGs. Except for the core top, IPLs of the PL fraction from all of the other four sample depths should be exclusively derived from sedimentary bacteria, as algal IPLs are expected to be degraded within the surface layer. This rapid decay was reported to occur within days to weeks after cell death (Harvey et al., 1986; White et al., 1979) and is supported in our samples by the lack of typical phototrophic fatty acid side chain combinations observed in the PL (with the exception of PE in the uppermost sample). With SAR being as low as  $0.5 \text{ cm yr}^{-1}$  at the core top, even the topmost sample from 0-3 cm should be deposited long enough, that only a fraction of the IPLs in the analyzed sediment can be of phototrophic origin. Additionally, some glycolipid and aminolipids were found in the PL fraction. However, their side-chains were dominated by monounsaturated, odd-numbered, and methyl-branched FAs, which suggests they are of in-situ microbial origin. The dated FAs of the PL-fraction can be safely interpreted as purely in-situ bacterial origin.

While the PL fraction seems to represent an in-situ signal, the separation of IPLs in the GL fraction was not as successful: Before the experiment, the fate of free, unbound fatty acids during IPL column separation was determined using a  $C_{19:0}$ -MA standard on test columns using the described procedure. Recovery rates were close to 100% in the GL-fraction and below detection limit in the N-TLE and PL fraction. Achieved separation of the actual samples were verified by checking IPL splits for free fatty acids with GC-MS (data not shown). This showed that > 95 % of free fatty acids eluted into the GL-fraction and not as expected into the N-TLE fraction. IPL analysis showed that the GL fractions have substantial contamination by TAGs indicating that the GLFAs are composed of a mixed-signal from potentially modern to ancient free FAs, FAs from TAGs with an expected modern radiocarbon signal,

and in-situ produced FAs, initially bound to GLs, with radiocarbon signal of the in-situ communities. The resulting mixed-signal has to be therefore interpreted with cushions.

### 4.2.2 Carbon fixation

To assess the FA radiocarbon signatures of the viable bacterial community in the sediment, carbon sources for the metabolic pathways of the microbial community have to be discussed (Petsch et al., 2001). Within the local sediment, four possible carbon sources were identified: (I) seawater derived DIC, (II) carbonate derived carbon due to in-situ dissolution, (III) deposited OM via direct assimilation by heterotrophs, or (IV) deposited OM via carbon release due to remineralization and its subsequent assimilation of by heterotrophs.

Considering the radiocarbon depleted values of all dated FA but GLFA C<sub>14:0</sub> render (I) as singular source highly unlikely as estimated marine reservoir ages are too young. Furthermore, (II) dissolved carbonates have been excluded as a source as adjacent source rocks were of primarily siliciclastic origin (Dallmann et al., 2015), marine primary production was reported to be primarily performed by diatoms and flagellates (Piwosz et al., 2009) which produce siliciclastic rather than carbonate skeletons (Schrader, 1971), and bulk sample treatment with 6M HCl showed no carbonate degassing.

Sedimentary OM as the primary carbon source, agreed best with the detected FA radiocarbon values. The direct assimilation (III) by heterotrophic microbes would be the most straightforward assumption and is considered to be the most likely processes. However, heterotrophic bacteria have been reported to assimilate to some minor degree carbon from CO<sub>2</sub> through the citric acid cycle (Ljungdahl and Wood, 1969). Furthermore, Kellermann et al. (2012) have shown that at least some microbial communities are capable of autotrophy, or can switch to autotrophy under certain environmental conditions in sediments, e.g. presence of methane. These microbes primarily use the surrounding DIC for their biosynthesis and decompose OM only as an energy source. In the setting investigated in this thesis, the continuous remineralization of ancient OM as an energy source would cause an ongoing <sup>14</sup>C depletion of the residual DIC pool in the adjacent porewaters as the clayey grain size is likely to restrict concentration changes due to diffusive processes. The initial DIC pool during an early sedimentation state, can be expected to be at marine reservoir levels. Hence, the assimilation of sedimentary DIC into synthesized microbial lipids due to the citric acid cycle, may cause the F<sup>14</sup>C to underestimated the decomposed ancient OM.

### 4.2.3 Radiocarbon signature of fatty acids

As demonstrated in the previous section, the analyzed PLFAs were derived from IPLs of viable microbiota in the sediment. Within the subsurface, bacterial communities are often restricted to OM as singular energy source. The isotopic  $^{14}\text{C}$  signature of the utilized OM substrate is then passed on to the utilizing microbial communities (Petsch et al., 2001). Within the local sediments, these communities can either use (1) exclusively modern, freshly produced OM of marine origin, (2) exclusively ancient, petrogenic OM derived from Tertiary coal, supplied by glacial meltwaters, or (3) a mixture of both sources.  $F^{14}\text{C}$ -values for both endmembers had to be defined in order to determine which pathway the communities utilized. The petrogenic OM was defined as radiocarbon free, due to its initial deposition in the Tertiary. Therefore, the petrogenic endmember value was defined at  $F^{14}\text{C} = 0.0$ . The suggested marine reservoir age of  $380 \pm 30$  years by Mangerud et al. (2006) strongly resembles the GLFA  $\text{C}_{14:0}$  radiocarbon values of  $F^{14}\text{C} = 0.959 \pm 0.0098$  ( $334 \pm 67$  years) and was used as a modern endmember for the marine OM.

Except for GLFA  $\text{C}_{14:0}$  FAME, all analyzed FAs showed radiocarbon signatures below modern values (Figure 18) and therefore, reflect, to a certain degree, incorporation of the isotopic radiocarbon signal of the fossil petrogenic OM. FAs of both the GLFA and PLFA fractions show a clear indication of fossil OM being utilized for microbial biosynthesis. However, the degree to which fossil OM was assimilated into the FAs was highly variable, changing with FA configuration and sample depth.

Individual FA radiocarbon contents show variations both relative to GLFA and PLFA fractions as well as within the individual FAs themselves. However, trends of both fractions resemble one another, indicating similar mechanisms for the biosynthesis of GLs and PLs. From top to bottom a distinctive decrease in radiocarbon content was observed and therefore an increasing amount of fossil carbon was utilized with increasing depth.

These trends parallel the radiocarbon content of the bulk OM. However, radiocarbon levels are half to a full order of magnitude higher. Despite that, the CSRD of the sample depth of 86-89 cm showed the lowest radiocarbon contents. Unfortunately, no direct correlation between the bulk OM radiocarbon content at this depth was possible, due to limitations in sample material. Bulk OM radiocarbon dating was only performed at 83.5 cm and did not show a negative divergence in comparison to 133 cm. Due to very high SAR and strong seasonality of the sediment input (Szczeniński, 2019, unpublished data, personal communication, AMU) a distinctive difference between 83.5 and 86-89 cm is possible. Furthermore, this seasonality may cause the sedimentation of different quantities of substrates and

## Release and Remineralization of Ancient Carbon from Svalbard Glaciers

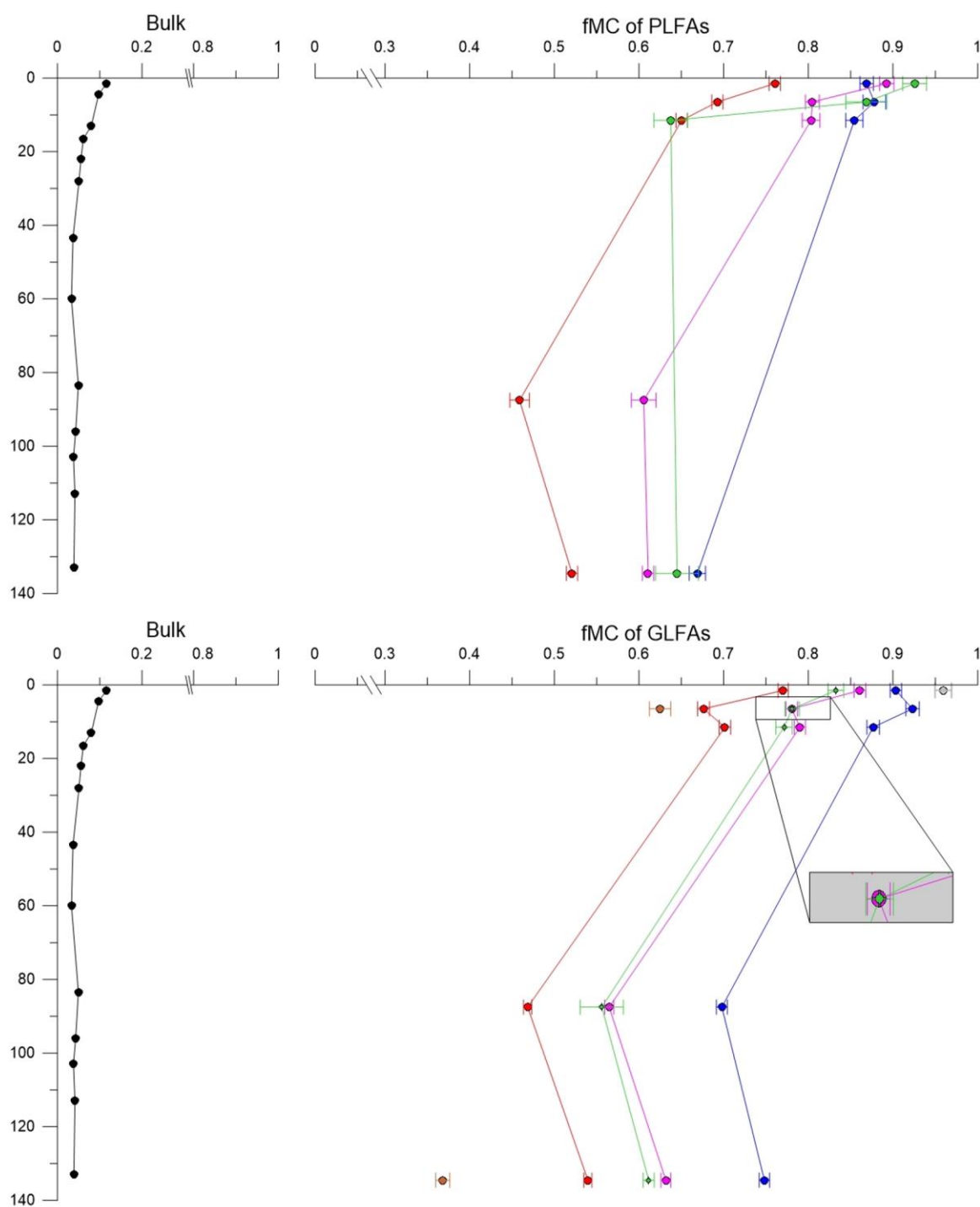


**Figure 18: Compound specific radiocarbon data of PLFAs and GLFAs. Grey:  $C_{14:0}$ ; Green:  $C_{15:0}$  i&aj; Pink:  $C_{16:0}$ ; Red:  $C_{16:1}$ ; Brown:  $C_{26:0}+C_{28:0}+C_{30:0}$**

nutrients in these layers, especially as XRF data show two distinctive events within 1 cm above and below the sample depth. These divergences could potentially impact the metabolism (Arndt et al., 2013) of the microbial communities and therefore also impact the assimilation of modern versus ancient carbon (Bianchi, 2011). Furthermore, all biomarker abundances and indices, SAR, IPL data, and

radiocarbon data show a strong homogeneity below 50 cm. This suggests that the microbial communities are uniform in this anoxic, semi steady-state regime, with minor change in their CSRD signature and therefore utilization of ancient OM. However, further studies would be needed to clarify this hypothesis.

The three samples in the topmost 15 cm show an overall fast decrease in  $F^{14}C$  of the individual PLFAs with increasing depth. Within this transition, biomarker abundances suggest a relative decrease in recently synthesized marine OM versus ancient petrogenic OM, similarly reflected in bulk OM radiocarbon data. Consequently, an increase in fossil carbon assimilation took place with increasing depth.

Of the combined long-chained FA fraction  $C_{26:0}+C_{28:0}+C_{30:0}$  only two successful purifications and measurements were achieved. Therefore, no in-depth analysis of the radiocarbon data was performed. However, the radiocarbon ages of these compounds are within the same range as anthropogenically derived carbon from fossil fuel burning, found in snow on Greenland glaciers (Stubbins et al., 2012). In the same study, the authors further reported long-chained fatty acids to be deposited similarly. These findings would correlate to this studies' results, although it is worth noting that fossil fuel derivatives would be radiocarbon free.

### 4.2.4 Isotope mass balance calculation

To determine to what extent the organic matter degrading bacteria are using fossil and modern OM, an isotope mass balance calculation (Equation 14) was applied using the two previously assigned endmembers of GLFA  $C_{14:0}$  for modern OM and radiocarbon free, fossil OM. As the GL fraction has been shown to represent a mixed signal of different precursor sources, a detailed analysis of the endmember mixing model was performed only based on the radiocarbon content of the PLFAs.

The results of the mixing model showed diverse values of fossil carbon assimilated into the microbial biomass (Table 5), ranging from 4 % at the core top in the  $C_{15:0\ i\&ai}$  up to 52 % at 86-89 cm in  $C_{16:1}$  which demonstrates that substantial degradation of ancient material is occurring in the sediment. Nevertheless, by comparing to the fossil part of the bulk OM ranging from 90.4 % to 96.4 % of the TOC, it is clear that the recently synthesized modern OM is the highly preferred substrate of the bacterial communities and outweighs the utilized fossil substrate.

The signal of the PLFA  $C_{15:0\ i\&ai}$  has previously been assigned in marine sediments to be primarily of SRB origin (Bühning et al., 2014). With fossil carbon proportions being the lowest at the core top with 4 %

and an increase to 9 %, 34 %, and 33 % at 5-8 cm, 10-13 cm, and 133-136 cm respectively, an increasing reliance on the fossil OM as a substrate is apparent. The utilized fossil fraction increased from the core top to the deeper parts of the core by nearly an order of magnitude, whereas the modern fraction of the bulk OM only decreased by about two thirds, from 11.6 % to 3.9 %. A disproportional increase in the utilized fossil carbon relative to the fossil components of the bulk OM was observed in the FA markers for SRB, indicating a predominant utilization of modern carbon in the early stages of diagenesis and an increasing importance of ancient carbon at later stages. The “priming effect” has to be considered as a possible cause of this shift in substrate utilization (compare below).

Similar trends have been observed for the other three FA of  $C_{16:0}$ ,  $C_{16:1}$ , and  $C_{18:1+18:2}$ . However, with different intensities regarding the fossil fraction that was used for biosynthesis and the extent by which the relative amounts increased with depths. Odd-numbered, monounsaturated, and methyl-branched PLFAs can be assigned as purely bacterial origin (Guckert et al., 1985; Ringelberg et al., 1997) and  $C_{16:0}$  was reported to be ubiquitous in bacteria (Petsch et al., 2001). All the analyzed FAs were reported to be present in similar source organisms, such as methanotrophic bacteria (Bowman et al., 1991). This similarity in occurrence causes their radiocarbon signature to represent a mixed signal of different microbial organisms in the sediment, contributing partially to the pool of the analyzed FAs. A more detailed taxonomic characterization of the individual PLFA precursor organisms is not possible with the approach used for this thesis and is beyond the scope of the study.

Considering these mixed signals, the most extreme value was calculated for the PLFA  $C_{16:1}$  at 86-89 cm, which suggests that 52 % of its carbon derives from fossil carbon and indicated that some bacterial strains can utilize even higher percentages of ancient OM. However, whether or not they can thrive purely on ancient material has to be determined in future studies.

### 4.2.5 Environmental controls

While the assimilation of petrogenic carbon by bacterial communities has been shown to be an efficient process (Petsch et al., 2003, 2001), significant portions of fossil OM from shale weathering is expected to be buried in marine sediments (Drenzek et al., 2009). The radiocarbon data obtained in this study provide further evidence for the incorporation of fossil carbon into the microbial biomass within fjord/marine sediments and therefore a release of ancient carbon as a metabolic product to the sediment, water column, and eventually to the atmosphere. However, comparing these findings to previous studies, a more diverse situation is likely. Analyzing oil spill contaminated sediments in a rocky tidal zone, Slater et al. (2006) reported saturated and mono-unsaturated FAs to be significantly

depleted in  $^{14}\text{C}$ , in agreement with the results of this thesis. The authors suggested the incorporation of petroleum-derived  $^{14}\text{C}$  free carbon into microbial biomass. On the contrary, Wakeham et al. (2006) found only minor carry-over of  $^{14}\text{C}$ -depleted carbon to microbial biomass in an oil spill contaminated marsh sediment. In these two studies, the ancient carbon substrates were imported through anthropogenic activity to the sediments, other studies show a more uniform picture of active utilization of ancient carbon, when a natural input of ancient carbon occurs on a geological time scale (Bardgett et al., 2007; Cui et al., 2016b; Petsch et al., 2001), as is the case in this study's location. Schubotz et al. (2011) came to a similar conclusion of microbial communities thriving on asphalt substrates in the Gulf of Mexico, however, without using  $^{14}\text{C}$  as an inverse tracer. Recent work by Bogard et al. (2019) in arctic lacustrine environments reported minimal remineralization of available ancient OM associated with remineralization of exclusively modern OM derived from carbon fixation of atmospheric  $\text{CO}_2$ , raising the question of the controlling or limiting factors for ancient OM utilization.

Consequently, questions arise as to whether the microbial community in Hornsund Fjord has adapted to the ancient substrate supply or if the limitation of fresh material forces them to utilize the ancient substrate. Within the framework of this thesis, these questions cannot be resolved. However, as the biomarker indices show a distinctive difference in the input of ancient and modern carbon with depth, the potential effects of the "priming effect" (Bingeman et al., 1953) have to be considered.

### 4.2.6 Priming Effect

The "priming effect" is a well-studied phenomenon in soil science, however, it has only been a focus in marine studies within the recent decades (Bianchi, 2011). Generally, "priming" describes the mechanism of enhanced degradation of recalcitrant OM by the input of labile OM into a system (Bingeman et al., 1953; Kuzyakov et al., 2000). This is of particular interest in this study, as mineralization of very recalcitrant black carbon has been shown to increase between 36 % and 600 % after priming (Hamer et al., 2004). Furthermore, it has been shown that marine sediments can be primed due to fresh substrates like algae (Turnewitsch et al., 2007).

Considering the sedimentary setting of the analyzed Hornsund Fjord sediment, the priming effect may play an important role in terms of OM degradation in the local sediment. A rate-limiting step in the degradational process is the hydrolysis of OM by extracellular enzymes (Arnosti, 2011), which are either released freely or stay attached to the cell (Hoppe, 1991). In the case of priming, these extracellular enzymes and their resulting metabolites are initially produced by decomposers of labile

OM, which later stimulated the remineralization or the metabolism of decomposers targeting recalcitrant OM (Bianchi, 2011).

In the analyzed core, primarily ancient recalcitrant petrogenic OM gets deposited with increasing relative contributions of fresh labile OM towards the core top. IPL data indicate a high consistency within the microbial community and suggest environmental factors to control the microbial utilization of ancient OM. Associated radiocarbon ages of the degrading bacterial communities further indicate increasing amounts of ancient OM being used for biosynthesis with increasing depth, therefore longer duration of remineralization processes and a possible enforcement of the priming effect. Simultaneously, analyzed biomarkers and bulk OM parameters suggest different diagenetic settings and enhanced degradational processes towards the core top. The disproportional increase in the assimilation of ancient carbon into the  $C_{15:0}$  fraction with depths may not just be related to a decrease in available labile modern carbon, but also related to a longer accumulation of exoenzymes in the deeper regions of the core. This raises the question of whether the microbial communities would be able to utilize the ancient OM exclusively or if the input of the labile marine OM forms the basis of the ancient OM utilization potential of the microbial community.

### 5. Conclusion

Atmospheric temperature changes were expected to be the primary control on OM input to the sediment. Performed biomarker analysis suggests that sedimentary OM is primarily composed of remobilized petrogenic OM supplied from glacial meltwater streams. The position of the tidewater glacier front is expected to be the strongest governing factor on the TOC input to the sediment. TOC values remained relatively constant throughout the core in spite of decreasing total sedimentary load by an order of magnitude comparing pre-1980 to post-1990 levels. Relative contributions of marine to petrogenic OM increased during this period from about 5 % to 13 % of total TOC. Overall OM deposition rates decreased from both pools, with increasing distance to the glacial front. Whereas petrogenic OM input is directly linked to meltwater sediment load supply, a decrease in overall marine OM burial is expected to be either linked to lower marine detritus or stronger remineralization of the modern material. Diagenetic processes are expected to reduce TOC values, especially in the topmost 20 cm of the core, due to lower sedimentation rates. Recently produced OM from terrestrial plants and soils were identified as a negligible fraction of the sedimentary TOC. Long term atmospheric temperature changes were shown to impact relative distribution of marine OM exported into the sediment. Winter

temperatures may play an essential role due to changing sea-ice conditions controlling spring plankton blooms. However, these results fall into the uncertainty range of the age model. A full assessment of working hypothesis (1) was not possible, due to a lack of spatial resolution.

CSRD was performed on IPLs to determine the capability of the benthic microbial communities to utilize ancient carbon from petrogenic origin. Radiocarbon data of all analyzed PLFAs show a distinctive signal of ancient petrogenic carbon being assimilated into the microbial biomass. Individual PLFAs show similarly increasing trends of ancient carbon assimilation with increasing depth and therefore prolonged time of remineralization. Accounting to an isotope mass balance model using two endmember values, fossil OM accounted for 4 % to 52 % of the utilized substrate. The two deepest samples have shown the strongest utilization of ancient material indicating two possible control mechanisms. First, increasing relative contributions of petrogenic carbon to the TOC pool in the deeper sediment may force microbial communities to use ancient material as substrate, due to inaccessibility of labile, modern OM. Secondly, prolonged time of degradation of labile OM allowed the microbial communities to develop sufficient quantities of byproducts like exoenzymes to enable the utilization of previously inaccessible recalcitrant OM, due to priming. The results of this study indicate the latter scenario is more likely. Further, the lipids in the GLFA fractions were found to consist of a mixed signal of GL, TAGs, and free FAs, possibly explaining minor differences in the radiocarbon signal of the PLFAs. However, the similar trends of both GLFA and PLFA indicate robustness of the method.

Direct indications for priming due to changing quantities of fresh marine input were not observed, as the input of labile marine OM was fairly uniform throughout the core. However, a disproportional increase in ancient OM utilization in the topmost 15 cm was observed associated with decreasing labile marine OM. Compared to the relatively stable proportions of ancient OM being utilized and overall labile marine OM content in the deeper samples. Two possible controls were identified: the time of deposition and the diagenetic setting. To clarify this issue further studies have to be conducted.

### 5.1 Outlook

With the aforementioned conclusions some further questions arise. Biomarker abundances have shown shifts of OM input to the sediment. However, the extent of degradational effects could not be assessed completely due to the lack of pore water data. Therefore, including pore water chemistry into future sampling strategies would be helpful. Further, the geochemical zonation would allow categorization of microbial communities in more detail and allow insights into potential metabolic pathways. Genetic characterization of the present microbial communities would allow comparison of

different geographical locations to one another, and whether the ancient OM substrates cause different populations to thrive. The analysis of pore water DIC radiocarbon signatures would also allow verification of the assumptions regarding the metabolic pathways of the presumably heterotrophic bacterial communities in the sediment.

The CSRD data has shown microbial communities are capable of utilizing ancient carbon. However, both rates and pathways are fairly unknown. Incubation experiments are considered to be a reliable method to determine both in a controlled setting. They would allow investigation of the importance of priming, changing labile modern (marine) OM input, and whether or not the microbial communities are capable of solely thriving on the ancient material. This may be of high importance as with changing climatic conditions different OM input scenarios become likely. The aforementioned pore water data would further inform on accurate simulated in-situ conditions.

Additionally, studies in different fjord systems but also in shelf regions will be needed to assess these processes on a global scale, especially since strong input by ancient carbon occurs all over the arctic regions from both petrogenic OM but also from permafrost soils. The latter is of particular importance as the inputs to arctic shelves are projected to increase dramatically within the next decades. As permafrost derived OM is widely seen as highly labile, it could further enhance a positive carbon feedback.

## 6. Acknowledgements

I would like to express my gratitude to my supervisors Gesine Mollenhauer and Florence Schubotz, who guided me exceptionally well through my thesis whenever I needed their advice. Furthermore, I would like to thank everyone from the two groups of the marine geochemistry at AWI, who taught me a lot in the last two years working there. Especially, I want to thank Jens Hefter who guided me through all the lab work with so much wisdom and patience, without the thesis would not have been possible. Also, I would like to thank Matthias Forwick and Witold Szczuciński whose corporation provided the basis for this thesis by entrusting the used material, supplementary data, and a lot of their expertise, which helped me out a lot during this work. Finally, I want to thank all the awesome people in Bremen and Bremerhaven who have made the master's program, not just a formative but joyful experience, which helped me to personal growth as well.

## 7. References

- Adams, R.M., Hurd, B.H., Lenhart, S., Leary, N., 1998. Effects of global climate change on agriculture: an interpretative review. *Clim Res* 12.
- Akondi, R.N., Trexler, R.V., Pfiffner, S.M., Mouser, P.J., Sharma, S., 2017. Modified Lipid Extraction Methods for Deep Subsurface Shale. *Front. Microbiol.* 8, 1408. <https://doi.org/10.3389/fmicb.2017.01408>
- Arndt, S., Jørgensen, B.B., LaRowe, D.E., Middelburg, J.J., Pancost, R.D., Regnier, P., 2013. Quantifying the degradation of organic matter in marine sediments: A review and synthesis. *Earth-Sci. Rev.* 123, 53–86. <https://doi.org/10.1016/j.earscirev.2013.02.008>
- Arnosti, C., 2011. Microbial extracellular enzymes and the marine carbon cycle. *Annu. Rev. Mar. Sci.* 3, 401–425.
- Bardgett, R.D., Richter, A., Bol, R., Garnett, M.H., Bäumler, R., Xu, X., Lopez-Capel, E., Manning, D.A.C., Hobbs, P.J., Hartley, I.R., Wanek, W., 2007. Heterotrophic microbial communities use ancient carbon following glacial retreat. *Biol. Lett.* 3, 487–490. <https://doi.org/10.1098/rsbl.2007.0242>
- Bauer, J.E., Cai, W.-J., Raymond, P.A., Bianchi, T.S., Hopkinson, C.S., Regnier, P.A.G., 2013. The changing carbon cycle of the coastal ocean. *Nature* 504, 61–70. <https://doi.org/10.1038/nature12857>
- Bhatia, M.P., Das, S.B., Longnecker, K., Charette, M.A., Kujawinski, E.B., 2010. Molecular characterization of dissolved organic matter associated with the Greenland ice sheet. *Geochim. Cosmochim. Acta* 74, 3768–3784. <https://doi.org/10.1016/j.gca.2010.03.035>
- Bianchi, T.S., 2011. The role of terrestrially derived organic carbon in the coastal ocean: A changing paradigm and the priming effect. *Proc. Natl. Acad. Sci.* 108, 19473–19481.
- Bianchi, T.S., Canuel, E.A., 2011. *Chemical biomarkers in aquatic ecosystems*. Princeton University Press.
- Bianchi, T.S., Cui, X., Blair, N.E., Burdige, D.J., Eglinton, T.I., Galy, V., 2018. Centers of organic carbon burial and oxidation at the land-ocean interface. *Org. Geochem.* 115, 138–155. <https://doi.org/10.1016/j.orggeochem.2017.09.008>
- Bingeman, C.W., Varner, J.E., Martin, W.P., 1953. The Effect of the Addition of Organic Materials on the Decomposition of an Organic Soil 1. *Soil Sci. Soc. Am. J.* 17, 34–38.
- Błaszczyk, M., Jania, J.A., Kolondra, L., 2013. Fluctuations of tidewater glaciers in Hornsund Fjord (Southern Svalbard) since the beginning of the 20th century. *Pol. Polar Res.* 34, 327–352. <https://doi.org/10.2478/popore-2013-0024>
- Bligh, E.G., Dyer, W.J., 1959. A rapid method of total lipid extraction and purification. *Can. J. Biochem. Physiol.* 37, 911–917.
- Bogard, M.J., Kuhn, C.D., Johnston, S.E., Striegl, R.G., Holtgrieve, G.W., Dornblaser, M.M., Spencer, R.G.M., Wickland, K.P., Butman, D.E., 2019. Negligible cycling of terrestrial carbon in many lakes of the arid circumpolar landscape. *Nat. Geosci.* 12, 180–185. <https://doi.org/10.1038/s41561-019-0299-5>
- Bowman, J.P., Skerratt, J.H., Nichols, P.D., Sly, L.I., 1991. Phospholipid fatty acid and lipopolysaccharide fatty acid signature lipids in methane-utilizing bacteria. *FEMS Microbiol. Lett.* 85, 15–21.
- Brander, K., 2010. Impacts of climate change on fisheries. *J. Mar. Syst.* 79, 389–402. <https://doi.org/10.1016/j.jmarsys.2008.12.015>

- Bühning, S.I., Kamp, A., Wörmer, L., Ho, S., Hinrichs, K.-U., 2014. Functional structure of laminated microbial sediments from a supratidal sandy beach of the German Wadden Sea (St. Peter-Ording). *J. Sea Res.* 85, 463–473. <https://doi.org/10.1016/j.seares.2013.08.001>
- Burdige, D.J., 2007. Preservation of organic matter in marine sediments: controls, mechanisms, and an imbalance in sediment organic carbon budgets? *Chem. Rev.* 107, 467–485.
- Burdige, D.J., 2005. Burial of terrestrial organic matter in marine sediments: A re-assessment. *Glob. Biogeochem. Cycles* 19.
- Burrows, K., Kinney, P., 2016. Exploring the Climate Change, Migration and Conflict Nexus. *Int. J. Environ. Res. Public Health* 13, 443. <https://doi.org/10.3390/ijerph13040443>
- Change, I.C., 2007. The physical science basis. *Contrib. Work. Group Fourth Assess. Rep. Intergov. Panel Clim. Change* 996.
- Ćmiel, S.R., Fabiańska, M.J., 2004. Geochemical and petrographic properties of some Spitsbergen coals and dispersed organic matter. *Int. J. Coal Geol.* 57, 77–97. <https://doi.org/10.1016/j.coal.2003.09.002>
- Cottier, F.R., Nilsen, F., Skogseth, R., Tverberg, V., Skarðhamar, J., Svendsen, H., 2010. Arctic fjords: a review of the oceanographic environment and dominant physical processes. *Geol. Soc. Lond. Spec. Publ.* 344, 35–50. <https://doi.org/10.1144/SP344.4>
- Cranwell, P.A., Eglinton, G., Robinson, N., 1987. Lipids of aquatic organisms as potential contributors to lacustrine sediments—II. *Org. Geochem.* 11, 513–527.
- Cui, X., Bianchi, T.S., Jaeger, J.M., Smith, R.W., 2016a. Biospheric and petrogenic organic carbon flux along southeast Alaska. *Earth Planet. Sci. Lett.* 452, 238–246. <https://doi.org/10.1016/j.epsl.2016.08.002>
- Cui, X., Bianchi, T.S., Jaeger, J.M., Smith, R.W., 2016b. Biospheric and petrogenic organic carbon flux along southeast Alaska. *Earth Planet. Sci. Lett.* 452, 238–246. <https://doi.org/10.1016/j.epsl.2016.08.002>
- Cui, X., Bianchi, T.S., Savage, C., 2017. Erosion of modern terrestrial organic matter as a major component of sediments in fjords. *Geophys. Res. Lett.* 44, 1457–1465. <https://doi.org/10.1002/2016GL072260>
- Cui, X., Bianchi, T.S., Savage, C., Smith, R.W., 2016c. Organic carbon burial in fjords: Terrestrial versus marine inputs. *Earth Planet. Sci. Lett.* 451, 41–50. <https://doi.org/10.1016/j.epsl.2016.07.003>
- da Silva, V. de P.R., 2004. On climate variability in Northeast of Brazil. *J. Arid Environ.* 58, 575–596. <https://doi.org/10.1016/j.jaridenv.2003.12.002>
- Dallmann, W.K., Atakan, K., Blomeier, D., Bond, D., Christiansen, H., Elvevold, S., Forwick, M., Gerland, S., Grundvåg, S.-A., Hagen, J.-O., Hormes, A., Jernas, P.E., Kohler, J., Laberg, J.S., Majka, J., Mørk, A., Nasuti, A., Nuth, C., Olaussen, S., Olesen, O., Ottemöller, L., Ottesen, R.T., Pavlov, V., Pavlova, O., Piepjohn, K., Reymert, P.K., Salvigsen, O., Sander, G., Storheim, B.M., Sundjord, A., Vorren, T.O., 2015. *Geoscience Atlas of Svalbard (Atlas No. 148)*. The Norwegian Polar Institute.
- Dalsgaard, J., St. John, M., Kattner, G., Müller-Navarra, D., Hagen, W., 2003. Fatty acid trophic markers in the pelagic marine environment. *Adv. Mar. Biol.* 46, 225–340. [https://doi.org/10.1016/S0065-2881\(03\)46005-7](https://doi.org/10.1016/S0065-2881(03)46005-7)

- Drenzek, N.J., Hughen, K.A., Montluçon, D.B., Southon, J.R., 2009. A new look at old carbon in active margin sediments 5.
- Drenzek, N.J., Montluçon, D.B., Yunker, M.B., Macdonald, R.W., Eglinton, T.I., 2007. Constraints on the origin of sedimentary organic carbon in the Beaufort Sea from coupled molecular  $^{13}\text{C}$  and  $^{14}\text{C}$  measurements. *Mar. Chem.* 103, 146–162.
- Dunstan, G.A., Volkman, J.K., Barrett, S.M., Leroi, J.-M., Jeffrey, S.W., 1993. Essential polyunsaturated fatty acids from 14 species of diatom (Bacillariophyceae). *Phytochemistry* 35, 155–161. [https://doi.org/10.1016/S0031-9422\(00\)90525-9](https://doi.org/10.1016/S0031-9422(00)90525-9)
- Eglinton, G., Hamilton, R.J., 1967. Leaf Epicuticular Waxes. *Science* 156, 1322–1335. <https://doi.org/10.1126/science.156.3780.1322>
- Eglinton, T.I., Aluwihare, L.I., Bauer, J.E., Druffel, E.R.M., McNichol, A.P., 1996. Gas Chromatographic Isolation of Individual Compounds from Complex Matrices for Radiocarbon Dating. *Anal. Chem.* 68, 904–912. <https://doi.org/10.1021/ac9508513>
- Elvert, M., Boetius, A., Knittel, K., Jørgensen, B.B., 2003. Characterization of Specific Membrane Fatty Acids as Chemotaxonomic Markers for Sulfate-Reducing Bacteria Involved in Anaerobic Oxidation of Methane. *Geomicrobiol. J.* 20, 403–419. <https://doi.org/10.1080/01490450303894>
- Fang, J., Barcelona, M.J., Semrau, J.D., 2000. Characterization of methanotrophic bacteria on the basis of intact phospholipid profiles. *FEMS Microbiol. Lett.* 189, 67–72.
- Feng, X., Vonk, J.E., van Dongen, B.E., Gustafsson, O., Semiletov, I.P., Dudarev, O.V., Wang, Z., Montluçon, D.B., Wacker, L., Eglinton, T.I., 2013. Differential mobilization of terrestrial carbon pools in Eurasian Arctic river basins. *Proc. Natl. Acad. Sci.* 110, 14168–14173. <https://doi.org/10.1073/pnas.1307031110>
- Fontaine, S., Mariotti, A., Abbadie, L., 2003. The priming effect of organic matter: a question of microbial competition? *Soil Biol. Biochem.* 35, 837–843. [https://doi.org/10.1016/S0038-0717\(03\)00123-8](https://doi.org/10.1016/S0038-0717(03)00123-8)
- Forwick, M., 2019. Supplementary Data - Email correspondence - Department of Geosciences, The Arctic University of Norway, Norway.
- Galy, V., Beysac, O., France-Lanord, C., Eglinton, T., 2008. Recycling of Graphite During Himalayan Erosion: A Geological Stabilization of Carbon in the Crust. *Science* 322, 943. <https://doi.org/10.1126/science.1161408>
- Gontikaki, E., Thornton, B., Huvenne, V.A.I., Witte, U., 2013. Negative Priming Effect on Organic Matter Mineralisation in NE Atlantic Slope Sediments. *PLoS ONE* 8, e67722. <https://doi.org/10.1371/journal.pone.0067722>
- Grzelak, K., Kotwicki, L., 2012. Meiofaunal distribution in Hornsund fjord, Spitsbergen. *Polar Biol.* 35, 269–280. <https://doi.org/10.1007/s00300-011-1071-5>
- Guckert, J.B., Antworth, C.P., Nichols, P.D., White, D.C., 1985. Phospholipid, ester-linked fatty acid profiles as reproducible assays for changes in prokaryotic community structure of estuarine sediments. *FEMS Microbiol. Ecol.* 1, 147–158.
- Guillemette, F., Bianchi, T.S., Spencer, R.G.M., 2017. Old before your time: Ancient carbon incorporation in contemporary aquatic foodwebs. *Limnol. Oceanogr.* 62, 1682–1700. <https://doi.org/10.1002/lno.10525>

- Haddeland, I., Heinke, J., Biemans, H., Eisner, S., Flörke, M., Hanasaki, N., Konzmann, M., Ludwig, F., Masaki, Y., Schewe, J., Stacke, T., Tessler, Z.D., Wada, Y., Wisser, D., 2014. Global water resources affected by human interventions and climate change. *Proc. Natl. Acad. Sci.* 111, 3251–3256. <https://doi.org/10.1073/pnas.1222475110>
- Hamer, U., Marschner, B., Brodowski, S., Amelung, W., 2004. Interactive priming of black carbon and glucose mineralisation. *Org. Geochem.* 35, 823–830.
- Hanson, R.S., Hanson, T.E., 1996. Methanotrophic bacteria. *Microbiol Mol Biol Rev* 60, 439–471.
- Hartnett, H.E., Keil, R.G., Hedges, J.I., Devol, A.H., 1998. Influence of oxygen exposure time on organic carbon preservation in continental margin sediments. *Nature* 391, 572–575. <https://doi.org/10.1038/35351>
- Harvey, H.R., Fallon, R.D., Patton, J.S., 1986. The effect of organic matter and oxygen on the degradation of bacterial membrane lipids in marine sediments. *Geochim. Cosmochim. Acta* 50, 795–804.
- Hedges, J.I., Baldock, J.A., Gélinas, Y., Lee, C., Peterson, M., Wakeham, S.G., 2001. Evidence for non-selective preservation of organic matter in sinking marine particles. *Nature* 409, 801.
- Hemingway, J.D., Rothman, D.H., Grant, K.E., Rosengard, S.Z., Eglinton, T.I., Derry, L.A., Galy, V.V., 2019. Mineral protection regulates long-term global preservation of natural organic carbon. *Nature* 570, 228.
- Ho, S., Meyers, P.A., 1994. Variability of early diagenesis in lake sediments: Evidence from the sedimentary geolipid record in an isolated tam 16.
- Hood, E., Battin, T.J., Fellman, J., O'Neel, S., Spencer, R.G.M., 2015. Storage and release of organic carbon from glaciers and ice sheets. *Nat. Geosci.* 8, 91–96. <https://doi.org/10.1038/ngeo2331>
- Hood, E., Fellman, J., Spencer, R.G.M., Hernes, P.J., Edwards, R., D'Amore, D., Scott, D., 2009. Glaciers as a source of ancient and labile organic matter to the marine environment. *Nature* 462, 1044–1047. <https://doi.org/10.1038/nature08580>
- Hopmans, E.C., Schouten, S., Sinninghe Damsté, J.S., 2016. The effect of improved chromatography on GDGT-based palaeoproxies. *Org. Geochem.* 93, 1–6. <https://doi.org/10.1016/j.orggeochem.2015.12.006>
- Hopmans, E.C., Weijers, J.W.H., Schefuß, E., Herfort, L., Sinninghe Damsté, J.S., Schouten, S., 2004. A novel proxy for terrestrial organic matter in sediments based on branched and isoprenoid tetraether lipids. *Earth Planet. Sci. Lett.* 224, 107–116. <https://doi.org/10.1016/j.epsl.2004.05.012>
- Hoppe, H.-G., 1991. Microbial extracellular enzyme activity: a new key parameter in aquatic ecology, in: *Microbial Enzymes in Aquatic Environments*. Springer, pp. 60–83.
- Hunt, A., Watkiss, P., 2011. Climate change impacts and adaptation in cities: a review of the literature. *Clim. Change* 104, 13–49. <https://doi.org/10.1007/s10584-010-9975-6>
- Hwang, J., Druffel, E.R.M., 2005. Blank Correction for  $\Delta^{14}\text{C}$  Measurements in Organic Compound Classes of Oceanic Particulate Matter. *Radiocarbon* 47, 75–87. <https://doi.org/10.1017/S0033822200052218>
- Kalscheuer, R., Stöveken, T., Malkus, U., Reichelt, R., Golyshin, P.N., Sabirova, J.S., Ferrer, M., Timmis, K.N., Steinbüchel, A., 2007. Analysis of storage lipid accumulation in *Alcanivorax borkumensis*:

- evidence for alternative triacylglycerol biosynthesis routes in bacteria. *J. Bacteriol.* 189, 918–928.
- Kellermann, M.Y., Wegener, G., Elvert, M., Yoshinaga, M.Y., Lin, Y.-S., Holler, T., Mollar, X.P., Knittel, K., Hinrichs, K.-U., 2012. Autotrophy as a predominant mode of carbon fixation in anaerobic methane-oxidizing microbial communities. *Proc. Natl. Acad. Sci.* 109, 19321–19326. <https://doi.org/10.1073/pnas.1208795109>
- Killops, S., Killops, V., 2013. Carbon, the Earth and Life, in: *Introduction to Organic Geochemistry*. Blackwell Publishing Ltd., Malden, MA USA. <https://doi.org/10.1002/9781118697214.ch1>
- Kim, J.-H., Peterse, F., Willmott, V., Kristensen, D.K., Baas, M., Schouten, S., Sinninghe Damsté, J.S., 2011. Large ancient organic matter contributions to Arctic marine sediments (Svalbard). *Limnol. Oceanogr.* 56, 1463–1474. <https://doi.org/10.4319/lo.2011.56.4.1463>
- Kohler, J., James, T.D., Murray, T., Nuth, C., Brandt, O., Barrand, N.E., Aas, H.F., Luckman, A., 2007. Acceleration in thinning rate on western Svalbard glaciers. *Geophys. Res. Lett.* 34. <https://doi.org/10.1029/2007GL030681>
- Koziorowska, K., Kuliński, K., Pempkowiak, J., 2018. Comparison of the burial rate estimation methods of organic and inorganic carbon and quantification of carbon burial in two high Arctic fjords. *Oceanologia* 60, 405–418. <https://doi.org/10.1016/j.oceano.2018.02.005>
- Koziorowska, K., Kuliński, K., Pempkowiak, J., 2016. Sedimentary organic matter in two Spitsbergen fjords: Terrestrial and marine contributions based on carbon and nitrogen contents and stable isotopes composition. *Cont. Shelf Res.* 113, 38–46. <https://doi.org/10.1016/j.csr.2015.11.010>
- Kristensen, E., Andersen, F.Ø., Holmboe, N., Holmer, M., Thongtham, N., 2000. Carbon and nitrogen mineralization in sediments of the Bangrong mangrove area, Phuket, Thailand. *Aquat. Microb. Ecol.* 22, 199–213.
- Kuzyakov, Y., Friedel, J.K., Stahr, K., 2000. Review of mechanisms and quantification of priming effects. *Soil Biol. Biochem.* 32, 1485–1498.
- Lewińska-Preis, L., Fabiańska, M.J., Ćmiel, S., Kita, A., 2009. Geochemical distribution of trace elements in Kaffioyra and Longyearbyen coals, Spitsbergen, Norway. *Int. J. Coal Geol.* 80, 211–223. <https://doi.org/10.1016/j.coal.2009.09.007>
- Ljungdahl, L.G., Wood, H.G., 1969. Total synthesis of acetate from CO<sub>2</sub> by heterotrophic bacteria. *Annu. Rev. Microbiol.* 23, 515–538.
- Lydersen, C., Assmy, P., Falk-Petersen, S., Kohler, J., Kovacs, K.M., Reigstad, M., Steen, H., Strøm, H., Sundfjord, A., Varpe, Ø., Walczowski, W., Weslawski, J.M., Zajaczkowski, M., 2014. The importance of tidewater glaciers for marine mammals and seabirds in Svalbard, Norway. *J. Mar. Syst.* 129, 452–471. <https://doi.org/10.1016/j.jmarsys.2013.09.006>
- Majewski, W., Szczuciński, W., Zajaczkowski, M., 2009. Interactions of Arctic and Atlantic water-masses and associated environmental changes during the last millennium, Hornsund (SW Svalbard). *Boreas* 38, 529–544. <https://doi.org/10.1111/j.1502-3885.2009.00091.x>
- Mangerud, J., Bondevik, S., Gulliksen, S., Karin Hufthammer, A., Høisæter, T., 2006. Marine 14C reservoir ages for 19th century whales and molluscs from the North Atlantic. *Quat. Sci. Rev.* 25, 3228–3245. <https://doi.org/10.1016/j.quascirev.2006.03.010>
- Marshall, C., Uguna, Jacob., Large, D.J., Meredith, W., Jochmann, M., Friis, B., Vane, C., Spiro, B.F., Snape, C.E., Orheim, A., 2015. Geochemistry and petrology of palaeocene coals from

- Spitzbergen — Part 2: Maturity variations and implications for local and regional burial models. *Int. J. Coal Geol.* 143, 1–10. <https://doi.org/10.1016/j.coal.2015.03.013>
- Meyer, V.D., Hefter, J., Köhler, P., Tiedemann, R., Gersonde, R., Wacker, L., Mollenhauer, G., 2019. Permafrost-carbon mobilization in Beringia caused by deglacial meltwater runoff, sea-level rise and warming. *Environ. Res. Lett.* 14, 085003. <https://doi.org/10.1088/1748-9326/ab2653>
- Meyers, P.A., 1997. Organic geochemical proxies of paleoceanographic, paleolimnologic, and paleoclimatic processes. *Org. Geochem.* 27, 213–250. [https://doi.org/10.1016/S0146-6380\(97\)00049-1](https://doi.org/10.1016/S0146-6380(97)00049-1)
- Mikkelsen, D.M., Rysgaard, S., Glud, R.N., 2008. Microalgal composition and primary production in Arctic sea ice: a seasonal study from Kobbefjord (Kangerluarsunnguaq), West Greenland. *Mar. Ecol. Prog. Ser.* 368, 65–74.
- Mollenhauer, G., Eglinton, T.I., 2007. Diagenetic and sedimentological controls on the composition of organic matter preserved in California Borderland Basin sediments. *Limnol. Oceanogr.* 52, 558–576. <https://doi.org/10.4319/lo.2007.52.2.0558>
- Mollenhauer, G., Kusch, S., Eglinton, T.I., Pearson, A., 2019. Compound-Specific Radiocarbon Measurements, in: *Encyclopedia of Ocean Sciences*. Elsevier, pp. 235–244. <https://doi.org/10.1016/B978-0-12-409548-9.11432-0>
- Mollenhauer, G., Rethemeyer, J., 2009. Compound-specific radiocarbon analysis – Analytical challenges and applications. *IOP Conf. Ser. Earth Environ. Sci.* 5, 012006. <https://doi.org/10.1088/1755-1307/5/1/012006>
- Moss, C.W., Lambert-Fair, M.A., 1989. Location of Double Bonds in Monounsaturated Fatty Acids of *Campylobacter cryaerophila* with Dimethyl Disulfide Derivatives and Combined Gas Chromatography-Mass Spectrometry. *J CLIN MICROBIOL* 4.
- Muckenhuber, S., Nilsen, F., Korosov, A., Sandven, S., 2016. Sea ice cover in Isfjorden and Hornsund, Svalbard (2000–2014) from remote sensing data. *The Cryosphere* 10, 149–158. <https://doi.org/10.5194/tc-10-149-2016>
- Mukamolova, G.V., Yanopolskaya, N.D., Votyakova, T.V., Popov, V.I., Kaprelyants, A.S., Kell, D.B., 1995. Biochemical changes accompanying the long-term starvation of *Micrococcus luteus* cells in spent growth medium. *Arch. Microbiol.* 163, 373–379.
- Müller, P.J., Suess, E., 1979. Productivity, sedimentation rate, and sedimentary organic matter in the oceans—I. Organic carbon preservation. *Deep Sea Res. Part Oceanogr. Res. Pap.* 26, 1347–1362.
- Musslewhite, C.L., McInerney, M.J., Dong, H., Onstott, T.C., Green-Blum, M., Swift, D., Macnaughton, S., White, D.C., Murray, C., Chien, Y.-J., 2003. The factors controlling microbial distribution and activity in the shallow subsurface. *Geomicrobiol. J.* 20, 245–261.
- Onarheim, I.H., Smedsrud, L.H., Ingvaldsen, R.B., Nilsen, F., 2014. Loss of sea ice during winter north of Svalbard. *Tellus Dyn. Meteorol. Oceanogr.* 66, 23933. <https://doi.org/10.3402/tellusa.v66.23933>
- Park, E., Hefter, J., Fischer, G., Iversen, M.H., Ramondenc, S., Nöthig, E.-M., Mollenhauer, G., 2019. Seasonality of archaeal lipid flux and GDGT-based thermometry in sinking particles of high-latitude oceans: Fram Strait (79°&thinsp;N) and Antarctic Polar Front (50°&thinsp;S). *Biogeosciences* 16, 2247–2268. <https://doi.org/10.5194/bg-16-2247-2019>

- Pawłowska, J., Zajączkowski, M., Szczuciński, W., Zaborska, A., Kucharska, M., Jernas, P.E., Forwick, M., 2017. The influence of Coriolis force driven water circulation on the palaeoenvironment of Hornsund (S Spitsbergen) over the last century. *Boreas* 46, 737–749. <https://doi.org/10.1111/bor.12249>
- Peters, K.E., Walters, C.C., Moldowan, J.M., 2005. *The biomarker guide*, 2nd ed. ed. Cambridge University Press, Cambridge, UK ; New York.
- Petsch, S.T., Edwards, K.J., Eglinton, T.I., 2003. Abundance, distribution and  $\delta^{13}\text{C}$  analysis of microbial phospholipid-derived fatty acids in a black shale weathering profile. *Org. Geochem.* 34, 731–743.
- Petsch, S.T., Eglinton, T.I., Edwards, K.J., 2001.  $^{14}\text{C}$ -Dead Living Biomass: Evidence for Microbial Assimilation of Ancient Organic Carbon During Shale Weathering. *Science* 292, 1127–1131. <https://doi.org/10.1126/science.1058332>
- Piwoż, K., Walkusz, W., Hapter, R., Wieczorek, P., Hop, H., Wiktor, J., 2009. Comparison of productivity and phytoplankton in a warm (Kongsfjorden) and a cold (Hornsund) Spitsbergen fjord in mid-summer 2002. *Polar Biol.* 32, 549–559. <https://doi.org/10.1007/s00300-008-0549-2>
- Reimer, P.J., 2004. *IntCal04*. *Radiocarbon* 46, 1029–1058.
- Reuveny, R., 2007. Climate change-induced migration and violent conflict. *Polit. Geogr.* 26, 656–673. <https://doi.org/10.1016/j.polgeo.2007.05.001>
- Ringelberg, D.B., Sutton, S., White, D.C., 1997. Biomass, bioactivity and biodiversity: microbial ecology of the deep subsurface: analysis of ester-linked phospholipid fatty acids. *FEMS Microbiol. Rev.* 20, 371–377. <https://doi.org/10.1111/j.1574-6976.1997.tb00322.x>
- Robbins, J.A., Edgington, D.N., 1975. Determination of recent sedimentation rates in Lake Michigan using Pb-210 and Cs-137. *Geochim. Cosmochim. Acta* 39, 285–304.
- Rohmer, M., Bisseret, P., Neunlist, S., 1992. The hopanoids, prokaryotic triterpenoids and precursors of ubiquitous molecular fossils. *Biol. Markers Sediments Pet.* 54, 1–17.
- Rossel, P.E., Elvert, M., Ramette, A., Boetius, A., Hinrichs, K.-U., 2011. Factors controlling the distribution of anaerobic methanotrophic communities in marine environments: evidence from intact polar membrane lipids. *Geochim. Cosmochim. Acta* 75, 164–184.
- Rütters, H., Sass, H., Cypionka, H., Rullkötter, J., 2001. Monoalkylether phospholipids in the sulfate-reducing bacteria *Desulfosarcina variabilis* and *Desulforhabdus amnigenus*. *Arch. Microbiol.* 176, 435–442.
- Saloranta, T.M., Svendsen, H., 2001. Across the Arctic front west of Spitsbergen: high-resolution CTD sections from 1998–2000. *Polar Res.* 20, 177–184. <https://doi.org/10.3402/polar.v20i2.6515>
- Schmidt, F., Koch, B.P., Witt, M., Hinrichs, K.-U., 2014. Extending the analytical window for water-soluble organic matter in sediments by aqueous Soxhlet extraction. *Geochim. Cosmochim. Acta* 141, 83–96. <https://doi.org/10.1016/j.gca.2014.06.009>
- Schouten, S., Hopmans, E.C., Sinninghe Damsté, J.S., 2013. The organic geochemistry of glycerol dialkyl glycerol tetraether lipids: A review. *Org. Geochem.* 54, 19–61. <https://doi.org/10.1016/j.orggeochem.2012.09.006>
- Schrader, H.-J., 1971. Fecal Pellets: Role in Sedimentation of Pelagic Diatoms. *Science* 174, 55. <https://doi.org/10.1126/science.174.4004.55>

- Schubotz, F., Lipp, J.S., Elvert, M., Kasten, S., Mollar, X.P., Zabel, M., Bohrmann, G., Hinrichs, K.-U., 2011. Petroleum degradation and associated microbial signatures at the Chapopote asphalt volcano, Southern Gulf of Mexico. *Geochim. Cosmochim. Acta* 75, 4377–4398.
- Schubotz, F., Wakeham, S.G., Lipp, J.S., Fredricks, H.F., Hinrichs, K.-U., 2009. Detection of microbial biomass by intact polar membrane lipid analysis in the water column and surface sediments of the Black Sea. *Environ. Microbiol.* 11, 2720–2734. <https://doi.org/10.1111/j.1462-2920.2009.01999.x>
- Seidel, M., Graue, J., Engelen, B., Köster, J., Sass, H., Rullkötter, J., 2012. Advection and diffusion determine vertical distribution of microbial communities in intertidal sediments as revealed by combined biogeochemical and molecular biological analysis. *Org. Geochem.* 52, 114–129. <https://doi.org/10.1016/j.orggeochem.2012.08.015>
- Seifert, W.K., Moldowan, J.M., 1980. Paleoreconstruction by biological markers.
- Shah, S.R., Mollenhauer, G., Ohkouchi, N., Eglinton, T.I., Pearson, A., 2008. Origins of archaeal tetraether lipids in sediments: Insights from radiocarbon analysis. *Geochim. Cosmochim. Acta* 72, 4577–4594.
- Skei, J., 1983. Why sedimentologists are interested in Fjords. *Sediment. Geol.* 36, 75–80. [https://doi.org/10.1016/0037-0738\(83\)90002-7](https://doi.org/10.1016/0037-0738(83)90002-7)
- Slater, G.F., Nelson, R.K., Kile, B.M., Reddy, C.M., 2006a. Intrinsic bacterial biodegradation of petroleum contamination demonstrated in situ using natural abundance, molecular-level <sup>14</sup>C analysis. *Org. Geochem.* 37, 981–989. <https://doi.org/10.1016/j.orggeochem.2006.06.014>
- Slater, G.F., Nelson, R.K., Kile, B.M., Reddy, C.M., 2006b. Intrinsic bacterial biodegradation of petroleum contamination demonstrated in situ using natural abundance, molecular-level <sup>14</sup>C analysis. *Org. Geochem.* 37, 981–989. <https://doi.org/10.1016/j.orggeochem.2006.06.014>
- Smith, R.W., Bianchi, T.S., Allison, M., Savage, C., Galy, V., 2015. High rates of organic carbon burial in fjord sediments globally. *Nat. Geosci.* 8, 450–453. <https://doi.org/10.1038/ngeo2421>
- Smola, Z.T., Tatarek, A., Wiktor, J.M., Wiktor, J.M.W., Kubiszyn, A., Węśławski, J.M., 2017. Primary producers and production in Hornsund and Kongsfjorden – comparison of two fjord systems. *Pol. Polar Res.* 38, 351–373. <https://doi.org/10.1515/popore-2017-0013>
- Stern, N., 2006. Stern Review: The economics of climate change.
- Stubbins, A., Hood, E., Raymond, P.A., Aiken, G.R., Sleighter, R.L., Hernes, P.J., Butman, D., Hatcher, P.G., Striegl, R.G., Schuster, P., Abdulla, H.A.N., Vermilyea, A.W., Scott, D.T., Spencer, R.G.M., 2012. Anthropogenic aerosols as a source of ancient dissolved organic matter in glaciers. *Nat. Geosci.* 5, 198–201. <https://doi.org/10.1038/ngeo1403>
- Sturt, H.F., Summons, R.E., Smith, K., Elvert, M., Hinrichs, K.-U., 2004. Intact polar membrane lipids in prokaryotes and sediments deciphered by high-performance liquid chromatography/electrospray ionization multistage mass spectrometry—new biomarkers for biogeochemistry and microbial ecology. *Rapid Commun. Mass Spectrom.* 18, 617–628. <https://doi.org/10.1002/rcm.1378>
- Sun, S., Meyer, V., Dolman, A.M., Winterfeld, M., Hefter, J., Dummann, W., McIntyre, C., Montluçon, D.B., Haghypour, N., Wacker, L., Gentz, T., Eglinton, T.I., Mollenhauer, G., 2019. <sup>14</sup>C blank assessment in small-scale compound-specific radiocarbon analysis of lipid biomarkers and lignin phenols. *Radiocarbon* 14. <https://doi.org/10.1017/RDC.2019.108>

- Syvitski, J.P., 1989. On the deposition of sediment within glacier-influenced fjords: oceanographic controls. *Mar. Geol.* 85, 301–329.
- Szczuciński, W., 2019. HH14-897 Age Model - Email correspondence - Department of Mineralogy and Petrology, Adam Mickiewicz University, Poland.
- Szczuciński, W., Schettler, Georg, Zajączkowski, M., 2006. Sediment accumulation rates, geochemistry and provenance in complex High Arctic fjord, Hornsund, Svalbard. Fourth ESF SEDIFLUX Science Meeting and First Workshop of I.A.G./A.I.G. SEDIBUD 1.
- Szczuciński, W., Zajączkowski, M., 2013. Factors Controlling Downward Fluxes of Particulate Matter in Glacier-Contact and Non-Glacier Contact Settings in a Subpolar Fjord (Billefjorden, Svalbard), in: Li, M.Z., Sherwood, C.R., Hill, P.R. (Eds.), *Sediments, Morphology and Sedimentary Processes on Continental Shelves*. John Wiley & Sons, Ltd, Chichester, West Sussex, UK, pp. 369–386. <https://doi.org/10.1002/9781118311172.ch18>
- Tarnocai, C., Canadell, J.G., Schuur, E.A.G., Kuhry, P., Mazhitova, G., Zimov, S., 2009. Soil organic carbon pools in the northern circumpolar permafrost region: SOIL ORGANIC CARBON POOLS. *Glob. Biogeochem. Cycles* 23, n/a-n/a. <https://doi.org/10.1029/2008GB003327>
- Turnewitsch, R., Domeyer, B., Graf, G., 2007. Experimental evidence for an effect of early-diagenetic interaction between labile and refractory marine sedimentary organic matter on nitrogen dynamics. *J. Sea Res.* 57, 270–280.
- Uchida, M., Shibata, Y., Kawamura, K., Kumamoto, Y., Yoneda, M., Ohkushi, K., Harada, N., Hirota, M., Mukai, H., Tanaka, A., al, et, 2001. Compound-Specific Radiocarbon Ages of Fatty Acids in Marine Sediments from the Western North Pacific. *Radiocarbon* 43, 949–956. <https://doi.org/10.1017/S0033822200041618>
- Vonk, J.E., Sánchez-García, L., van Dongen, B.E., Alling, V., Kosmach, D., Charkin, A., Semiletov, I.P., Dudarev, O.V., Shakhova, N., Roos, P., Eglinton, T.I., Andersson, A., Gustafsson, Ö., 2012. Activation of old carbon by erosion of coastal and subsea permafrost in Arctic Siberia. *Nature* 489, 137–140. <https://doi.org/10.1038/nature11392>
- Vonk, J.E., Tesi, T., Tesi, T., Bröder, L., Bröder, L., Holmstrand, H., Holmstrand, H., Hugelius, G., Hugelius, G., Andersson, A., Andersson, A., Dudarev, O., Dudarev, O., Semiletov, I., Semiletov, I., Semiletov, I., Gustafsson, Ö., Gustafsson, Ö., 2017. Distinguishing between old and modern permafrost sources in the northeast Siberian land&#8211;shelf system with compound-specific &#948;2H analysis [WWW Document]. <https://doi.org/info:doi/10.5194/tc-11-1879-2017>
- Wacker, Lukas, Bonani, G., Friedrich, M., Hajdas, I., Kromer, B., Němec, M., Ruff, M., Suter, M., Synal, H.-A., Vockenhuber, C., 2010. MICADAS: routine and high-precision radiocarbon dating. *Radiocarbon* 52, 252–262.
- Wacker, L., Christl, M., 2011. Data reduction for small radiocarbon samples—error propagation using the model of constant contamination 1.
- Wacker, L., Christl, M., Synal, H.-A., 2010. Bats: a new tool for AMS data reduction. *Nucl. Instrum. Methods Phys. Res. Sect. B Beam Interact. Mater. At.* 268, 976–979.
- Wakeham, S.G., McNichol, A.P., Kostka, J.E., Pease, T.K., 2006. Natural-abundance radiocarbon as a tracer of assimilation of petroleum carbon by bacteria in salt marsh sediments. *Geochim. Cosmochim. Acta* 70, 1761–1771. <https://doi.org/10.1016/j.gca.2005.12.020>

- Walinsky, S.E., Prahl, F.G., Mix, A.C., Finney, B.P., Jaeger, J.M., Rosen, G.P., 2009. Distribution and composition of organic matter in surface sediments of coastal Southeast Alaska. *Cont. Shelf Res.* 29, 1565–1579. <https://doi.org/10.1016/j.csr.2009.04.006>
- Wei, B., Jia, G., Hefter, J., Kang, M., Park, E., Mollenhauer, G., 2019. Comparison of the U37K', LDI, TEX86H and RI-OH temperature proxies in the northern shelf of the South China Sea. *Biogeosciences Discuss* 2019, 1–26. <https://doi.org/10.5194/bg-2019-345>
- Wenger, L.M., Isaksen, G.H., 2002. Control of hydrocarbon seepage intensity on level of biodegradation in sea bottom sediments. *Org. Geochem.* 33, 1277–1292.
- Wezslawski, J.M., Jankowski, A., Kwasniewski, S., Swerpel, S., Ryg, M., 1991. Summer hydrology and zooplankton in two Svalbard fjords Polish Polar Research, 445–460.
- Wheeler, T., von Braun, J., 2013. Climate Change Impacts on Global Food Security. *Science* 341, 508–513. <https://doi.org/10.1126/science.1239402>
- White, D.C., Davis, W.M., Nickels, J.S., King, J.D., Bobbie, R.J., 1979. Determination of the sedimentary microbial biomass by extractible lipid phosphate. *Oecologia* 40, 51–62.
- White, H.K., Reddy, C.M., Eglinton, T.I., 2008. Radiocarbon-based assessment of fossil fuel-derived contaminant associations in sediments. *Environ. Sci. Technol.* 42, 5428–5434.
- White, H.K., Reddy, C.M., Eglinton, T.I., 2005. Isotopic Constraints on the Fate of Petroleum Residues Sequestered in Salt Marsh Sediments. *Environ. Sci. Technol.* 39, 2545–2551. <https://doi.org/10.1021/es048675f>
- Winterfeld, M., Mollenhauer, G., Dummann, W., Köhler, P., Lembke-Jene, L., Meyer, V.D., Hefter, J., McIntyre, C., Wacker, L., Kokfelt, U., Tiedemann, R., 2018. Deglacial mobilization of pre-aged terrestrial carbon from degrading permafrost. *Nat. Commun.* 9. <https://doi.org/10.1038/s41467-018-06080-w>
- Wörmer, L., Lipp, J.S., Hinrichs, K.-U., 2015. Comprehensive Analysis of Microbial Lipids in Environmental Samples Through HPLC-MS Protocols, in: McGenity, T.J., Timmis, K.N., Nogales, B. (Eds.), *Hydrocarbon and Lipid Microbiology Protocols*. Springer Berlin Heidelberg, Berlin, Heidelberg, pp. 289–317. [https://doi.org/10.1007/8623\\_2015\\_183](https://doi.org/10.1007/8623_2015_183)
- Wörmer, L., Lipp, J.S., Schröder, J.M., Hinrichs, K.-U., 2013. Application of two new LC-ESI-MS methods for improved detection of intact polar lipids (IPLs) in environmental samples. *Org. Geochem.* 59, 10–21.
- Ziaja, W., 2001. Glacial Recession in Sorkapland and Central Nordenskiöldöland, Spitsbergen, Svalbard, during the 20th Century. *Arct. Antarct. Alp. Res.* 33, 36–41. <https://doi.org/10.1080/15230430.2001.12003402>

## Appendix

Sediment depth	F <sup>14</sup> C	+-(abs)	Age B.P. (y)	+-(y)	TOC marine
1.5 cm	0.1157	0.0007	17327	48	12%
4.5 cm	0.0971	0.0007	18730	59	10%
13 cm	0.0801	0.0006	20280	57	8%
16.5 cm	0.0611	0.0006	22453	73	6%
22 cm	0.0555	0.0005	23219	77	6%
28 cm	0.0509	0.0005	23920	81	5%
43.5 cm	0.0367	0.0004	26547	97	4%
60 cm	0.0331	0.0004	27377	104	3%
83.5 cm	0.0495	0.0004	24142	68	5%
96 cm	0.0430	0.0005	25268	87	4%
103 cm	0.0380	0.0005	26270	96	4%
113 cm	0.0413	0.0005	25601	90	4%
133 cm	0.0389	0.0005	26083	95	4%

App. Table 2: Bulk OM radiocarbon data and corresponding age B.P.

ng/g	ββ31	31αβS	31αβR	31βαS+R
1.5 cm	0.166	7.309	4.983	0.000
4.5 cm	0.332	6.811	5.150	1.827
8 cm	0.492	8.361	5.902	0.000
13 cm	0.333	8.167	6.000	0.000
16.5 cm	0.040	4.682	3.512	0.000
19 cm	0.332	8.638	6.146	0.000
22 cm	0.660	18.317	12.871	4.290
25 cm	0.484	9.355	6.613	0.000
28 cm	0.166	7.475	5.482	0.000
31 cm	0.329	8.882	6.414	0.000
34 cm	0.497	10.099	7.119	3.146
43.5 cm	0.495	2.970	1.980	0.000
53.5 cm	0.489	5.212	3.583	0.000
60 cm	0.485	7.120	5.178	0.000
73.5 cm	0.333	4.167	3.000	0.000
83.5 cm	0.326	3.420	2.280	0.000
96 cm	0.669	5.518	3.846	0.000
103 cm	0.498	10.299	7.475	0.000
113 cm	0.498	6.146	4.485	0.000
123 cm	0.489	4.235	2.769	0.163
133 cm	0.162	3.883	2.913	0.000
137.5 cm	0.495	6.601	4.785	0.000

App. Table 1: Homohopane data

[ng/g]	FAME 14:0	FAME 15:0	FAME 16:1	FAME 16:0	FAME 17:0	FAME 18:2	FAME 18:1w9	FAME 18:1w11	FAME 18:0	FAME 19:0	FAME 20:0	FAME 21:0	FAME 22:6	FAME 22:0	FAME 23:0	FAME 24:0	FAME 25:0	FAME 26:0	FAME 27:0	FAME 28:0	FAME 29:0	FAME 30:0	
AO 2	+2.4	+0.7	+1.3	+10.2	+16.5	+0.5	+0.5	+1.2	+0.9	+0.2	+0.8	+0.3	+0.1	+0.3	+0.1	+0.9	+0.2	+0.7	+0.1	+1.6	+0.4	+0.1	+0.3
AO 3	+2.0	+0.6	+0.5	+1.2	+9.0	+1.2	+4.5	+3.4	+7.4	+0.9	+4.6	+0.9	+0.1	+5.3	+1.6	+1.2	+2.1	+1.2	+1.6	+7.0	+0.8	+2.5	+0.3
AO 4	+3.0	+0.9	+0.8	+1.7	+13	+2.2	+0.6	+0.8	+1.1	+0.2	+1.5	+1.0	+0.1	+0.3	+0.1	+1.1	+0.2	+0.8	+0.1	+1.8	+0.1	+0.1	+0.4
1.5 cm	+1098	+238	+597	+2967	+3759	+125	+372	+2722	+772	+465	+156	+347	+1395	+126	+41	+531	+115	+115	+48	+152	+36	+85	+42
4.5 cm	+663	+150	+167	+132	+1423	+2039	+79	+225	+1886	+426	+303	+87	+349	+77	+88	+112.8	+3.0	+5.0	-	+2.5	-	+4.8	-
8 cm	+428	+125	+131	+97	+1358	+1596	+13	+147	+1128	+445	+327	+117	+237	+124	+55	+148	-	+77	+43	+4.5	-	-	-
13 cm	+577	+139	+155	+215	+2109	+2226	+85	+190	+1326	+607	+351	+126	+238	+664	+122	+40	+416	+119	+48	+36	+7.5	+4.2	+4.2
16.5 cm	+1106	+26	+31	+34	+347	+335	+14	+200	+82	+207	+43	+3.0	+350	+7.3	+4.1	+12	-	+44.4	-	+2.2	-	+5.4	-
19 cm	+414	+172	+261	+248	+2325	+3153	+155	+328	+2337	+735	+229	+185	+691	+288	+76	+332	+168	+110	+168	+87	+191	+25	-
22 cm	+176	+33	+51	+39	+383	+474	+25	+345	+490	+40	+37	+107	+116	+344	+15	+344	+15	+10	+5.3	+4.2	-	+2.5	-
25 cm	+319	+107	+117	+102	+1198	+1412	+57	+116	+1005	+383	+261	+90	+200	+330	+125	+250	+113	+80	+42	+2.6	-	-	-
28 cm	+59	+20	+23	+16	+197	+212	+49.1	+122	+32	+16	+40	+51	+7.0	+7.0	+5.4	+13	-	+4.7	-	+2.6	-	-	-
31 cm	+521	+154	+181	+161	+1389	+2081	+72	+197	+398	+118	+189	+436	+144	+323	+126	+163	-	+81	+38	+4.5	-	+4.3	-
34 cm	+96	+29	+36	+25	+229	+313	+12	+207	+48	+21	+38	+68	+8.1	+271	+7.7	+13	-	+4.8	+2.3	+6.0	+98	+13	-
43.5 cm	+189	+98	+157	+84	+1295	+1749	+186	+1131	+518	+468	+147	+128	+383	+201	+182	+51	+236	+122	+60	+3.6	+1.3	+1.3	-
53.5 cm	+35	+18	+31	+13	+213	+263	-	+196	+57	+26	+26	+60	+11	+219	+11	+4.4	+20	+7.2	+3.6	+1.3	+1.3	+1.3	-
60 cm	+263	+112	+114	+66	+114	+1297	+47	+106	+293	+80	+202	+283	+116	+189	+101	+53	+132	+62	+3.7	+3.7	+3.7	+3.7	-
73.5 cm	+48	+21	+23	+10	+183	+195	+7.5	+112	+36	+14	+41	+44	+6.5	+159	+6.2	+4.5	+11	+3.7	+3.7	+3.7	+3.7	+3.7	-
83.5 cm	+277	+115	+120	+84	+988	+1137	+45	+106	+690	+68	+170	+261	+106	+194	+49	+135	+66	+66	+32	+2.0	+2.0	+2.0	-
96 cm	+263	+117	+121	+100	+994	+1281	+43	+114	+289	+293	+167	+145	+240	+92	+49	+114	+43	+43	+3.9	+3.9	+3.9	+3.9	-
103 cm	+367	+166	+162	+103	+1548	+2127	+74	+141	+604	+413	+203	+446	+194	+63	+195	+67	+255	+47	+125	+59	+5.3	+5.3	-
113 cm	+527	+280	+235	+129	+1934	+2360	+90	+205	+605	+493	+173	+248	+456	+217	+83	+285	+229	+142	+69	+3.6	+3.6	+3.6	-
123 cm	+597	+53	+46	+20	+318	+355	+14	+215	+77	+207	+60	+30	+50	+112	+8.8	+243	+14	+8.4	+4.2	+4.2	+4.2	+4.2	-
133 cm	+330	+165	+144	+76	+1127	+1435	+57	+138	+399	+342	+103	+180	+213	+157	+64	+164	+160	+90	+5.3	+5.3	+5.3	+5.3	-
137.5 cm	+60	+31	+28	+12	+186	+216	+9.1	+146	+42	+18	+36	+33	+8.9	+4.8	+5.6	+17	-	+5.3	+3.2	+3.2	+3.2	+3.2	-
	+450	+182	+164	+84	+1356	+1519	+67	+117	+408	+280	+113	+181	+435	+126	+61	+261	+134	+93	+28	+27	+1.7	+1.7	-
	+289	+145	+186	+96	+1541	+2634	+228	+2132	+665	+507	+198	+101	+355	+201	+242	+188	+39	+252	+56	+3.4	+3.4	+3.4	-
	+53	+27	+37	+15	+365	+396	-	+240	+131	+227	+61	+35	+20	+55	+11	-	+203	+12	+2.1	+3.4	+3.4	+3.4	-
	+138	+69	+65	+41	+690	+936	+37	+69	+196	+66	+117	+132	+93	+85	+91	+42	+120	+57	+28	+2.7	+1.7	+1.7	-
	+25	+13	+13	+6.4	+113	+140	+5.9	+72	+32	+11	+24	+5.3	+3.4	+72	+5.6	+3.6	+10	+3.4	+1.7	+1.7	+1.7	+1.7	-
	+184	+102	+92	+63	+979	+1464	+57	+113	+522	+315	+87	+179	+266	+114	+60	+142	+67	+67	+4.0	+4.0	+4.0	+4.0	-
	+34	+19	+19	+10	+161	+220	+11.9	+118	+178	+38	+15	+36	+41	+6.5	+5.1	+12	-	+4.0	+4.0	+4.0	+4.0	+4.0	-
	+318	+130	+127	+106	+1022	+1806	+90	+134	+537	+454	+99	+178	+300	+146	+181	+457	+181	+90	+205	+2.5	+2.5	+2.5	-
	+525	+254	+221	+126	+1780	+2191	+89	+192	+563	+467	+130	+220	+445	+175	+228	+223	+99	+99	+5.3	+5.3	+5.3	+5.3	-
	+496	+48	+44	+20	+293	+330	+14	+202	+67	+23	+44	+69	+9.8	+208	+14	-	+19	+5.8	+5.8	+5.8	+5.8	+5.8	-
	+467	+207	+230	+72	+1698	+2015	+72	+149	+439	+137	+133	+305	+160	+166	+173	+197	+98	+98	+94	+94	+94	+94	-
	+86	+39	+45	+11	+280	+303	+12	+157	+53	+24	+27	+47	+9.0	+140	+11	-	+17	+5.8	+3.6	+3.6	+3.6	+3.6	-

App. Table 3: Fatty acid methyl ester data. Uncertainties were determined due the standard deviation of the "Am Ochsenturm" (AO2-4) in house standards.

# Release and Remineralization of Ancient Carbon from Svalbard Glaciers

[ng/g]	n- C16	n- C17	n- C18	n- C19	n- C20	n- C21	n- C22	n- C23	n- C24	n- C25	n- C26	n- C27	n- C28	n- C29	n- C30	n- C31	n- C32	n- C33	n- C34	n- C35	n- C36	n- C37	n- C38	
AO 2	3.5	4.1	3.2	4.1	7.3	7.6	13	18	33	19	62	20	104	25	133	20	120	12	55	7.9	12	5.4	3.5	3.5
AO 3	±1.3	±0.3	±0.4	±0.3	±0.3	±0.7	±1.2	±2.8	±0.8	±3.6	±1.8	±6.1	±1.6	±8.0	±1.3	±7.8	±0.6	±4.1	±0.9	±0.4	±0.4	±1.3	±1.4	±1.4
AO 3	1.6	3.5	2.9	5.8	7.7	8.1	15	20	40	69	23	116	28	151	23	138	14	66	10	14	6.5	4.5	4.5	4.5
AO 3	±0.6	±0.2	±0.4	±0.3	±0.4	±0.8	±1.3	±3.4	±0.9	±4.0	±2.1	±6.9	±1.8	±9.1	±1.5	±8.9	±0.7	±4.9	±1.2	±1.1	±0.5	±1.7	±1.8	±1.8
AO 4	1.6	3.6	2.3	5.6	6.9	7.2	13	17	35	18	61	19	102	25	134	20	121	13	58	10	13	5.9	8.2	8.9
AO 4	±0.6	±0.2	±0.3	±0.3	±0.3	±0.7	±1.1	±2.9	±0.8	±3.5	±1.7	±6.0	±1.6	±8.1	±1.3	±7.9	±0.6	±4.4	±1.1	±1.1	±0.4	±3.1	±3.7	±3.7
1.5 cm	468	566	328	577	121	586	488	432	414	349	342	263	258	193	203	120	111	61	54	37	31	17.3	16.9	11.6
1.5 cm	±181	±37	±43	±30	±6.3	±28	±29	±35	±15	±20	±24	±15	±12	±12	±7.9	±7.2	±3.0	±4.0	±4.1	±2.5	±1.3	±6.4	±4.8	±4.8
4.5 cm	283	411	225	451	88	458	416	389	337	277	269	207	200	150	155	92	80	45	39	28	24	13.6	11.3	11.3
4.5 cm	±109	±27	±29	±23	±4.6	±22	±22	±28	±12	±16	±19	±12	±10	±9.3	±6.2	±2.0	±2.2	±2.9	±3.2	±2.0	±1.0	±4.2	-	-
8 cm	284	438	260	482	96	494	405	397	345	329	253	248	182	188	114	97	59	51	35	29	22.0	16.4	16.4	16.4
8 cm	±110	±28	±33	±25	±5.0	±24	±27	±34	±15	±19	±23	±15	±12	±11	±7.5	±6.3	±3.0	±3.9	±4.0	±2.4	±1.7	±6.2	-	-
13 cm	328	490	264	542	104	558	492	435	428	362	349	272	264	192	122	105	60	54	38	33	19.3	16.0	16.0	16.0
13 cm	±127	±32	±34	±28	±5.4	±27	±29	±36	±16	±20	±25	±16	±12	±12	±8.0	±6.8	±3.0	±4.1	±4.3	±2.6	±1.5	±6.0	-	-
16.5 cm	22	134	60	265	42	347	360	378	341	330	287	203	199	144	152	86	82	48	40	30	21	-	-	-
16.5 cm	±8.7	±8.9	±7.7	±13	±2.2	±17	±17	±23	±28	±13	±16	±12	±9.2	±9.1	±5.7	±5.3	±2.4	±3.0	±3.4	±1.7	-	-	-	-
19 cm	250	413	216	480	92	502	471	457	409	404	345	335	253	186	184	116	98	57	48	35	31	18.9	15.0	15.0
19 cm	±97	±27	±28	±25	±4.8	±24	±22	±14	±27	±34	±15	±19	±12	±11	±7.7	±6.4	±2.8	±3.6	±3.9	±2.5	±1.4	±5.6	-	-
22 cm	783	970	548	982	189	1004	911	891	801	780	682	651	505	480	366	353	225	187	111	94	68	62	41.3	25.4
22 cm	±303	±64	±71	±51	±10	±48	±41	±48	±53	±66	±30	±38	±46	±28	±23	±21	±15	±12	±5.5	±7.1	±7.7	±5.0	±3.1	±9.5
25 cm	385	524	262	557	101	585	518	454	443	378	359	280	267	194	202	126	108	62	53	38	35	22.3	16.1	16.1
25 cm	±149	±34	±34	±29	±5.3	±28	±25	±30	±38	±17	±21	±45	±16	±12	±12	±8.3	±7.0	±3.1	±3.9	±4.3	±2.8	±1.7	±6.1	±6.1
28 cm	75	271	135	434	76	514	508	509	464	441	387	371	283	272	200	201	126	109	61	53	38	31	-	-
28 cm	±29	±18	±17	±23	±4.0	±25	±23	±37	±37	±17	±21	±26	±16	±13	±12	±8.3	±7.1	±3.1	±4.0	±4.3	±2.5	-	-	-
31 cm	343	524	268	563	106	627	548	555	492	476	410	388	308	282	206	211	135	113	58	48	35	33	19.4	14.1
31 cm	±133	±35	±35	±29	±5.5	±29	±30	±40	±18	±22	±28	±17	±13	±13	±8.9	±7.3	±2.9	±3.6	±4.0	±2.6	±1.5	±5.3	-	-
34 cm	249	422	190	485	89	513	465	397	387	332	319	246	235	174	168	110	92	54	46	33	29	17.9	13.9	13.9
34 cm	±97	±28	±25	±25	±4.7	±25	±24	±26	±33	±15	±18	±22	±14	±11	±10	±7.3	±6.0	±2.7	±3.4	±3.7	±2.4	±1.3	±5.2	±5.2
43.5 cm	230	373	127	427	65	456	423	405	365	346	295	281	219	203	154	144	95	82	46	40	27	24	16.8	16.8
43.5 cm	±89	±25	±16	±22	±3.4	±22	±19	±22	±24	±29	±13	±16	±20	±12	±9.8	±6.3	±5.3	±3.0	±3.1	±1.9	±1.3	-	-	-
53.5 cm	357	508	219	555	97	582	522	503	436	418	362	339	268	252	187	188	118	101	58	49	36	30	15.3	15.3
53.5 cm	±138	±33	±28	±29	±5.1	±28	±24	±27	±29	±35	±16	±20	±24	±15	±12	±7.8	±6.5	±2.9	±3.7	±4.0	±2.4	±1.2	-	-
60 cm	597	789	364	835	156	840	748	703	621	588	514	485	373	352	268	247	165	131	80	70	49	42	28.8	21.0
60 cm	±231	±52	±47	±44	±8.2	±40	±34	±38	±41	±50	±23	±28	±34	±21	±17	±15	±11	±8.5	±4.0	±5.2	±5.5	±3.4	±2.2	±7.9
73.5 cm	387	554	214	589	96	603	549	520	455	434	373	346	275	250	191	181	120	98	63	51	35	31	19.7	15.7
73.5 cm	±150	±37	±29	±28	±5.0	±29	±25	±28	±30	±37	±16	±20	±25	±15	±12	±10	±7.9	±6.4	±3.1	±3.9	±2.5	±1.5	±5.9	±5.9
83.5 cm	347	474	206	501	88	505	441	419	371	351	299	284	221	206	154	151	97	81	50	40	29	23	15.6	12.4
83.5 cm	±134	±31	±27	±26	±4.6	±24	±20	±23	±25	±30	±13	±16	±20	±12	±9.7	±9.1	±6.4	±5.3	±3.0	±3.3	±1.9	±1.2	±4.7	±4.7
96 cm	120	395	153	604	100	701	668	647	574	536	464	442	345	311	226	223	135	119	66	61	37	31	-	-
96 cm	±46	±26	±20	±31	±5.3	±34	±31	±35	±38	±45	±20	±26	±31	±18	±14	±13	±8.9	±7.7	±3.3	±4.6	±4.2	±2.5	-	-
103 cm	390	540	299	581	113	598	535	522	468	445	395	379	292	275	210	200	129	104	62	52	39	34	23.3	17.6
103 cm	±151	±36	±39	±30	±5.9	±29	±25	±28	±31	±38	±17	±22	±27	±16	±13	±12	±8.5	±6.7	±3.1	±3.9	±4.4	±2.8	±1.8	±6.6
113 cm	309	444	222	479	84	494	446	433	385	359	314	295	232	215	163	157	103	83	50	44	32	27	17.3	15.0
113 cm	±120	±29	±29	±25	±4.4	±24	±20	±23	±26	±30	±14	±17	±21	±13	±10	±9.4	±6.8	±5.4	±2.5	±3.3	±3.6	±2.2	±1.3	±5.6
123 cm	237	421	194	502	87	545	491	496	440	408	359	333	266	249	188	179	116	97	61	48	35	32	18.2	16.3
123 cm	±92	±42	±28	±25	±4.6	±26	±23	±27	±29	±35	±16	±19	±24	±15	±12	±11	±7.6	±6.3	±3.0	±3.6	±2.6	±1.4	±6.1	±6.1
133 cm	169	357	175	472	87	519	482	446	389	374	318	297	233	217	164	157	103	84	50	42	31	27	16.2	14.2
133 cm	±66	±24	±23	±25	±4.6	±25	±22	±24	±26	±32	±14	±17	±21	±13	±10	±9.4	±6.8	±5.4	±2.5	±3.1	±3.5	±2.1	±1.2	±5.4
137.5 cm	336	476	249	534	105	551	482	444	397	372	324	318	242	228	170	168	108	90	52	48	32	28	17.8	13.5
137.5 cm	±131	±32	±32	±28	±5.5	±27	±22	±24	±26	±32	±14	±18	±22	±13	±11	±10	±7.1	±5.9	±2.6	±3.6	±3.6	±2.2	±1.3	±5.1

App. Table 4: n-Alkane data. Uncertainties were determined due the standard deviation of the "Am Ochsentrum" (AO2-4) in house standards.

# Release and Remineralization of Ancient Carbon from Svalbard Glaciers

[ng/l]	GDGT 0	GDGT 1	GDGT 2	GDGT 3	Cren.	Cren. Iso	brGDGT la	brGDGT lb	brGDGT lc	brGDGT lla (5)	brGDGT lla (6)	brGDGT llb (5)	brGDGT llb (6)	brGDGT llc (5)	brGDGT llc (6)	brGDGT lll (5)	brGDGT lll (6)	brGDGT llc (5)	brGDGT llc (6)	brGDGT lll (5)	brGDGT lll (6)	brGDGT lllc (5)	brGDGT lllc (6)
AO 2	2.43 ±0.143	0.25 ±0.012	0.14 ±0.010	0.06 ±0.003	1.64 ±0.13	±0.001	3.23 ±0.153	0.90 ±0.060	0.31 ±0.028	1.99 ±0.132	0.58 ±0.032	0.38 ±0.027	0.28 ±0.014	0.06 ±0.003	0.05 ±0.002	0.67 ±0.034	0.45 ±0.024	0.03 ±0.002	0.04 ±0.003	0.03 ±0.002	0.04 ±0.003	0.01 ±0.001	0.01 ±0.001
AO 3	2.85 ±0.168	0.28 ±0.014	0.17 ±0.011	0.07 ±0.003	2.02 ±0.136	±0.001	3.68 ±0.174	1.06 ±0.070	0.39 ±0.028	2.39 ±0.159	0.65 ±0.036	0.46 ±0.032	0.32 ±0.016	0.07 ±0.003	0.05 ±0.002	0.78 ±0.039	0.49 ±0.026	0.03 ±0.002	0.05 ±0.003	0.03 ±0.002	0.05 ±0.003	0.01 ±0.001	0.01 ±0.001
AO 4	2.59 ±0.152	0.26 ±0.013	0.15 ±0.010	0.06 ±0.003	1.73 ±0.168	±0.001	3.46 ±0.164	0.92 ±0.061	0.34 ±0.030	2.15 ±0.143	0.60 ±0.033	0.41 ±0.029	0.31 ±0.015	0.06 ±0.003	0.05 ±0.002	0.73 ±0.039	0.47 ±0.025	0.03 ±0.002	0.05 ±0.003	0.03 ±0.002	0.05 ±0.003	0.01 ±0.001	0.01 ±0.001
15 cm	8.47 ±0.500	0.24 ±0.012	0.08 ±0.005	0.05 ±0.003	6.58 ±0.144	±0.001	0.08 ±0.004	0.08 ±0.005	0.04 ±0.004	0.04 ±0.002	0.03 ±0.001	0.10 ±0.007	0.04 ±0.002	0.01 ±0.001	0.01 ±0.001	0.12 ±0.006	0.06 ±0.003	0.02 ±0.001	0.01 ±0.001	0.02 ±0.001	0.01 ±0.001	0.01 ±0.001	0.00 ±0.001
45 cm	6.61 ±0.390	0.17 ±0.008	0.06 ±0.004	0.04 ±0.002	5.14 ±0.545	±0.001	0.05 ±0.003	0.06 ±0.004	0.03 ±0.003	0.03 ±0.002	0.02 ±0.001	0.09 ±0.006	0.02 ±0.001	0.01 ±0.001	0.01 ±0.001	0.08 ±0.004	0.05 ±0.001	0.01 ±0.001	0.01 ±0.001	0.01 ±0.001	0.01 ±0.001	0.01 ±0.001	0.00 ±0.001
8 cm	7.30 ±0.430	0.16 ±0.008	0.07 ±0.005	0.05 ±0.002	5.36 ±0.427	±0.003	0.06 ±0.003	0.06 ±0.004	0.03 ±0.003	0.04 ±0.002	0.02 ±0.001	0.10 ±0.007	0.02 ±0.001	0.01 ±0.001	0.01 ±0.001	0.10 ±0.005	0.05 ±0.003	0.02 ±0.001	0.01 ±0.001	0.02 ±0.001	0.01 ±0.001	0.01 ±0.001	0.00 ±0.001
13 cm	7.67 ±0.452	0.17 ±0.009	0.07 ±0.004	0.05 ±0.002	5.86 ±0.444	±0.001	0.06 ±0.003	0.05 ±0.004	0.03 ±0.003	0.04 ±0.003	0.03 ±0.002	0.08 ±0.006	0.03 ±0.001	0.01 ±0.001	0.01 ±0.001	0.13 ±0.006	0.06 ±0.003	0.02 ±0.001	0.01 ±0.001	0.02 ±0.001	0.01 ±0.001	0.01 ±0.001	0.00 ±0.001
16.5 cm	5.43 ±0.320	0.12 ±0.006	0.05 ±0.004	0.04 ±0.002	3.87 ±0.486	±0.001	0.05 ±0.003	0.03 ±0.002	0.02 ±0.001	0.03 ±0.002	0.02 ±0.001	0.05 ±0.003	0.02 ±0.001	0.01 ±0.001	0.01 ±0.001	0.11 ±0.006	0.06 ±0.003	0.02 ±0.001	0.01 ±0.001	0.02 ±0.001	0.01 ±0.001	0.00 ±0.001	0.00 ±0.001
19 cm	8.19 ±0.483	0.18 ±0.009	0.08 ±0.005	0.05 ±0.003	6.12 ±0.321	±0.001	0.05 ±0.002	0.03 ±0.002	0.02 ±0.002	0.04 ±0.002	0.02 ±0.001	0.05 ±0.004	0.02 ±0.001	0.01 ±0.001	0.00 ±0.001	0.14 ±0.007	0.06 ±0.001	0.01 ±0.001	0.00 ±0.001	0.01 ±0.001	0.00 ±0.001	0.00 ±0.001	0.00 ±0.001
22 cm	8.20 ±0.454	0.19 ±0.009	0.09 ±0.005	0.07 ±0.003	6.71 ±0.557	±0.001	0.07 ±0.004	0.05 ±0.003	0.02 ±0.002	0.05 ±0.004	0.04 ±0.002	0.09 ±0.005	0.02 ±0.001	0.01 ±0.001	0.00 ±0.001	0.17 ±0.008	0.06 ±0.003	0.02 ±0.001	0.01 ±0.001	0.02 ±0.001	0.01 ±0.001	0.01 ±0.001	0.00 ±0.001
25 cm	7.70 ±0.454	0.18 ±0.009	0.08 ±0.005	0.06 ±0.003	5.50 ±0.557	±0.001	0.09 ±0.004	0.05 ±0.003	0.02 ±0.002	0.06 ±0.004	0.03 ±0.002	0.08 ±0.005	0.02 ±0.001	0.01 ±0.001	0.01 ±0.001	0.13 ±0.007	0.07 ±0.004	0.02 ±0.001	0.01 ±0.001	0.02 ±0.001	0.01 ±0.001	0.01 ±0.001	0.00 ±0.001
28 cm	5.56 ±0.328	0.14 ±0.007	0.06 ±0.004	0.04 ±0.002	4.30 ±0.357	±0.001	0.06 ±0.003	0.04 ±0.002	0.02 ±0.002	0.04 ±0.003	0.03 ±0.002	0.06 ±0.004	0.02 ±0.001	0.01 ±0.001	0.01 ±0.001	0.12 ±0.006	0.06 ±0.003	0.02 ±0.001	0.01 ±0.001	0.02 ±0.001	0.01 ±0.001	0.01 ±0.001	0.00 ±0.001
31 cm	8.69 ±0.513	0.19 ±0.010	0.08 ±0.006	0.07 ±0.003	6.61 ±0.548	±0.002	0.08 ±0.004	0.05 ±0.003	0.03 ±0.002	0.06 ±0.004	0.03 ±0.002	0.08 ±0.005	0.03 ±0.002	0.01 ±0.001	0.01 ±0.001	0.20 ±0.010	0.08 ±0.003	0.02 ±0.001	0.01 ±0.001	0.02 ±0.001	0.01 ±0.001	0.01 ±0.001	0.00 ±0.001
34 cm	6.97 ±0.411	0.16 ±0.008	0.07 ±0.005	0.05 ±0.003	4.79 ±0.397	±0.001	0.07 ±0.003	0.04 ±0.002	0.02 ±0.002	0.05 ±0.003	0.03 ±0.002	0.05 ±0.004	0.02 ±0.001	0.01 ±0.001	0.01 ±0.001	0.12 ±0.006	0.07 ±0.004	0.02 ±0.001	0.01 ±0.001	0.02 ±0.001	0.01 ±0.001	0.01 ±0.001	0.00 ±0.001
43.5 cm	4.95 ±0.292	0.11 ±0.006	0.05 ±0.003	0.04 ±0.002	3.64 ±0.302	±0.001	0.05 ±0.003	0.03 ±0.002	0.01 ±0.001	0.05 ±0.003	0.03 ±0.002	0.04 ±0.003	0.02 ±0.001	0.01 ±0.001	0.01 ±0.001	0.11 ±0.008	0.06 ±0.004	0.02 ±0.001	0.01 ±0.001	0.02 ±0.001	0.01 ±0.001	0.01 ±0.001	0.00 ±0.001
53.5 cm	5.70 ±0.336	0.15 ±0.008	0.06 ±0.004	0.05 ±0.002	4.75 ±0.394	±0.001	0.11 ±0.005	0.07 ±0.004	0.03 ±0.003	0.07 ±0.004	0.04 ±0.002	0.09 ±0.006	0.03 ±0.002	0.01 ±0.001	0.01 ±0.001	0.15 ±0.014	0.10 ±0.005	0.02 ±0.001	0.01 ±0.001	0.02 ±0.001	0.01 ±0.001	0.01 ±0.001	0.00 ±0.001
60 cm	5.30 ±0.312	0.17 ±0.009	0.08 ±0.005	0.04 ±0.002	4.36 ±0.361	±0.001	0.18 ±0.008	0.09 ±0.006	0.05 ±0.004	0.13 ±0.008	0.08 ±0.004	0.14 ±0.009	0.05 ±0.002	0.02 ±0.001	0.02 ±0.001	0.29 ±0.008	0.16 ±0.009	0.03 ±0.001	0.02 ±0.001	0.03 ±0.001	0.01 ±0.001	0.01 ±0.001	0.01 ±0.001
73.5 cm	3.47 ±0.205	0.10 ±0.005	0.04 ±0.003	0.03 ±0.001	2.81 ±0.233	±0.001	0.12 ±0.005	0.06 ±0.004	0.03 ±0.003	0.08 ±0.003	0.05 ±0.003	0.09 ±0.006	0.03 ±0.001	0.01 ±0.001	0.01 ±0.001	0.17 ±0.007	0.10 ±0.005	0.02 ±0.001	0.01 ±0.001	0.02 ±0.001	0.01 ±0.001	0.01 ±0.001	0.00 ±0.001
83.5 cm	4.95 ±0.292	0.13 ±0.006	0.05 ±0.004	0.04 ±0.002	3.87 ±0.321	±0.002	0.11 ±0.005	0.06 ±0.004	0.04 ±0.003	0.06 ±0.004	0.04 ±0.002	0.10 ±0.007	0.03 ±0.001	0.01 ±0.001	0.01 ±0.001	0.14 ±0.008	0.10 ±0.005	0.02 ±0.001	0.01 ±0.001	0.02 ±0.001	0.01 ±0.001	0.01 ±0.001	0.00 ±0.001
96 cm	5.50 ±0.324	0.15 ±0.008	0.07 ±0.004	0.04 ±0.002	4.29 ±0.356	±0.002	0.16 ±0.008	0.09 ±0.006	0.05 ±0.004	0.11 ±0.008	0.07 ±0.004	0.12 ±0.009	0.05 ±0.003	0.02 ±0.001	0.01 ±0.001	0.02 ±0.006	0.16 ±0.008	0.02 ±0.002	0.02 ±0.001	0.02 ±0.001	0.01 ±0.001	0.01 ±0.001	0.01 ±0.001
103 cm	3.24 ±0.191	0.08 ±0.004	0.04 ±0.003	0.03 ±0.001	2.62 ±0.217	±0.001	0.07 ±0.004	0.05 ±0.003	0.02 ±0.002	0.05 ±0.003	0.03 ±0.002	0.07 ±0.005	0.02 ±0.001	0.01 ±0.001	0.01 ±0.001	0.12 ±0.007	0.07 ±0.004	0.01 ±0.002	0.01 ±0.001	0.01 ±0.002	0.01 ±0.001	0.01 ±0.001	0.00 ±0.001
113 cm	3.89 ±0.229	0.10 ±0.005	0.04 ±0.003	0.03 ±0.002	3.07 ±0.254	±0.001	0.09 ±0.004	0.05 ±0.004	0.03 ±0.002	0.06 ±0.004	0.04 ±0.002	0.08 ±0.005	0.03 ±0.001	0.01 ±0.001	0.01 ±0.001	0.13 ±0.015	0.08 ±0.004	0.01 ±0.001	0.01 ±0.001	0.01 ±0.001	0.01 ±0.001	0.01 ±0.001	0.00 ±0.001
123 cm	8.09 ±0.477	0.23 ±0.012	0.10 ±0.006	0.07 ±0.004	6.97 ±0.578	±0.004	0.27 ±0.013	0.14 ±0.009	0.07 ±0.007	0.15 ±0.005	0.10 ±0.005	0.21 ±0.014	0.06 ±0.003	0.03 ±0.001	0.02 ±0.001	0.31 ±0.011	0.21 ±0.015	0.03 ±0.002	0.03 ±0.001	0.02 ±0.002	0.03 ±0.001	0.01 ±0.001	0.01 ±0.001
133 cm	5.30 ±0.312	0.14 ±0.007	0.06 ±0.004	0.04 ±0.002	4.26 ±0.353	±0.003	0.16 ±0.008	0.10 ±0.006	0.05 ±0.004	0.10 ±0.007	0.06 ±0.004	0.13 ±0.009	0.04 ±0.002	0.01 ±0.001	0.01 ±0.001	0.22 ±0.011	0.15 ±0.008	0.02 ±0.001	0.02 ±0.001	0.02 ±0.001	0.01 ±0.001	0.01 ±0.001	0.01 ±0.001
137.5 cm	9.55 ±0.563	0.24 ±0.012	0.11 ±0.008	0.08 ±0.004	7.42 ±0.616	±0.001	0.17 ±0.008	0.11 ±0.007	0.06 ±0.005	0.10 ±0.007	0.07 ±0.004	0.17 ±0.012	0.06 ±0.003	0.02 ±0.001	0.02 ±0.001	0.25 ±0.014	0.16 ±0.009	0.03 ±0.002	0.02 ±0.001	0.03 ±0.002	0.02 ±0.001	0.01 ±0.001	0.01 ±0.001

App. Table 5: GDGT data. Uncertainties were determined due the standard deviation of the “Am Ochsenturm” (AO2-4) in house standards.

GL 0-3cm			PL 0-3cm		
	Area	relative abundances:		Area	relative abundances:
SQDG	7838787	29%	PG	19823739.8	7%
2G-DAG	9530263	35%	PME	68880041.9	24%
DPG	6328995	23%	PE	70170858.8	25%
lyso-DPG	2444454	9%	PC	76836685.6	27%
1G-DAG	1144933	4%	DPG	10117872.9	4%
Total:	27287432		lyso-DPG	5343044.9	2%
			BL - DGTS & DGTA	31496457.6	11%
			Total:	282668701.5	
GL 8cm			PL 8cm		
	Area	relative abundances:		Area	relative abundances:
SQDG	1339411	30%	PG	9434956	11%
2G-DAG	715101	16%	PME	18498579	21%
DPG	1694757	39%	PE	19065765	21%
lyso-DPG	499282	11%	PC	27336656	31%
1G-DAG	152804	3%	DPG	3690887	4%
Total:	4401355		lyso-DPG	1322572	1%
			BL - DGTS & DGTA	10024237	11%
			Total:	89373652	
GL 13cm			PL 13cm		
	Area	relative abundances:		Area	relative abundances:
SQDG	2059252.21	64%	PG	9434956	11%
2G-DAG	883102.8	28%	PME	18498579	21%
DPG	96100.67	3%	PE	19065765	21%
lyso-DPG	39399.58	1%	PC	27336656	31%
1G-DAG	132450.22	4%	DPG	3690887	4%
Total:	3210305.48		lyso-DPG	1322572	1%
			BL - DGTS & DGTA	10024237	11%
			Total:	89373652	
GL 83.5cm			PL 83.5cm		
	Area	relative abundances:		Area	relative abundances:
SQDG	1986180.9	72%	PG	9083849.6	11%
2G-DAG	366826.7	13%	PME	15761650.1	19%
DPG	38148.8	1%	PE	18509183	22%
lyso-DPG		0%	PC	27657598.3	33%
1G-DAG	372424.8	13%	DPG	2134249.7	3%
Total:	2763581.2		lyso-DPG	1785821.8	2%
			BL - DGTS & DGTA	9647283.4	11%
			Total:	84579635.9	
GL 133-136cm			PL 133-136cm		
	Area	relative abundances:		Area	relative abundances:
SQDG	2641794	19%	PG	14108231	7%
2G-DAG	1815157	13%	PME	56571400	29%
DPG	4993236	36%	PE	49089960	25%
lyso-DPG	4572569	33%	PC	62951928	32%
1G-DAG		0%	DPG	1440744	1%
Total:	14022756		lyso-DPG	2305361	1%
			BL - DGTS & DGTA	11837340	6%
			Total:	198304964	

App. Table 6 Relative contributions of IPLs in glycol-and polar-lipid fraction



App. Figure 1. Line scans and X-ray images of core HH14-897-MF-GC provided by Forwick